

Characterizing transport and capture of finely divided dispersed phase on fibers and meshes: From filtration to fog harvesting

Doctor of Philosophy
(Engineering)

Thesis submitted by
Arkadeep Datta

Registration No: 1012014001 of 20-21
Index No.: 273/20/E

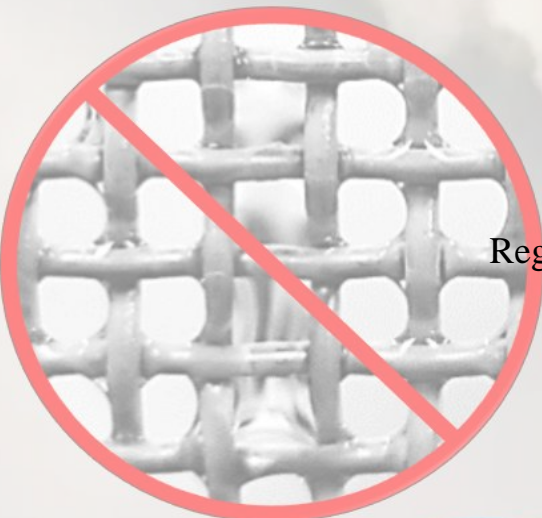
Under the supervision of

Prof. Ranjan Ganguly
(Jadavpur University, India)
&

Prof. Harunori Yoshikawa
(Doshisha University, Japan)

Department of Power Engineering
Faculty Council of Engineering and Technology
Jadavpur University
Kolkata, India

Year: 2024



Characterizing transport and capture of finely divided dispersed phase on fibers and meshes: From filtration to fog harvesting

**Doctor of Philosophy
(Engineering)**

**Thesis submitted by
Arkadeep Datta**

Registration No: **1012014001** of 20-21
Index No.: **273/20/E**

Under the supervision of

Prof. Ranjan Ganguly
(Jadavpur University, India)

&

Prof. Harunori Yoshikawa
(Doshisha University, Japan)

**Department of Power Engineering
Faculty Council of Engineering and Technology
Jadavpur University
Kolkata, India**

Year: 2024

**JADAVPUR UNIVERSITY
KOLKATA – 700032,
INDIA**

Index No.: **273/20/E**

Title of the thesis: Characterizing transport and capture of finely divided dispersed phase on fibers and meshes: From filtration to fog harvesting

Name, Designation and Institution of Supervisors

Supervisor:

Prof. Ranjan Ganguly
Professor
Department of Power Engineering
Faculty Council of Engineering and Technology
Jadavpur University
Kolkata, 700106, India

Co-Supervisor: Prof. Harunori Yoshikawa

Professor
Department of Electrical Engineering
Faculty of Science & Engineering
Doshisha University
Address: Faculty of Science & Engineering, Doshisha University
1-3 Tatara Miyakodani, Kyotanabe-shi 610-0321 Japan

List of Publications / Conferences / Technical Invention Disclosure

International Journal Publications

1. Mukhopadhyay, A., **Datta, A.**, Dutta, P. S., Datta, A., & Ganguly, R., Droplet morphology-based wettability tuning and design of fog harvesting mesh to minimize mesh-clogging. *Langmuir*, 2024, 40, 15, 8094–8107. DOI: 10.1021/acs.langmuir.4c00075
2. **Datta, A.**, Ganguly, R., & Yoshikawa, H. Tunable Dielectrophoretic (DEP) Filters for Air-Borne Microdroplet Capture. Available at SSRN 4693346. (*Under review*)

Conference publications

1. Saha, A., **Datta, A.**, Mukhopadhyay, A., Datta, A., Ganguly, R. “Time-dependent droplet detachment behaviour from wettability-engineered fibers during fog harvesting”, Proceedings of the 9th International and 49th National Conference on Fluid Mechanics and Fluid Power (FMFP), December 14-16, 2022, IIT Roorkee, Roorkee-247667, Uttarakhand, India
2. **Datta, A.**, Mukhopadhyay, A., Dutta, P.S., Saha, A, Datta, A., Ganguly, R. “Droplet detachment from a horizontal fiber of a fog harvesting mesh”, 48th National Conference on Fluid Mechanics and Fluid Power, Dec. 27-29, 2021, BITS Pilani, India. **Received Prof. BVSSS Prasad Memorial Best Paper Award.**
3. Yoshikawa, H., **Datta, A.**, Ganguly, R. “Microdroplet capture by a tunable dielectrophoretic (DEP) filter”, 75th Annual Meeting of the Division of Fluid Dynamics, Volume 67, Number 19, 2022
4. **Datta, A.**, Mukhopadhyay, A., Datta, A., Ganguly, R., “Designs of clog-free metal mesh for fog harvesting from cooling tower plume”, Proceedings of the International Conference on Innovations in the Power Sector towards Sustainable Development Goals-iPSSDG, iPSSDG 2023, 23rd - 24th June 2023, ISBN 978-93-5891-755-0.
5. **Datta, A.**, Mukhopadhyay, A., Datta, A., Ganguly, R., “ALIVE: A Low-Cost Interactive Vaccine Storage Environment Module ensuring easy portability and remote tracking of operational logistics to the last mile”, Intelligent Control, Robotics, and Industrial Automation - Proceedings of International Conference, RCAAI 2023, 12 —14 October, 2023, Manipal Institute of Technology, Manipal, India.

Patents/ Patent Applications

1. **Datta, A.**, Mukhopadhyay, A., Datta, A., Ganguly, R.,_“‘Never-clog’ mesh designs for capture and separation of a dispersed phase from a flowing fluid stream and systems thereof,” Indian Patent filed, Application Number 202231045629, Date of Filing: 10th August, 2022, Publication Date (U/S 11A): 17th March, 2023. Under Examination.
2. Mukhopadhyay, A., **Datta, A.**, Datta, A., Ganguly, R., “An IoT-based Portable, Integrated, Remotely Operable Environmental Chamber with real-time location tracking for multimodal, multi-system applications,” Indian Patent filed, Application Number 202231030204, Date of Filing: 26th May, 2022; Publication Date (U/S 11A): 24th June,

2022. First Examination Report received on 09/11/2022, Response submitted on 24/04/2023.

List of Funding / Awards / Fellowships

(a) List of Funding / Fellowships (3)

1. **JRF** under **TEQIP III** of Jadavpur University during July 2019 – Jan 2021.
2. **JRF** (Feb 2021 – Feb 2023) followed by **SRF** (Feb 2023 – July 2023) under **SERB – CRG** project (Grant No: CRG/2019/005887) titled “Optimizing wettability-engineered metal mesh for cooling tower fog harvesting”.
3. **CNRS**-(IEA00338) as a visiting researcher (Oct 2021 – Dec 2021) at Institut de Physique (INPHYNI) of University Cote d'Azur, France.

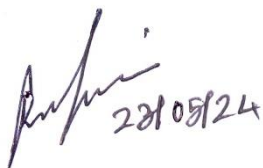
(b) List of Awards (2)

1. Received Prof. BVSSS Prasad Memorial Best Paper Award. 48th National Conference on Fluid Mechanics and Fluid Power, Dec. 27-29, 2021, BITS Pilani, India
2. Finalist at Falling Walls Lab India 2022 for the entry “Breaking the wall of frugal vaccine transportation and delivery logistics.”

CERTIFICATE FROM THE SUPERVISOR/S

This is to certify that the thesis entitled “**Characterizing transport and capture of finely divided dispersed phase on fibers and meshes: From filtration to fog harvesting**” submitted by **Mr. ARKADEEP DATTA**, who got his/her name registered on **09.12.2020** for the award of Ph. D. (Engg.) degree of Jadavpur University is absolutely based upon his own work under our supervision and that neither his thesis nor any part of the thesis has been submitted for any degree/diploma or any other academic award anywhere before.

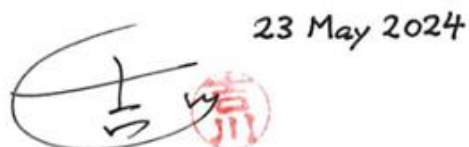
1. Prof. Ranjan Ganguly



Signature of the Supervisor
and date with Office Seal

Dr. Ranjan Ganguly
Professor
Dept. of Power Engineering
Jadavpur University, Salt Lake Campus
Kolkata-700 106

2. Prof. Harunori Yoshikawa



Signature of the Supervisor
and date with Office Seal

〒610-0321
京都府京田辺市多々羅都谷1-3
同志社大学理工学部電気工学科

“STATEMENT OF ORIGINALITY”

I, Arkadeep Datta, registered on 09/12/2020 do hereby declare that this thesis entitled **“Characterizing transport and capture of finely divided dispersed phase on fibers and meshes: From filtration to fog harvesting”** contains literature survey and original research work done by the undersigned candidate as part of Doctoral studies.

All information in this thesis have been obtained and presented in accordance with existing academic rules and ethical conduct. I declare that, as required by these rules and conduct, I have fully cited and referred all materials and results that are not original to this work.

I also declare that I have checked this thesis as per the “Policy on Anti Plagiarism, Jadavpur University, 2019”, and the level of similarity as checked by iThenticate software is 9.0 %.

Signature of Candidate:

Arkadeep Datta

Date :

27/05/2024

Certified by Supervisor(s):

(Signature with date, seal)

1.

Dr. Ranjan Ganguly
Professor
Dept. of Power Engineering
Jadavpur University, Salt Lake Campus
Kolkata-700 106

2.

23 May 2024

Signature of the Supervisor
and date with Office Seal

〒610-0321

京都府京田辺市多々羅都谷1-3

同志社大学理工学部電気工学科

ACKNOWLEDGEMENTS

I wish to extend my sincere gratitude to my esteemed supervisors, Prof. Ranjan Ganguly, and Prof. Amitava Datta of Jadavpur University (India), for their invaluable guidance, unwavering support, and insightful mentorship throughout the course of my dissertation work. Their expertise, encouragement, and constructive feedback have been instrumental in shaping my research journey and fostering my development as a researcher.

My academic journey has been enriched by diverse experiences. During my undergraduate years, I found joy in engaging with robotics competitions, relishing the process of constructing functional models capable of executing basic tasks, but my focus was never inclined towards research. I always strived to be an officer in the Air Force and later when it did not come to fruition, I redirected my focus to be an officer in the Indian Engineering Services, but a chance encounter with Prof. Ganguly and his acceptance of my request to pursue my master's in his lab, a dynamic space where researchers thrive. Here I was introduced to intricacies of surface science, and I gradually took a keen interest in research. I must mention, that Dr. Chayan Das, who was then pursuing his PhD in AMRA lab, had a great role in shaping my research journey. Each experience has contributed to my growth as a researcher and has shaped my interdisciplinary approach to addressing societal challenges.

I am grateful for the enriching opportunity to work as a research intern at Institut de Physique de Nice, France, under the guidance of Prof. Harunori Yoshikawa and Prof. Medici Marie-Gabrielle. This experience broadened my horizons, enhanced my technical skills, and instilled in me the confidence to pursue any forthcoming opportunities.


I am deeply thankful to Prof. Amitava Gupta and Prof. Kamal K. Mondal, Heads of the Power Engineering Department at Jadavpur University, for their generous support and assistance in providing access to essential resources that significantly contributed to the progress of my work.

I extend my heartfelt appreciation to my fellow labmates: Saikat Roy, with whom I engaged in countless discussions on both politics and research; Ankit Roy, with whom I quarreled a lot – for no good reason; and Saikat Halder, my junior and a wonderful friend. I would also like to thank my esteemed co-researchers at Jadavpur University, Dr. Mithun Das, Mr. Arijit Saha, and Mr. Rudrajit Majumder for their invaluable contributions, constant efforts, and collaborative spirit in facilitating experimental setups and offering invaluable insights throughout the research process.

Furthermore, I express my profound gratitude to my family, particularly, Mrs. Kalpana Datta and uncle Mr. Swapan Datta, for their unwavering support, encouragement, and belief in my abilities. I am also deeply grateful to my dear friend and co-researcher Mr. Arani Mukhopadhyay, for unwavering support during this demanding academic journey. The endless discussions that we had was really enriching in shaping our research.

I acknowledge with deep appreciation the assistance and guidance provided by numerous respected individuals whose expertise, suggestions, and support have been instrumental in the completion of this research work. Their encouragement, support, and guidance have been invaluable in helping me overcome obstacles and achieve my academic aspirations.

Going forward in my journey, I am inspired by the vision of bridging the gap between industry and academia to foster innovation and address pressing societal challenges. With a steadfast commitment to sustainability and a dedication to leveraging research for the greater good, I am determined to make meaningful contributions to the fields of energy transition, water conservation, and bio-medical engineering.



Askadeep Datta
27/05/2024

Dedicated to my father...
...I hope you bless me from afar

Dedicated to my family...

TABLE OF CONTENTS

	Page
Title page of the thesis	3
List of Publications / Conferences / Technical Invention Disclosure	4
List of Funding / Awards / Fellowships	6
Certificates from the supervisor/ s	7
Statement of originality	8
Acknowledgements	9
Abstract	26
Chapter 1: Introduction	
1 Motivation and prelude	30
1.1 Filtration of dispersed phases in air: particulate matter and fog droplets	33
1.1.1 Air filtration: Separation of suspended particulate matter in air	33
1.1.2 Fog harvesting: capture of airborne water droplets as alternate water source	35
1.1.2.1 Fog harvesting in Nature	36
1.1.2.2 Anthropogenic fog harvesting: <i>community and industry</i>	38
1.2 Issues in capture and separation of dispersed phase: particulate filtration and fog capture	41
1.2.1 Air-filtration	41
1.2.2 Fog capture	45
1.3 Gap area	49
1.4 Objectives	51
Chapter 2: Tunable dielectrophoretic (DEP) filters for air-borne micro-droplet capture	
2 A dielectrophoretic mesh filter for the capture of airborne liquid droplets	55
2.1 Theoretical modelling and simulation	58
2.2 General description of particle trajectories	62
2.3 Role of DEP in particle capture	64
2.4 Effects of varying electric field strength	67
2.5 Effect of varying operating frequency	68
2.6 Average collection efficiency	70
2.7 Merits of DEP filtration	78

Chapter 3: Droplet morphology-based wettability tuning and design of fog harvesting mesh to minimize mesh-clogging

3	Clog resistant meshes for efficient fog capture	81
3.1	Experimental	83
3.2	Simulation	85
3.3	Results and Discussions	
3.3.1	Barrel or clamshell shape?: Surface Evolver (SE) simulations	86
3.3.2	Estimation of maximal droplet dimensions from SE simulations	87
3.3.3	Experimental investigations into droplet morphology	88
3.3.4	Design and characterization of “clog-proof” meshes	90
3.3.4.1	Droplet maximal dimension	90
3.3.5	‘Clog-proof’ mesh selection criteria and efficiencies	95
3.3.6	Aerodynamics of flow through a mesh	95
3.3.7	Deposition and total efficiencies	100

Chapter 4: Concluding remarks

4.1	Summary of work	104
4.1.1	Dielectrophoretic separation of dispersed phase in air	104
4.1.2	Meshes for filtering dispersed phases, particularly designed for fog harvesting	105
4.2	Future scope of work	106

Appendix A

A1	Validation	109
A2	Stochasticity in particle trajectory	109
A3	Time-averaged spatial distribution of E2 field around the electrodes	110
A4	Role of DEP forces in particle capture	110
A5	Particle capture asymmetry attributed to 3-phase voltage waveform on electrodes	111
A6	Effect of varying operating frequency	111
A7	Merits of the DEP filters vis-à-vis existing technology	112

Appendix B

B1	Derivation of generalized Stokes number (St_g)	121
	Reference	123

LIST OF FIGURES

	Page
Figure 1.1: Particle size distribution of (A) fog and (B) particulate matter in nature. (C) Fog droplet size distribution from a cooling tower.	30
Figure 1.2: The diurnal variation in particulate matter (PM) fractions during (A) foggy conditions and (B) typical winter conditions, near Dhanbad in India, observed during the early hours of winter morning. Mass concentration of PM 1 and PM 2.5 as fractions of PM 10 were 72% and 82% higher, respectively under foggy conditions than in normal winter days. Presence of fog significantly elevates the concentration of PM2.5 and PM1 concentrations.	31
Figure 1.3: Dispersed phase filtration by the various mechanisms of impaction, interception, Brownian motion, and electrostatic attraction.	32
Figure 1.4: An air purification device using electric field.	34
Figure 1.5: Community based natural water harvesting in Peru.	36
Figure 1.6: (A) Schematic showing the mechanism of the fog collection on a spine of the cactus plant. (A – C) A time-lapse image progression showing collected fog water droplets directed towards the trichome at the base of the spine. The deposited drop (1) and the coalesced drops (2–4) coalesce, and directed towards the base (black arrows) to form a large drop (1+2+3+4+5). A new cycle of water collection begins after the absorption of the coalesced drops. Scale bars, 100 μm (b) and 500 μm (C).	37
Figure 1.7: (A) Fog Water Collector (FWC) as proposed by Schemenauer and Cereceda for providing drinking water for communities. (B) Cylindrical collector design Warka Water	39
Figure 1.8: (A) Schematic of a cooling tower fog harvester. (B) Meshes of various SC (porosities), geometry placed at the plume of a thermal power plant cooling tower by Ghosh et al.	39
Figure 1.9: (A) Electrostatic field- based aerosol separation occurring on a charged cylindrical precipitator. (B) The percentage of particle penetration through the filter (with only the cylinder) varies with the electrical mobility diameter (d_m) for different applied voltages to the copper cylinder. Higher voltages result in improved capture efficiency, even for larger particle sizes.	42
Figure 1.10: The trajectories of fog droplets around a cylinder are depicted in (A) with and (B) without the application of an electric field. The mesh fiber, represented as a grey circle, is grounded, while the air stream is charged using a metal needle (emitter electrode). The schematic illustrates air streamlines and droplet trajectories, with photographs showing droplet trajectories in the (C) absence and (D) presence of an electric field. In (D), droplets are observed closely following the electric field lines. The inset in (B) illustrates the additional electric force acting on a droplet. Both cylinders in (B) and (D) have a diameter of 1.88 mm. Photographs in (E) display the collection mesh	

and the storage beaker for collected water after 30 minutes of exposure. With high voltage, 30 ml of water was collected, while only three droplets were collected without an electric field. (F) illustrates the deposition efficiency of five meshes as a function of Ke , where Ke represents the ratio of electric and viscous forces. 43

Figure 1.11: Diagram (A) illustrates the principle of the fog-liquefier, while (B) shows the physical installation of the mesh in a paddy field in Japan. (C) The relationship between the liquefying rate or collection efficiency (η_{dr}) and the liquefying index ($\xi = \eta_{dr} / \text{electric power consumption}$) [%/Watt] as a function of applied voltage. The parameter D represents the inter-electrode separation between the corona wire and the mesh. (D) The dependence of fog liquefying rate on air velocity. 44

Figure 1.12: (A) Schematic showing fog flow and their deflection when passing through a woven mesh surface and a contour plot of the fog-harvesting efficiency. The enlarged portion marked in red, focuses on the interaction between the incoming fog droplets and a horizontal member of the woven mesh element. Fog droplets at the vicinity of the fiber are trapped and collected, while those at the periphery follow the streamline around the wire and escape. Droplets on the wire coalesce, and once they grow past a threshold size, they drain under gravity. Two adverse factors affecting collection efficiency are re-entrainment of collected fluid and clogging of mesh pore. A threshold for maximum and minimum droplet sizes to avoid (B) re-entrainment and (C) clogging respectively is depicted as contour plots, marking regions of stability of the drop on mesh as a function of drop radius. 46

Figure 1.13: (A) Photograph of the fog harvesting installation made by [79, 80] at a farm in USA. (B) Photographs showing the issue of tangling for harps of various wire diameters and pitches, under heavy fogging [82]. 46

Figure 1.14: Rationale of the study: A. explore the possibility of enhancement in deposition efficiency of particulate matter (PM) on meshes through electrohydrodynamic mechanisms. B. Explore enhancing the aerodynamic efficiency of fog/PM collection meshes, resistant to clogging, through the redesign of traditional interwoven metal mesh structures, optimizing parameters like mesh fiber diameter, pitch, and fiber wettability. 53

Figure 2.1: Representative schematic of the proposed DEP based air filtration system for personal-level (top) or industrial (bottom) air-filtration system. Droplets (5 – 50 μm diameter) are arrested on the charged mesh that has a 3-phase traveling voltage imposed on its electrically conducting parallel fibers that also act as electrodes. The cross fibers (grey) are insulating in nature and maintains the safe inter-electrode distance to avoid voltage breakdown. INSET Geometric arrangement of electrodes in the charged mesh of the active filter. The droplets are shown to be moving with free stream velocity U towards the electrodes. The insulating members of the filter are not shown in the inset. 56

Figure 2.2: The geometric, flow and the electric field arrangements. (A) The configuration of the electrodes (red circles) having radius of a and spaced out at distance s apart. A droplet/particle (the black circle) of diameter d_p is advected towards the electrodes with a free-stream velocity of U . (B) Sequence of the 3-phase traveling voltage of magnitude Φ_0 and frequency f applied on the electrodes. (C) The electrostatic potential field Φ , and (D) the square of the electric field intensity (E^2) at different time instants (of the time period T) to describe the traveling nature of the fields. (E) The normalized velocity field u/U responsible for advecting the droplets. **61**

Figure 2.3: Particle trajectories for (A and C) $d_p = 5.0 \mu\text{m}$ and (B and D) $d_p = 50 \mu\text{m}$ during DEP capture with mesh of fiber radius $a = 50 \mu\text{m}$ and inter-electrode spacing (A and B) $s = 2500 \mu\text{m}$, and (C and D) $s = 2500 \mu\text{m}$ operating at a 3-phase traveling-voltage, with a nominal field strength of $E_0 = 2.8\text{kV/mm}$ and frequency $f = 50 \text{ Hz}$. A free stream velocity $U = 2.5 \text{ m/s}$ is considered. Brownian fluctuation is more prominently observed for the smaller particle, i.e., for $d_p = 5.0 \mu\text{m}$. Both the axes are normalized by s . **63**

Figure 2.4: (A) Occurrence of capture Π mapped as functions of their transvers position of release ($-1 \leq y/s \leq +1$ at the inlet plane) and the inlet flow velocity U (0.5, 1, 2.5, 5 and 10 m/s), in absence of any electric field, for a constant fiber radius $a = 50 \mu\text{m}$. Fiber spacing and particle size are varied as $s = 500 \mu\text{m}$ (A1, A3) and $2500 \mu\text{m}$ (A2, A4) and $d_p = 5 \mu\text{m}$ (A1, A2) and $50 \mu\text{m}$ (A3, A4), respectively. (B1 through B4) Identical parametric plots under the same conditions, except that a 3-phase AC voltage (at $f = 50 \text{ Hz}$) is now imposed on the electrodes with electric field strength (Φ_0/s) of 2.8kV/mm . Each data-point represents the outcome of 5 simulations under identical set of parameters, yielding 6 discrete values of Π . Colour legend: $\Pi = 5/5$ (red), $4/5$ (yellow), $3/5$ (green), $2/5$ (cyan), $1/5$ and 0 (shown together in blue). Grey-shaded regions indicate the obstruction in flow path by the fibers/electrodes. **66**

Figure 2.5: Effect of varying the electric field on Π vs y/s plots for different inlet flow velocity U (0.5, 1, 2.5, 5 and 10 m/s) for a fixed fiber radius $a = 50 \mu\text{m}$ and particle size $d_p = 10 \mu\text{m}$. Variation of $E = (\Phi_0/s)$ is obtained either by keeping the voltage constant at $\Phi_0 = 1.4 \text{ kV}$ and varying the inter-electrode spacing as (A) $s = 500 \mu\text{m}$, (B) $s = 1500 \mu\text{m}$ and (C) $s = 2500 \mu\text{m}$, or by (D) adjusting the applied voltage at $\Phi_0 = 4.2 \text{ kV}$ while maintaining the inter-electrode spacing $s = 1500 \mu\text{m}$. For all cases, 3-phase AC at $f = 50 \text{ Hz}$ is used. The imposed electric field magnitude scales with (Φ_0/s) , implying that the E fields in (A) and (D) are the same, while those in (B) and (C) are, respectively, $1/3^{\text{rd}}$ and $1/5^{\text{th}}$ of that in (A). Colour legend: $\Pi = 5/5$ (red), $4/5$ (yellow), $3/5$ (green), $2/5$ (cyan), $1/5$ and 0 (shown together in blue). Grey-shaded regions indicate the obstruction in flow path by the fibers/electrodes. **69**

Figure 2.6: Effect of varying the frequency of imposed electric field ($f \in [50, 8000]$ Hz) on Π vs y/s plots for three different particle size, viz., (A) $d_p = 5 \mu\text{m}$, (B) $d_p = 10 \mu\text{m}$, and (C) $d_p = 50 \mu\text{m}$. For all the cases, $U = 2.5 \text{ m/s}$, $s = 2500 \mu\text{m}$ and $a = 50 \mu\text{m}$ and, $\Phi_0 = 7 \text{ kV}$, corresponding to a nominal electric field $E = 2.8 \text{ kV/mm}$. Colour legend: $\Pi = 5/5$ (red), $4/5$ (yellow), $3/5$ (green), $2/5$ (cyan), $1/5$ and 0 (shown together in blue). Grey-shaded regions indicate the obstruction in flow path by the fibers/electrodes. 71

Figure 2.7: Average capture efficiency, η_a , (computed over 100 runs), plotted against the $\frac{\tau_r}{\tau_f} = \frac{f \times s}{U}$ for different particle size and flow velocity, U (A) 1 m/s (B) 2.5 m/s and, (C) 5 m/s for the densest filter ($a = 50 \mu\text{m}$, $s = 500 \mu\text{m}$) is plotted. The electric field strength (Φ_0/s) has been maintained at 2.8 kV/mm . As frequency increases, local maxima and minima appear, indicating a critical factor in designing dielectrophoretic filters. η_a exhibits cyclic maxima and minima as the frequency is varied over the spectrum $f \in [50, 8000]$ Hz. 74

Figure 2.8: Average capture efficiency map, with η_a plotted against $\frac{\tau_{St}}{\tau_{DEP}} = \frac{C\epsilon_0\epsilon_r K_{CM} d_p^2}{12\mu U s} \left(\frac{\Phi_0}{s}\right)^2$ and the $\frac{\tau_r}{\tau_f} = \frac{f \times s}{U}$ within the parametric operation regimes of $U (\in [0.5 - 10] \text{ m/s})$ and $f (\in [50, 8000] \text{ Hz})$, for four different particle sizes. For all simulations the mesh geometry is constant, i.e., $a = 50 \mu\text{m}$ and $s = 500 \mu\text{m}$, and $E_0 = 2.8 \text{ kV/mm}$. The white regions, lying beyond the dotted black lines, represents conditions beyond the regimes of current investigation. 77

Figure 2.9: Average capture efficiency map, with η_a plotted against $\frac{\tau_{St}}{\tau_{DEP}} = \frac{C\epsilon_0\epsilon_r K_{CM} d_p^2}{12\mu U s} \left(\frac{\Phi_0}{s}\right)^2$ and the $\frac{\tau_r}{\tau_f} = \frac{f \times s}{U}$ within the parametric operation regimes of $U (\in [0.5 - 10] \text{ m/s})$ and $s (\in [500, 2500] \mu\text{m})$, for four different particle sizes. For all simulations $a = 50 \mu\text{m}$ and $f = 50 \text{ Hz}$, and $E_0 = 2.8 \text{ kV/mm}$. The white regions, lying beyond the dotted black lines, represents conditions beyond the regimes of current investigation. 77

Figure 2.10: Normalized pressure drop as a function of s/a computed from the analytical solution of Miyagi [113]. The INSET displays the dimensional pressure drop across filters for $a = 50 \mu\text{m}$, meeting the condition $s/a \in [10, 50]$, for different free stream velocities. The operational regime of the present study is highlighted in red. 79

Figure 3.1: (A) Traditional interweaved metal meshes are prone to clogging of mesh pores. Mesh clogging has strong dependence on the apparent contact angle of the liquid droplet on the fiber surface (inset). (B) A typical mesh arrangement in cooling tower fog harvesters [32] showing deposited and detached droplets. (C) A growing droplet on a thin fiber can undergo dramatic morphological variations: from axisymmetric barrel shaped droplets to clamshell shapes. 82

Figure 3.2: (A) Schematic of the sample preparation process: (i) to achieve superhydrophilic (SHPL) properties, the mesh fibers are etched in a 3M HCl

solution followed by passivation in boiling water and (ii) to render the mesh fibers hydrophobic (HPB), they are dipped in PDMS solution followed by hot air drying in an oven. (B) Experimental setup with a computer display (i) and an illuminated white background (ii) to capture droplet morphology on a wettability-engineered metal fiber (iii, the zoomed-in section). The metal fiber was held by a horizontally placed three-way chuck (iv), which in turn was affixed to a firm stand (v). (C) Schematic of the arrangement for droplet volume addition using a micropipette. The volume was incremented, in steps of the least dispensable volume (V_{LD}) of the micropipette, until the droplet detached at V_{CR} . (D) A vertically oriented mesh positioned orthogonally to the path of fog to observe fog deposition, droplet capture on mesh fiber and drainage.

84

Figure 3.3: (A) Estimation of droplet dimensions via image processing in Python. Final images from the evolved surfaces were stored and later processed. ROI = Region of interest. (B) SE simulation results for variation of droplet dimension (H and W) with change of V_R until droplet detachment for a 1.27 mm diameter fiber and three different wettability levels.

87

Figure 3.4: Clamshell droplet morphologies (for varying V_R) on wettability engineered fibers, as observed during experimentation. Droplets on SHPL fibers (A), were seen to spread laterally and had a greater lateral extent. Droplets on control fibers (untreated SS) showed no preference in change of lateral or vertical spread on increase of droplet volume (B), whereas droplets on HPB surfaces minimized their contact area while extending vertically with increase of volume (C). Comparisons between lateral and vertical extent of varying drop-on-fiber morphologies have been carried out in the next section. All experiments were carried out until the droplet reached the critical volume of detachment (V_{CR} , as seen in the last frame from each sequence), any volume addition after this would lead to droplet detachment. All images have the same scale bar, while each image show a fiber of diameter 2.7 mm.

89

Figure 3.5: (A) Measurement of maximal width (W_{max}) and maximal vertical hang (H_{max}) in droplets hanging from 1.27 mm (top, droplet volume 10 μL) and 4 mm (bottom, droplet volume 45 μL) fibers (stainless steel 304, $\theta \sim 70^\circ$). Each figure comprises of two halves: the left half (colored in green) corresponds to SE simulations, while the other half is an experimental image. (B) Rationale for the design of *clog-proof* mesh with square pores (B1) and rectangular pores (B2): The mesh pitch should be such that a symmetrically growing droplet should not touch any other fiber, either on the side or at the bottom, as it grows until its detachment. The mesh pore dimensions, viz., the pore height and width have been marked as p_H and p_W respectively. (C) Fog droplets growing from the middle of the mesh pore have a greater probability of clogging the mesh (marked in dashed white box), while droplets near a vertical fiber (marked in dashed yellow box) can drain down after contact with the nearest vertical fiber).

91

Figure 3.6: Variation of (A) the maximal droplet dimension ($Max\{H_{max}, W_{max}\}$) with the fiber radius, for the estimation of the minimum mesh pitch (as per Equation 2 or 3), and (B) the corresponding pore dimension maximal aspect ratio ($AR_m = H_{max}/W_{max}$, for the estimation of the minimum mesh pitch of a rectangular mesh as per Equation 3), plotted as functions of the fiber diameter for different mesh wettability. Legend: Filled symbols with dotted lines denote SE simulation results, half-filled circles denote the experimental data. Vertical dotted lines in both figures, mark the capillary length scale of water (~ 2.7 mm). (C) A series of experimental images showing the $AR=H/W$ calculated at the respective V_{CR} for different control fiber diameters ($\theta = 73^\circ$); H and W are marked in yellow and blue, respectively. 94

Figure 3.7: (A) Schematic of flow through a mesh placed in the path of fog laden wind (after Steiros [155]). Flow in *Region 1* deviates and goes around the mesh; fog within the upstream cross-sectional area A_I (less than the projected mesh area) interacts with the fog mesh. *Region 2* occurs just after the mesh, while *Region 3* is located at far downwind where mixing of flows from *Regions 1* and *2* occur. (B-i) Variation of the *clog-proof* SC values with the mesh fiber diameter for different fiber wettability. The *clog-proof* SC is calculated corresponding to the minimum mesh pitch lengths for square-pore fog meshes as suggested in Figure 6A. Regions above each curve (corresponding to a greater SC for a particular fiber diameter and wettability) are prone to clogging. Background color map denotes the corresponding aerodynamic efficiency as evaluated from (B-ii), which describes the variation of aerodynamic efficiency (also the black dashed curve) with the SC for square-pore fog-harvesting meshes. The color map background in (B-ii) is the same as that in (B-i), for easy comparison of η_a with *clog-proof* SC s. 98

Figure 3.8: (A) Optimal shade coefficients for varying fiber diameter and wettability. The optimal mesh SC is calculated corresponding to *clog-proof* mesh pitch lengths from Figure 3.6-A. Regions above each curve (for a specific level of fiber wettability) are prone to clogging (trends with only 3 representative fiber-wettability are shown for clarity). (B) The resulting maximum achievable aerodynamic efficiency for *clog-proof* square meshes as a function of fiber diameter for different fiber wettabilities. 99

Figure 3.9: (A) Variation of deposition efficiencies (η_d) as function of fiber diameters at different fog flow velocities as evaluated from Equation 14 for $St_g \leq 0.14$ and from Equation 15 for $St_g > 0.14$. η_d resulting from $St_g = 0.14$ has been marked with a dashed red line. (B) Variation of ($\eta_d \times \eta_a$) at different optimal *clog-proof* shade coefficients for different mesh fiber diameters and wettability conditions. Total efficiencies have been estimated for a representative fog flow velocity of 5 m/s. 102

Figure A1: vdbdb 114

Figure A2: Extent of stochastic behavior of the particles trajectories for (A) $d_p = 5.0 \mu m$ and (B) $d_p = 50 \mu m$. For both the cases, $a = 50 \mu m$, $s = 2500 \mu m$, the 3-phase

traveling-voltage $\Phi = 7$ kV (corresponding to $E_0 = \Phi_0/s = 2.8$ kV/mm) at $f = 50$ Hz and the inlet flow has $U = 2.5$ m/s. Brownian walk is prominently observable in smaller particle size. For each case, trajectories of ten identical particles, released from the same transverse position of the inlet plane are superposed.

115

Figure A3: Comparison of the time-averaged spatial distribution of E^2 field for (A) $s=500$ and (B) $2500 \mu\text{m}$, averaged over the time period of the 3-phase traveling wave with $f = 50$ Hz. The applied voltage to the electrode corresponds to $E_0 = 2.8$ kV/mm.

116

Figure A4: (A) Occurrence of capture Π mapped as functions of their transvers position of release ($-1 \leq y/s \leq +0.9$ at the inlet plane) and the inlet flow velocity U (0.5, 1, 2.5, 5 and 10 m/s), in absence of any electric field, for a constant fiber spacing $s = 1500 \mu\text{m}$. Fiber radius and particle size are varied as $a = 50 \mu\text{m}$ (A1, A3) and $150 \mu\text{m}$ (A2, A4) and $d_p = 5 \mu\text{m}$ (A1, A2) and $50 \mu\text{m}$ (A3, A4), respectively (B1 through B4). Identical parametric plots under the same conditions, except that a 3-phase AC voltage (at $f = 50$ Hz) is imposed on the electrodes with nominal electric field strength $E_0 = 2.8$ kV/mm. Each data-point represents the outcome of 5 simulations under identical set of parameters, yielding 6 discrete levels of Π . Colour legend: $\Pi = 5/5$ (red), $4/5$ (yellow), $3/5$ (green), $2/5$ (cyan), $1/5$ and 0 (shown together in blue). Grey-shaded regions indicate the obstruction in flow path by the fibers/electrodes.

117

Figure A5: Spatial distribution of Π on the U - y/s plane under DEP capture, demonstrating asymmetric patterns around electrodes, influenced by electric field gradients and phase sequence in a 3-phase voltage waveform. The phase is sequentially advanced by $\frac{2\pi}{3}$ from A to C.

118

Figure A6: The impact of varying the frequency ($f \in [50, 8000]$ Hz) of the imposed electric field, corresponding to $E_0 = 2.8$ kV/mm, on Π vs y/s . The trend aligns with the non-monotonic variation in particle capture dynamics depicted in Figure 6, underscoring the interplay of the DEP and drag force (viz. for $U = 1$ m/s and 5 m/s). Particle sizes are varied as $d_p = 5.0 \mu\text{m}$ (A-i - ii), $d_p = 10 \mu\text{m}$ (B-i - ii), and $d_p = 50 \mu\text{m}$ (C-i - ii).

119

List of Tables

	Page
Table 1.1: Efficiency of particulate matter removal when utilizing a HEPA filter.	34
Table A1: Comparison of filtration efficiency, pressure drop across the filters and their respective quality factor	112

ABSTRACT

Keywords:

Polydispersed phase flow; Electrohydrodynamics; Dielectrophoretic force; 3-phase voltage; Air filtration; Tunable capture efficiency, Fog harvesting; Droplet morphology; Droplet detachment; Wettability engineering; Surface Evolver simulation; Fog harvesting mesh design; Capture efficiency

In the field of air filtration and fog harvesting, optimizing mesh and filter designs is essential to achieve high deposition efficiency while minimizing pressure drop and clogging issues. Existing challenges include, in one hand, the development of filters/ meshes that balance the mutually conflicting requirements of high capture efficiency and low pressure drop, while on the other hand, it is also imperative that the filters/meshes are able to maintain clog-free operation. Dense meshes offer high deposition efficiency but increased pressure drop across the mesh filter, while rarer filters offer a low pressure drop, but at the expense of deposition efficiency. Dense meshes would also tend to get clogged more often, while filtering a dispersed liquid phase, for example fog, from a gas stream. Addressing these challenges requires a broad understanding of the transport of dispersed phase of liquid droplets as they pass in a gas stream over a filter strand, and also the interaction of the deposited liquid with the mesh fibers.

The present work strives achieve these objectives by focussing on two broad attributes of the transport of finely divided dispersed phases over fibers and meshes. In the first part, transport and separation of a dispersed phase using the principle of dielectrophoretic separation is investigated numerically to identify the conditions favourable for a high filtration efficiency and low pressure loss. The second part deals with deciphering the interaction of the dispersed liquid phase with the filter-fibers and developing a mesh design that is resilient to clogging, thus ensuring high capture efficiency. Tunable filtration of dispersed droplets from a gas-stream is central to several engineering applications. While the literature in filtration science is rich, and the technology is also mature, separation of dispersed phases of large polydispersity with minimal pressure loss remains to be a challenge. The present study investigates the efficacy of dielectrophoresis (DEP) for the separation and collection of a dispersed phase from a stream of particulate two-phase flow through a detailed numerical simulation. The dispersed phase consists of water droplets of varying diameters transported in an air stream. The DEP filter is modelled as an array of cylindrical metallic fibers which serve both as filtration elements and as the electrodes with a three-phase applied voltage. The influence of the particle inertia, viscous drag, DEP and random Brownian forces on the overall particle trajectory and capture are elucidated by numerical simulations. The filtering efficiency is assessed through statistical analysis of the simulation results, encompassing the effects of applied electric voltage, frequency modulation, droplet diameters, fiber (electrode) diameters, inter-fiber distances and a wide range of air velocities. The study reveals a distinctive pattern in the capture efficiency for different particle diameters and inter-fiber spacing as a function of the frequency of the applied voltage and identifies the optimal frequencies where the droplet capture efficiency attains peak values. These frequencies exhibit a significant correlation with a single dimensionless parameter representing the residence time of particles in the vicinity of the filter. Findings from the work offer valuable insights for designing DEP-based active filtration systems of high filtration efficiency and tunable operating regime, while maintaining low pressure drop and a high quality factor (Q_F), thereby lending to its better deployment in crucial healthcare environments, advanced face masks, home air filters, and even in industrial settings like oil-vapour extraction. While for a regular filtration of the dispersed phase from a low-density suspension, maintaining a high capture efficiency and, at the same time, a low pressure drop is a key challenge, an additional problem arises if the dispersed phase has a high liquid content, such as in the event of fog harvesting. Fog harvesting relies on intercepting atmospheric or industrial fog by placing a porous obstacle, e.g., a mesh and collecting the

deposited water. In the face of global water scarcity, such fog harvesting has emerged as a viable alternative source of potable water. Typical fog harvesting meshes suffer from poor collection efficiency due to aerodynamic bypassing of the oncoming fog stream and poor collection of the deposited water from the mesh. One pestering challenge in this context is the frequent clogging up of mesh pores by the deposited fog water, which not only yields low drainage efficiency but also generates high aerodynamic resistance to the oncoming fog stream, thereby negatively impacting the fog collection efficiency. Minimizing the clogging is possible by rendering the mesh fiber superhydrophobic, but that entails other detrimental effects like premature dripping and flow-induced re-entrainment of water droplets into the fog stream from the mesh fiber. The present work improvises on the traditional interweaved metal mesh designs by defining critical parameters, viz., mesh pitch, shade coefficient, and fiber wettability, and deduce their optimal values from numerically and experimentally observed morphology of collected fog-water droplets under various operating scenarios. The numerical simulation uses an open-source surface evolver platform that predicts the shape of a given volume of liquid (e.g., the water collected from the fog) as a function of mesh fiber radius and wettability, while the experiments are conducted to validate the predictions. Based on the maximal size of the liquid droplets that would hang from a horizontal fiber before it would detach by gravity, the present study sets a criterion of mesh pitch for a given range of fiber wettability and radius. The study is further extended over a varying range of mesh-wettability, including superhydrophilic and hydrophobic surfaces, to find optimal shade coefficients which would theoretically render clog-proof fog harvesting meshes. The aerodynamic, deposition, and overall collection efficiencies are characterized for different designs of the fog-harvester. For clog-proof meshes with fiber diameters above the capillary length scale, mesh wettability is found to play very little role in determining the overall efficiency. Further, the overall efficiency is found to decrease with increase of fiber diameter. Such a trend can be attributed to the fact that the optimally-designed clog-proof meshes, with a square pore, have a constant aerodynamic efficiency corresponding to an optimal SC of 0.52 at larger diameters and the trend in overall efficiency is directly influenced by the decreasing deposition efficiency of larger fibers. Findings of the study serves as the baseline criteria for design of high-efficiency fog harvesting meshes.

Chapter 1
INTRODUCTION

1. Motivation and prelude

Fog, smog, and haze are atmospheric occurrences characterized by the presence of water droplets and particulate matter (PM), either individually or in combination, suspended in the air. Fog typically appears as micron-sized water droplets suspended in air, occurring in diverse situations ranging from natural landscapes (such as in the hills or in some coastal areas) to industrial settings (such as in cooling tower plumes and spray ponds). Fog is typically characterized by diverse physical attributes such as particle/droplet loading (number and volumetric concentration) and particle size distribution. The size of fog droplets can vary – typically between 1 and 25 μm [1] (**Figure 1.1-A and B**) – depending upon atmospheric conditions prevalent during the formation of the fog through condensation of airborne water vapor, whereas fog from industrial sources such as cooling tower has an average diameter of 5-100 μm [2].

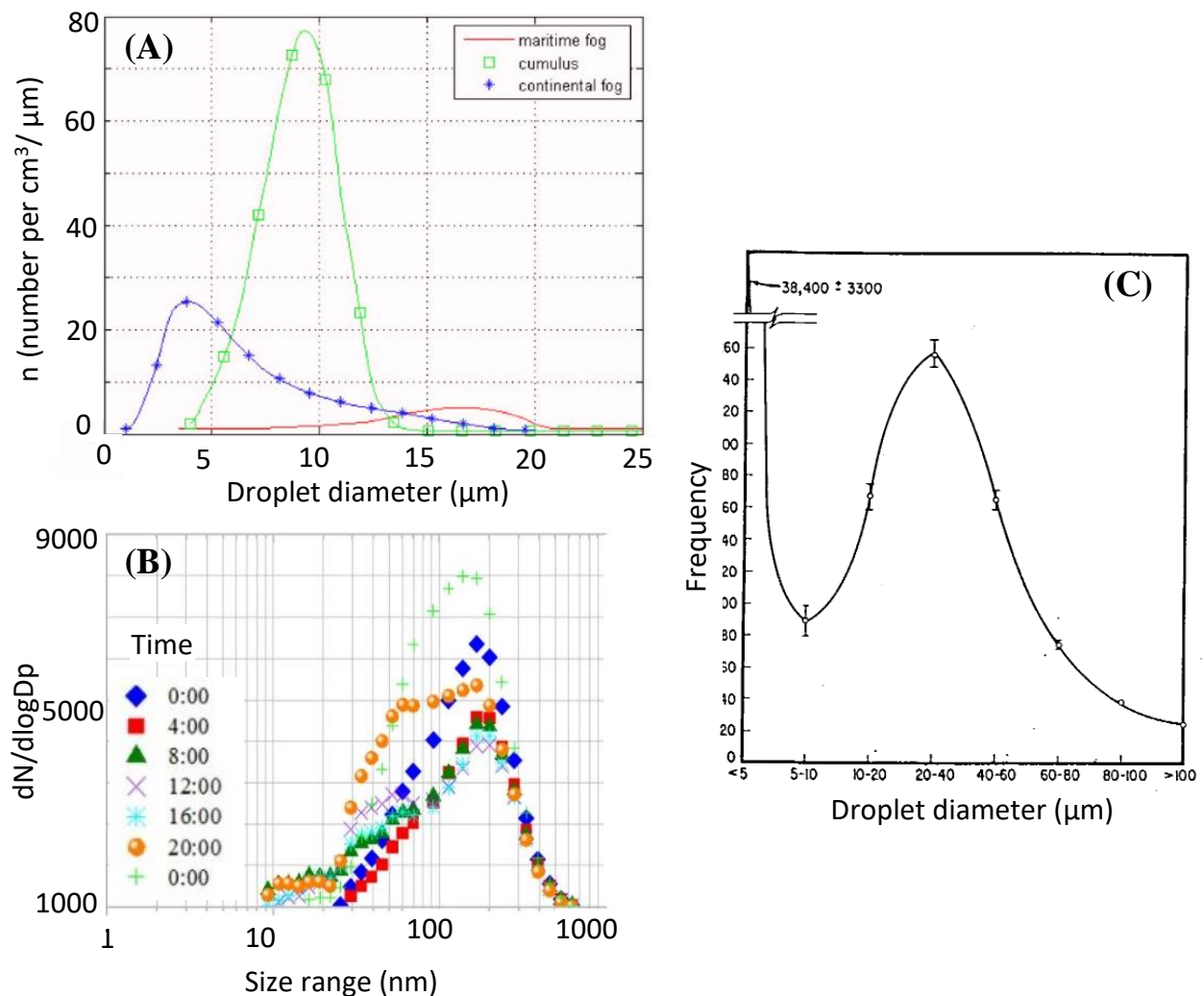


Figure 1.1 Particle size distribution of (A) fog and (B) particulate matter in nature. (C) Fog droplet size distribution from a cooling tower. (Reproduced with permission from [1, 2 and 3])

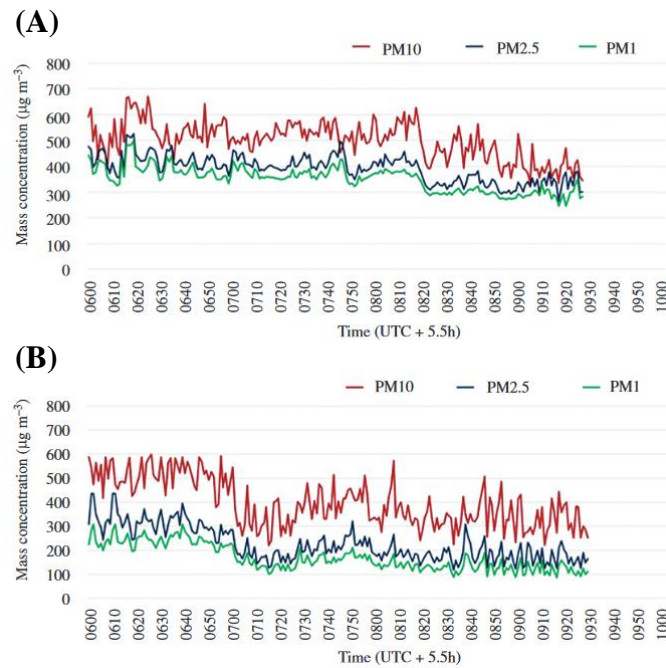


Figure 1.2 The diurnal variation in particulate matter (PM) fractions during (A) foggy conditions and (B) typical winter conditions, near Dhanbad in India, observed during the early hours of winter morning. Mass concentration of PM 1 and PM 2.5 as fractions of PM 10 were 72% and 82% higher, respectively under foggy conditions than in normal winter days. Presence of fog significantly elevates the concentration of PM2.5 and PM1 concentrations (Reproduced with permission from [4]).

Haze, in contrast, is made up of micron-sized particles of dust, salt, or other substances suspended in the air, with particle sizes generally ranging from 0.01 to 1 μm [3] (see **Figure 1.1-B**). Fog from industrial cooling towers often produce a bimodal distribution of number density, with peaks at $\sim 20 \mu\text{m}$ and smaller than 5 μm (see **Figure 1.1-C**). Smog, on the other hand, forms under conditions of high relative humidity (over $\sim 95\%$) when atmospheric water vapor nucleates on airborne suspended particulates [4]. Recent increases in fog-related events have been linked to elevated levels of dispersed particulate matter in the atmosphere [5, 6].

As illustrated in **Figure 1.2**, presence of fog has been found to elevate the persistence of suspended particulate matters concentrations noticeably [4, 7]. A combination of PM and fog particles forms a dispersed phase in air, drastically reducing visibility and air quality, thereby posing significant health risks. This observation highlights the complex interplay between atmospheric fog and air quality, emphasizing the necessity for diligent monitoring and strategic management of dispersed phases (both fog and particulate matters) to mitigate their impact on environment and public health [8]. The adverse effects of such dispersed phases in atmosphere underscores the crucial role of filtration in maintaining clean and breathable air, a need accentuated by recent public health crises such as the SARS, MERS, and the COVID-19

pandemic. Efficient filtration technologies are, therefore, essential for removing dispersed phases from continuous fluid streams in various environmental and industrial contexts so that the harmful particulates and infectious aerosols are removed from the air. Separation of airborne fog also has its own merit in light of fog harvesting. Capture and harvesting of fog droplets has emerged as a promising alternate source of water, particularly in regions with water scarcity but prone to fog formation, e.g., the coastal regions of Chile, Sudan, etc. [9].

While both air-filtration and fog harvesting share commonalities the principle of separating airborne droplets – both rely on inertial interception, Brownian and electrostatic (in case of active filtration) depositions of the droplets on the designated capture surfaces – they face unique challenges [10]. Capture of dispersed phase occurs with 4 major methods: inertial impaction, interception, Brownian motion and active electrostatic attraction. These capture, or filtration mechanisms are described in **Figure 1.3**.

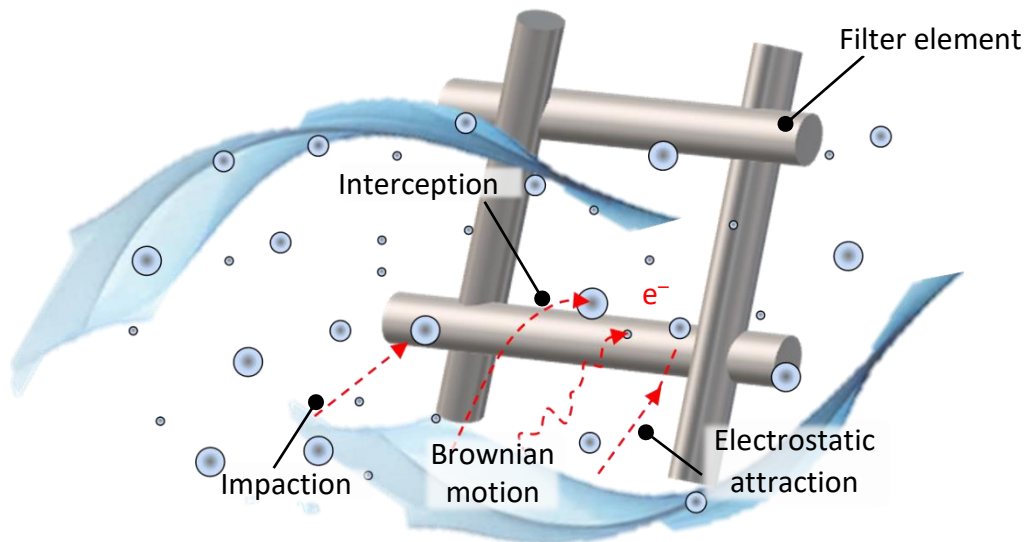


Figure 1.3: Dispersed phase filtration by the various mechanisms of impaction, interception, Brownian motion, and electrostatic attraction. (Reproduced with permission from [10])

Inertial impaction occurs when particles moving along an airstream deviate from rapidly changing streamlines, due to an obstacle placed in its path and directly impact the fiber/filter surface. Inertial impaction remains the predominant filtration process for larger particles and relies on the inertia of the particles. Interception occurs when particles carried are close to the filter surface by streamlines and the particle radii is larger than the inter-fiber distance. The effects of collisions with molecules producing the Brownian motion of particles are quite prominent in particle with very small diameter, which gives particles enough kinetic energy to deviate from their original path, increasing the likelihood of impacting the fiber surface. The other active method of filtration is by electrostatic attraction, where the particles or the filter

mesh is charged to attract the particles onto the mesh filters via Coulombic forces. Alternatively, when either the particles or fibers are neutral, charging one can polarize the other, resulting in attraction by dielectrophoretic forces. Notably, the electrostatic mechanism does not influence the airstream and can enhance filtration efficiency.

A further discussion on the influence of these forces on the equation of motion of particles is illustrated in Chapter 2. For air filtration systems, the target objective is to rid the air stream of suspended particles, while for fog harvesters, it is important to maximize collection of the airborne liquid for downstream utilization. While air-filtration systems typically strive to achieve maximum particulate removal at the expense of minimum pressure drop across the collection systems; for fog harvesting, the primary focus is to maximize drainage of the intercepted and collected fog to the designated collection port.

1.1 Filtration of dispersed phases in air: particulate matter and fog droplets

Amidst rapid industrialization, urban expansion, and population growth, modern society grapples with a myriad of challenges, ranging from deteriorating air quality to water scarcity. These challenges, exacerbated by the aftermath of the industrial revolution, are amplified by the continuous expansion of urban areas and industrial zones. Consequently, air pollution, characterized by elevated levels of particulate matter and other harmful pollutants, poses a significant threat to public health, particularly impacting vulnerable communities with increased susceptibility to respiratory ailments. Despite advancements in filtration technology, challenges persist, including substantial pressure drops across filters, low filtration efficiency, clogging-up of filter pores, and sensitivity to operating parameters. The need for personal air purification devices, such as household air purifiers and face masks, underscores the importance of achieving high capture efficiency while minimizing pressure drop across the filters.

1.1.1 Air filtration: Separation of suspended particulate matter in air

Traditional air filters like High Efficiency Particulate Air (HEPA) filters have played pivotal role in maintaining air quality and addressing waste gas treatment and have shown great efficiency in removing particulate of all sizes, as shown in **Table 1.1** [11]. These filters explore sieving, inertial impaction, interception, and diffusion [12, 13].

To enhance the removal of particles via mechanical means, the filters commonly incorporate fine fibrous materials characterized by diminutive fiber diameters and inter-fiber distances spanning from 0.1 to 10 μm , often accompanied by low porosity within the range of 0.5 to 10% [14, 15]. Nevertheless, this approach often entails a trade-off, manifested as increased pressure

losses across the filters, potentially compromising energy efficiency and user comfort, especially in face-mask applications. Another crucial drawback in the traditional filtration system is their selectivity to the specific particle size – while fine filters get easily clogged by the larger particles, coarser filters exhibit poor filtration against the smaller ones. This poses serious challenge when the oncoming dispersed phase has a large polydispersity index, for example, in air-filtration system high performance is often sought in the ranges of PM 1 – 2.5 and PM 2.5 – 10, [16, 17, 18], considering their respective compositions and impact on overall air quality [19].

To address these obstacles, electrophoretic air purification offers a viable solution [20] (see **Figure 1.4**), utilizing space-charge injection to enhance the deposition of suspended droplets in filters.

Table 1.1 Efficiency of particulate matter removal when utilizing a HEPA filter
(Reproduced with permission from [11])

PM/Cases	Air purifier I		
	HEPA purifier OFF <i>Mean (95% CI)</i>	HEPA purifier ON <i>Mean (95% CI)</i>	% Decrease
PM _{0.25}	0.39(0.36–0.42)	0.18 (0.16–0.21)	53
PM _{0.5}	193.54 (175.06–212.02)	96.74 (81.77–111.72)	50
PM _{1.0}	480.06 (428.99–531.13)	288.43 (238.56–338.29)	40
PM _{2.5}	561.80 (502.91–620.70)	370.09 (306.34–433.83)	34
PM _{5.0}	612.28 (552.59–671.96)	423.99 (356.09–491.89)	31
PM ₁₀	626.07 (566.25–685.90)	443.62 (373.85–513.40)	29

*Statistical significance was a 5% level ($p < 0.05$).

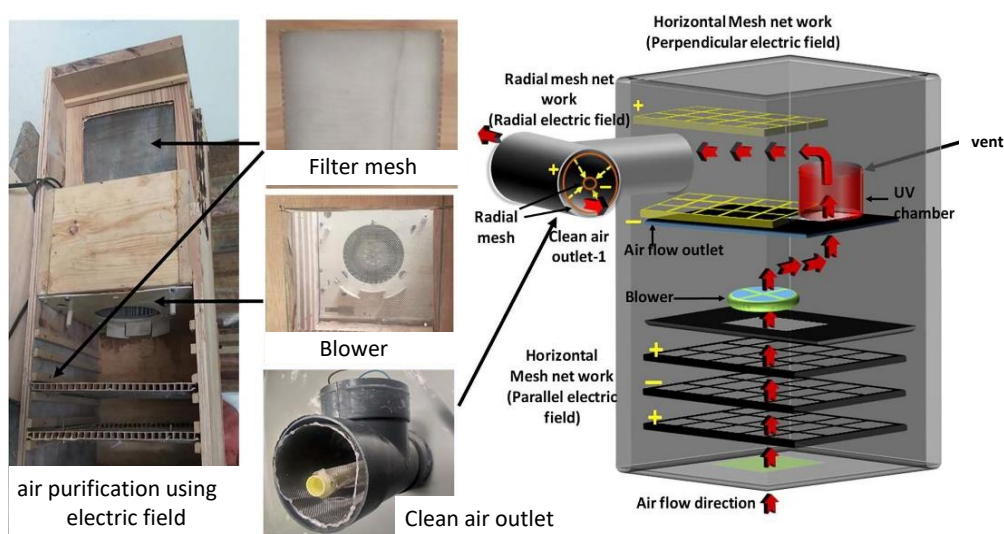


Figure 1.4 illustrates an air purification setup that employs an electric field to capture airborne microorganisms, particles or droplets. (Reproduced with permission from [20])

However, this method necessitates particle ionization, which entails imparting an electrical charge to the medium, which increase the deposition efficiency but limits its applicability in various scenarios. Apart from this, deposition efficiency also suffers when an excessive amount of dispersed phase accumulates on the filter, leading to clogging of its pores. With gradual buildup of the dispersed phase the filter transforms into an impermeable membrane, requiring the flow of the medium be redirected around the filter due to increased resistance. This necessitates the use of fans or additional devices to augment the flow, thereby raising operational costs.

Suspended particulate matter (PM) and virions, which are often enveloped in water [21], underscores the importance of capturing and separating these elements from the air. This is vital for mitigating health risks associated with inhaling contaminated air and also for controlling the spread of infectious diseases transmitted via respiratory droplets [22, 23]. Addressing the challenges in capture and separation of both suspended particulate matter and fluid droplets, such as those present in smog, fog, or released during activities like sneezing, filtration systems can significantly improve air quality and protect public health.

Therefore, strategically designing air filtration systems addresses both health concerns and water resource management.

1.1.2 Fog harvesting: Capture of airborne water droplets as alternate water source

The industrial revolution and a sudden boom in population [24], has put stress on freshwater resources with depleting groundwater sources; contamination of natural water bodies, and disputes over inter-regional water allocation. The World Economic Forum (WEF) classifies water as one of the biggest threats to humanity [25]. This is accentuated by the global rise in temperature and variability in the pattern of rainfall inflicted by climate change [26, 27, 28]. This has led contemporary researchers to look into various sources of freshwater, be it in desalination and purification technologies or innovations in water conservation [29, 30]. Water purification technologies like desalination and reverse osmosis are prohibitively costly. Due to such economic constraints, the potential alternative water resources need to be economically viable and renewable. With the increasing importance and the potential of water in fog, it is now considered as a source of potable water, especially in arid but fog-prone geographies, like the wide swaths of desert lands in Namibia, highlands of Peru and the rugged reaches of Nepal, which faces serious dearth of water, experiences intense fogging. Although Samuel Coleridge had penned the very famous lines, “water water everywhere and not a drop

to drink” on quite a different perspective, it seems quite right in such context. Certain community-based initiatives have come up with an intelligent idea. They strategically placed meshes in the paths of fog-laden wind to capture the fog; water that is collected and stored to be used later for daily utilities (see **Figure 1.5**). BBC reported such a method of water ‘harvesting’ as “the ethereal art of fog-catching”, [31] a title probably most worthy. The focus of fog collection has, in recent years, gravitated towards research in retrieving industrial fog (e.g., capturing drift losses from cooling tower plumes [32]). Such methods can help cut down on the freshwater dependency of industries such as thermal power plants, thereby making freshwater readily available for human consumption. Previous studies have established the feasibility of industrial fog harvesters [32] in capturing fog, for reuse, that would otherwise been lost to the environment. Water captured by a fog harvester depends on the interaction of fog-laden wind with the harvester mesh, examples of which are present in both Nature and industrial applications.

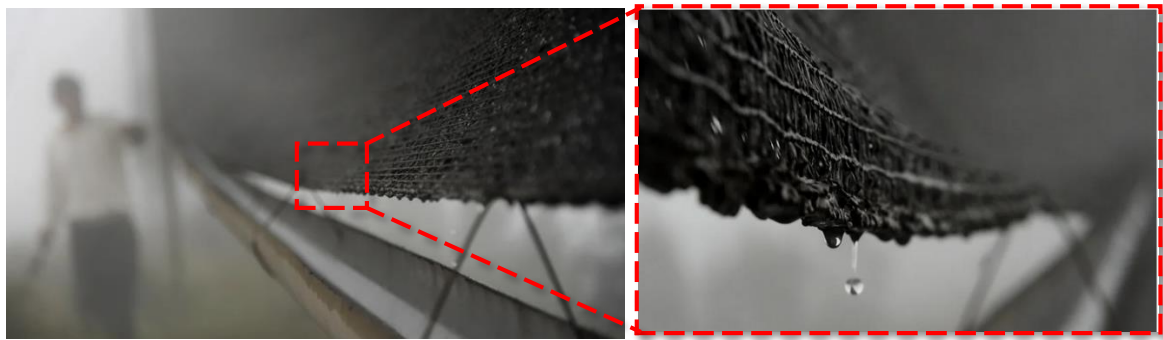


Figure 1.5: Community-based natural water harvesting in Peru.
(Reported from news article 31)

1.1.2.1 Fog harvesting in Nature

Nature has engineered its flora and fauna to survive in the harshest of all environments. The interception of atmospheric fog by such organisms, to complement its needs for water, is an immaculate example of biological processes inspiring bio-engineering applications. Small shrubs and cacti are known to intercept fog particles in fog prone arid areas.

The interception of atmospheric fog with the trees in fog-prone regions helps to collect water from the atmosphere, mostly observed in places of high water-scarcity [33]. Their fog harvesting capability is influenced by variations of their height and leaf structures. Vegetation with small needle-like leaf structures (e.g., cacti) intercept the suspended fog droplets. Fog is intercepted by the obstruction offered by such pattern of leaves and thorn-like structures. These provide minimum resistance to the flow of fog-laden wind while offering maximum surface area [34]. Most of these thorn-like structures have textures, like

in that of *Opuntia microdasys* (type of cactus) [35]. These build a Laplace pressure gradient, aiding in the transport of the deposited droplets towards the trichome at the base. The schematic illustration of the process is shown in **Figure 1.6-A**, and a time-lapse image progression showing the collected fog water droplets directed towards the trichome at the base of the spine is depicted in **Figure 1.6 - B - C**.

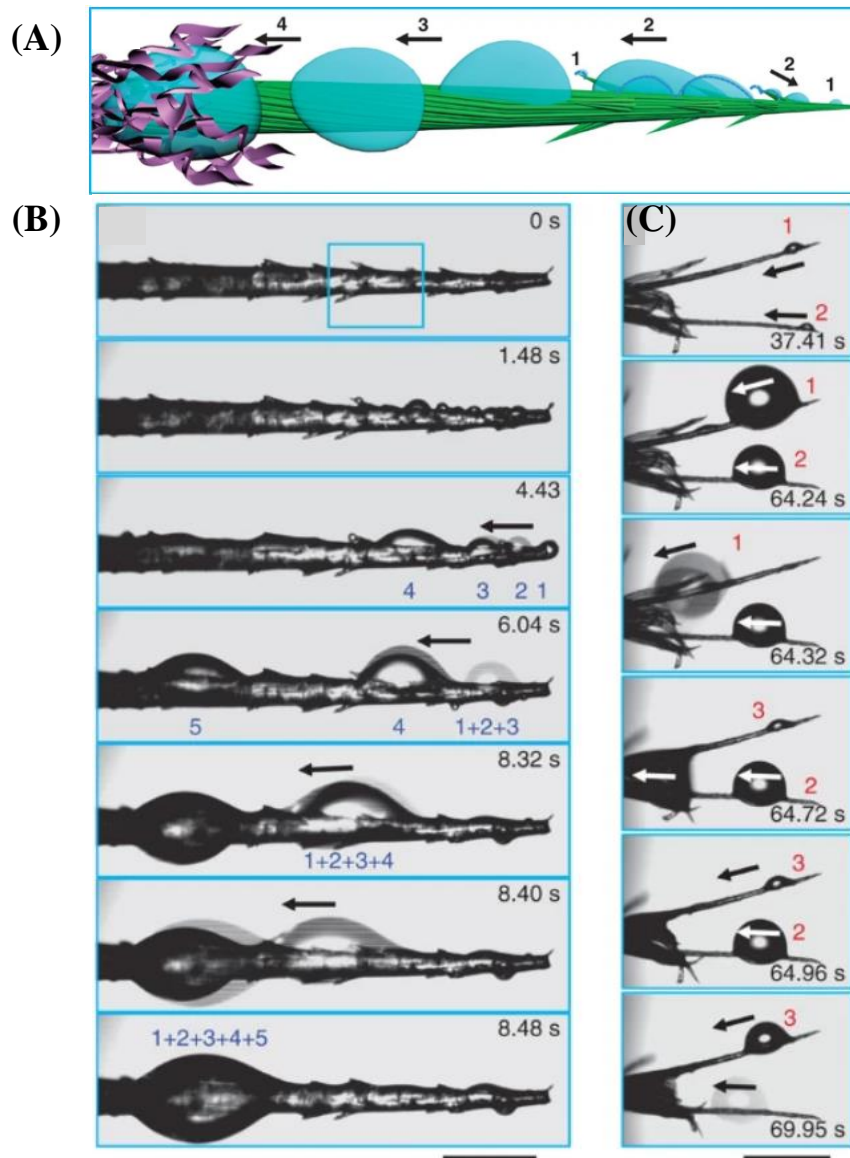


Figure 1.6: (A) Schematic showing the mechanism of the fog collection on a spine of the cactus plant. (B – C) A time-lapse image progression showing collected fog water droplets directed towards the trichome at the base of the spine. The deposited drop (1) and the coalesced drops (2–4) coalesce, and directed towards the base (black arrows) to form a large drop (1+2+3+4+5). A new cycle of water collection begins after the absorption of the coalesced drops. Scale bars, 100 μm (B) and 500 μm (C). (Reproduced with permission from [35])

Several species of desert-animals, mostly insects and reptiles, are endowed with similar body surface features that help meet their water demand by fog-basking. The discovery of water harvesting capability of the *Onymacris unguicularis*, aka the Namib Desert beetle, by Hamilton and Seely in 1976 [36] has inspired a flurry of work in the study of such fauna. The Namib Desert Beetles [37] are reported to meet their water demand by basking in the path of early-morning fog water, collecting upto 12% of their body weight. Favorable wettability features on the elytra (back of the beetle) allows for maximum dew collection [38, 39]. These insects are able to collect such huge quantity of water with the help of contrast wettability spots (superhydrophilic bumps on superhydrophobic background) at their back. Although, the quantity of collected fog-water by the beetle is less effective when compared to the collection by trees, but it still showcases a splendid use of surface wettability to harvest water from fog.

1.1.2.2 Anthropogenic fog harvesting: *Community and industry*

Fog collection for human use started recently in 1994 [40], although a couple of feasibility studies were previously conducted as early as the beginning of 1900s in South Africa [41]. These fog collectors are mostly simple structures with large screens made of polyethylene net meshes, placed orthogonal to fog flow. As the fog droplets impinge on these meshes, they get deposited, coalesce and are collected for collection. The water rolls down the woven structure of the mesh to collectors attached at the lower end of the collectors which drain into the collecting tank. The first edition fog nets [42] were made woven from locally available fibers which and were later replaced with commercial polyethylene based Raschel meshes [43]. Success by early studies inspired many NGOs around the world to successfully implement full-scale fog water harvesting collectors and supplying clean water to satellite communities. Basic fog water collector (FWC) designs consisted of large, planar nets mounted on rectangular frames [44]. These were eventually replaced by more innovative designs, promising higher collection, lower installation cost and maintenance. One such installation by Vittori and Volger [45] called *Warka Water*, proposes the use of Chinese-lantern-shaped outer scaffolding (see **Figure 1.7-B**), with the body made of cylindrical nylon or polypropylene mesh. The water collects in a circular well underneath. The device claims an annual average collection up to 100 L day⁻¹.

Apart from fog water collection from natural sources, recently, a pilot study by Ghosh et al. [32] looked into the possibility of water harvesting from the drift losses in the mouth a cooling tower, of a thermal power plant in India. Mesh integrity is of prime importance in such

applications for steady fog collection. The study estimated that the cooling water load for a 500 MW power plant [46] is around 54000 to 60000 m³h⁻¹, of which ~1.6% is lost per hour, predominantly in the form of evaporative loss, drift loss, and blow-down, which needs to be compensated in the form of make-up water (see **Figure 1.8-A**).

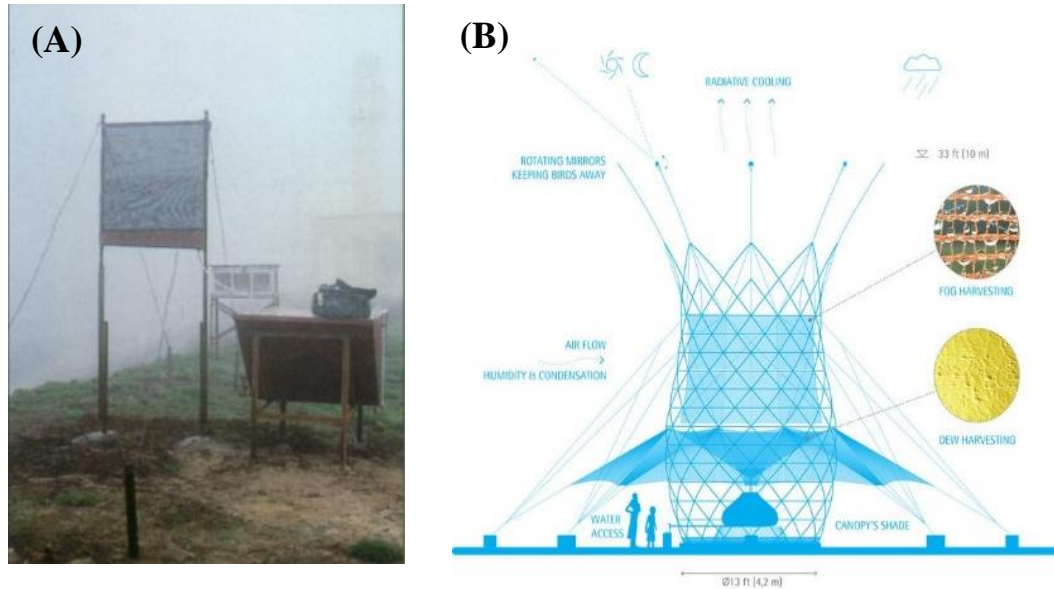


Figure 1.7: (A) Standard Fog Collector (SFC) as proposed by Schemenauer and Cereceda [44] (reproduced with permission) for providing drinking water for communities (B) Cylindrical collector design *Warka Water* [47] (permission not required, taken from open-source online link)

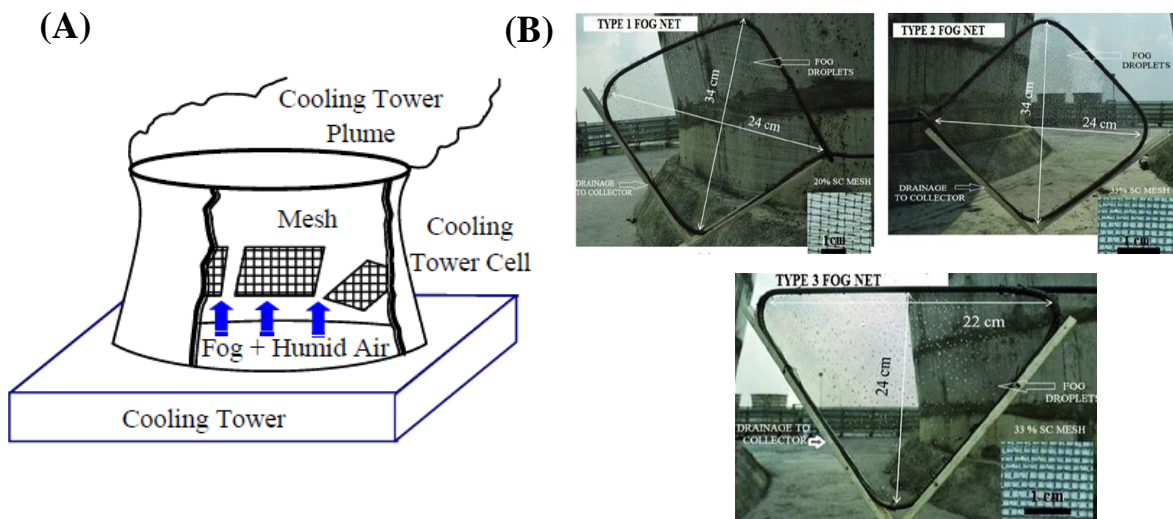


Figure 1.8: (A) Schematic of a cooling tower fog harvester. (B) Meshes of various SC (porosities), geometry placed at the plume of a thermal power plant cooling tower by Ghosh et al. [32] (Reproduced with permission from [32])

The study argued that, a metal mesh if placed near the plume of such a cooling tower, with the aim of arresting the drift losses (un-evaporated and re-condensed water droplets present in the

exhaust plume from industrial cooling towers), it could be expected to recover about 40% of this drift loss, depending on the mesh's porosity, view-factor and other parameters [48] (see **Figure 1.8-B**). Such revelations although make fog collecting meshes a prime candidate for implementation of in both natural and industrial fog harvesting scenarios.

1.2 Issues in capture and separation of dispersed phase: particulate filtration and fog capture:

1.2.1 Air-filtration

Air filters function by drawing surrounding unclean air through their fine openings in the filter medium. Particles – be it particulate matter or fog/smog remain as the dispersed phase within this continuous phase. As the dispersed phase pass through the filter medium, it gets collected in the filter medium by mechanisms like sieving, inertial impaction, interception, diffusion, or electrostatic attraction. Ideally, the air exits the filter with significantly reduced particle content. One strategy to achieve this is by increasing the packing density of the filter. While packed meshes may initially seem advantageous for maximizing airflow, a deeper examination reveals potential drawbacks. Their high packing density can result in heightened aerodynamic bypassing and diminished deposition, apart from inducing a large pressure drop across the filter. For an air filter to be efficient, it must strike a balance between maintaining high particle capture efficiency and ensuring acceptable airflow resistance. Thus, both filter penetration and aerodynamic resistance play pivotal roles in evaluating filter performance. The filter quality factor, denoted as Q_F is a measure of the filtration device's performance, where Q_F is defined as

$$Q_F = \frac{\ln\left(\frac{1}{1-\eta_a}\right)}{\Delta P} \quad (1.2)$$

where, η_a represents filtration efficiency, and ΔP is the pressure drop across the filter. The quality factor indicates the capture efficiency per unit pressure drop across a filter. One of the primary issues is filter clogging, where accumulated particles reduce the filter's permeability, reducing aerodynamic efficiency, η_a and that in-turn reduces quality factor. Also, a very dense filter warrants high deposition efficiency at the cost of high pressure-loss across the filter. For example, high-efficiency particulate air (HEPA) filters are recognized for their ability to capture 99.97% of particles sized 0.3 μm or larger. However, they exhibit a significant pressure drop across the filter element, limiting their suitability for use in environments requiring exceptionally high filtration quality, such as cleanrooms and healthcare facilities. An effective filter, characterized by a high filter quality, should ideally demonstrate both high collection efficiency and minimal air resistance without clogging the filter pores. This is because clogged pores are as reflected as pressure drop across the filter [48]. Achieving this balance often involves considerations such as flow velocity, pressure ratio at the inlet and outlet of the filter, fiber packing density (α), and the involvement of other field forces like electrostatic forces etc., all of which can influence collection efficiency.

Lowering the packing density inherently results in a minimal pressure drop across the filter, albeit with decreased particle deposition. However, enhancing particle deposition on a sparse filter can be achieved through the application of space charge injection in the filter assembly. Consequently, electrostatic filtration has emerged as a leading-edge technology in the air purification sector, harnessing electrostatic forces to efficiently capture particulate matter, including fog and aerosols.

Sanchez et al. [49] investigated particulate matter filtration using a single cylindrical rod made of copper, where aerosol separation occurred within the charged cylindrical precipitator based on an electrostatic field, as shown here in **Figure 1.9-A**. The percentage of particle penetration through the filter, consisting solely of the cylinder, varies with the electrical mobility diameter (d_m) for different applied voltages to the copper cylinder (**Figure 1.9-B**). Higher voltages lead to enhanced capture efficiency, even for larger particle sizes. This underscores the scenario where a stronger electric field yields greater particle capture efficiency, albeit with the potential risk of ionizing the air.

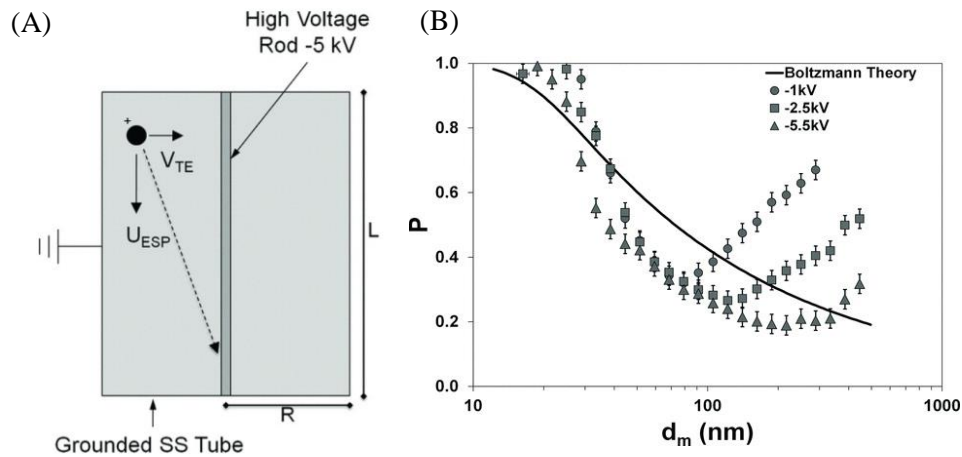


Figure 1.9: (A) Electrostatic field-based aerosol separation occurring on a charged cylindrical precipitator. (B) The percentage of particle penetration through the filter (with only the cylinder) varies with the electrical mobility diameter (d_m) for different applied voltages to the copper cylinder. Higher voltages result in improved capture efficiency, even for larger particle sizes. (Reproduced with permission from [49])

The application of electric fields around the meshes aids fog collection as the DEP force on the fog droplets steer the droplets towards the electrodes, overcoming the aerodynamic drag on the droplets. According to the study by Damak et al. [50], the primary limitation of low fog collection likely stems from aerodynamic bypassing leading to low fog deposition rather than low shedding rates, a challenge that could be addressed by employing strong electric fields around the mesh. In **Figure 1.10 - A – D**, trajectories of fog particles compared under

conditions with and without corona discharge are displayed. Most proposed collectors consist of meshes relying on inertial deposition for droplet capture and are inherently restricted by the aerodynamics of the flow.

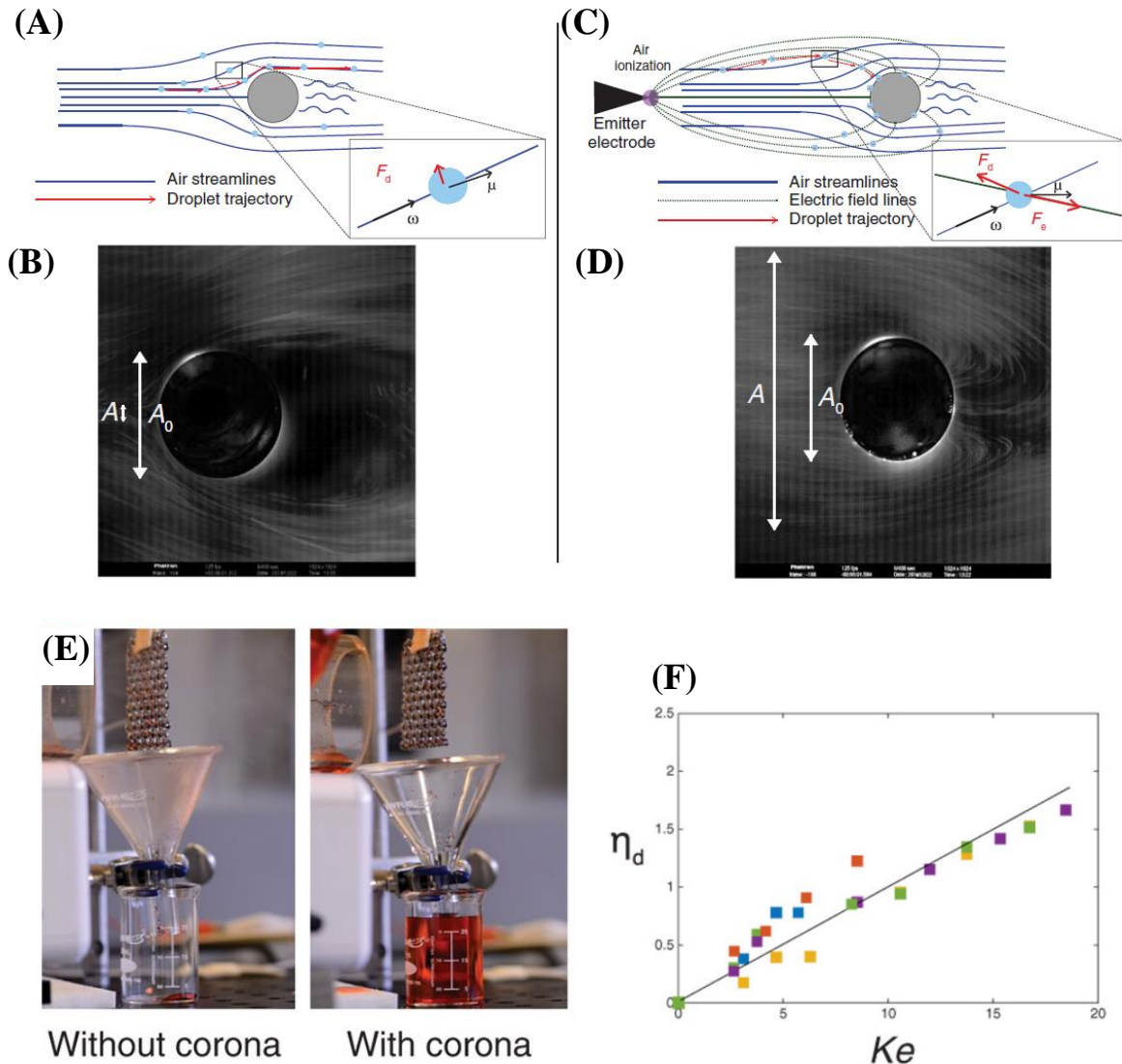


Figure 1.10: The trajectories of fog droplets around a cylinder (A) with and (B) without the application of an electric field. The mesh fiber, represented as a grey circle, is grounded, while the air stream is charged using a metal needle (emitter electrode). The schematic illustrates air streamlines and droplet trajectories, with photographs showing droplet trajectories in the (C) absence and (D) presence of an electric field. In (D), droplets are observed closely following the electric field lines. The inset in (B) illustrates the additional electric force acting on a droplet. Both cylinders in (B) and (D) have a diameter of 1.88 mm. Photographs in (E) display the collection mesh and the storage beaker for collected water after 30 minutes of exposure. With high voltage, 30 ml of water was collected, while only three droplets were collected without an electric field. (F) The deposition efficiency of five meshes as a function of Ke , (the ratio of electric force to viscous force). (reproduced with permission from reference [50])

The study proposes an alternative approach introducing electrical forces to overcome aerodynamic drag. By utilizing an ion emitter, they introduce a space charge into the fog,

imparting a net charge to incoming fog droplets and directing them toward a collector using an imposed electric field. This method increases fog water collection onto these fibers. This study later progresses into fog water collection on metal meshes of different geometric specifications, using the same technology (see **Figure 1.10 E – F**).

This observation was also noted in one of the earliest fog capture endeavours, which shares similarities with PM capture due to comparable diameters of the PM particles and fog droplets, as well as the use of electrified metal meshes. Uchiyama et al., in their study titled “Field experiments of an electrostatic fog-liquefier,” (shown here in **Figure 1.11-A – B**) [51, 52] demonstrated that fog collection efficiency correlates with the applied voltage and the diameter (D) of the mesh fibers. Furthermore, the capture efficiency exhibits a correlation with air velocity (**Figure 1.11-C**) and mesh opening pitch (**Figure 1.11-D**) in both scenarios, increasing with velocity until reaching a peak, after which it declines abruptly.

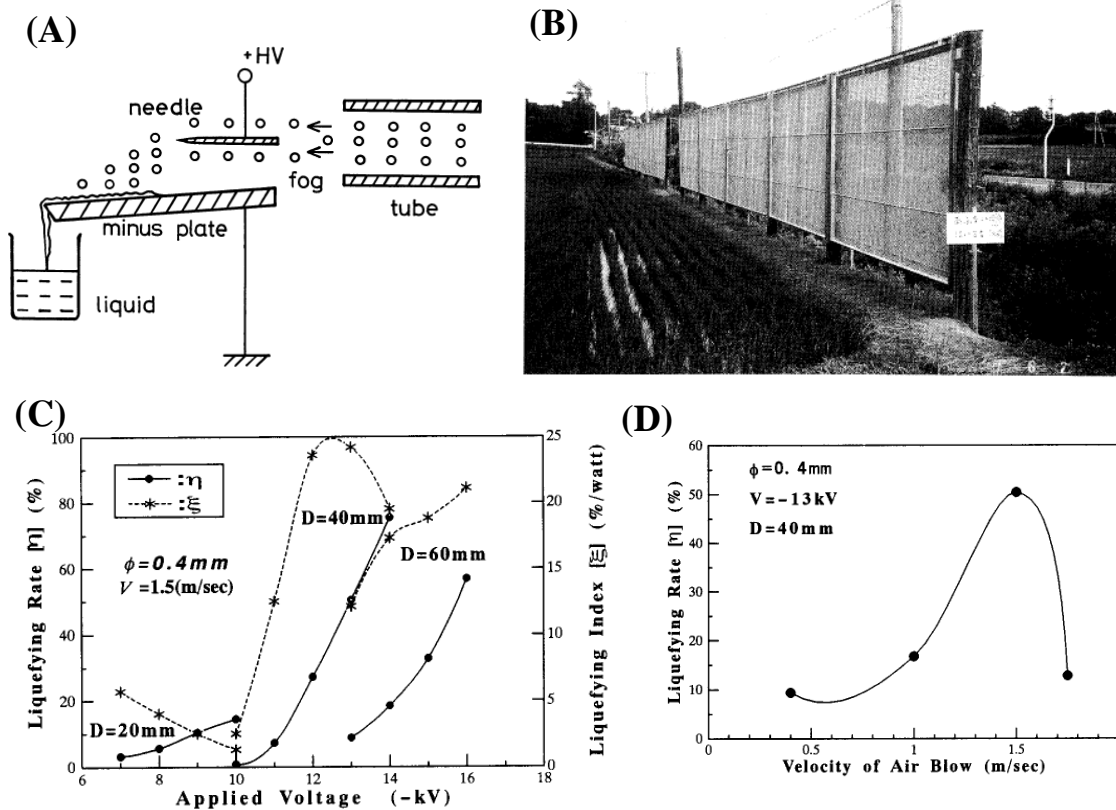


Figure 1.11: (A) The principle of the fog-liquefier, and (B) the physical installation of the mesh in a paddy field in Japan. (C) The relationship between the liquefying rate or collection efficiency (η_{dr}) and the liquefying index ($\xi = \eta_{dr} / \text{electric power consumption}$) [%/Watt] as a function of applied voltage. The parameter D represents the inter-electrode separation between the corona wire and the mesh. (D) The dependence of fog liquefying rate on air velocity. (reproduced with permission from references [51] and [52])

This underscores the role of aerodynamic efficiency and its dependence on these factors. While the above studies acknowledge improved capture efficiency with the inclusion of an electric field in the mesh/filter assembly, it is essential to consider the ecological ramifications of employing high voltages and the occurrence of corona discharge. One innovative approach to improving air filtration especially suited for personal use (e.g. mask) is the use of triboelectric adsorption techniques [15, 53], which entails the creation of a change on the filter element by friction between the filter layers. This method leverages electrostatic forces to enhance particle capture, significantly boosting initial filtration efficiency. However, the effectiveness of triboelectric adsorption tends to diminish over time, particularly in humid conditions created by exhaled breath [54, 55]. This decline in performance underscores the need for further enhancements in filter design to sustain protection levels. Additionally, filters experiencing gradual deposition of PM or fog particulates are susceptible to clogging, leading to decreased collection and, consequently, reduced collection efficiency.

1.2.2 Fog capture

A standard fog collector consists of meshes oriented perpendicular to the direction of fog flow. A fraction of the fog droplet population strikes the mesh fibers, gets deposited, coalesce to form larger droplets, which then roll down to get collected. A mesh pore clogs due to progressive deposition of these fog-droplets and subsequent coalescence of the deposited liquid leading to the formation of bigger droplets of different shapes on the fibers (**Figures 1.12-A**). These growing droplets may eventually touch the neighbouring mesh fibers when they clog the mesh pore either partly or completely (see **Figure 1. 12-A**). A clogged mesh pore offers a greater aerodynamic resistance to the oncoming fog stream, which in turn diminishes the fog droplet deposition. The droplet shape on a fiber depends on its volume, the wettability of the mesh fiber and the fiber diameter [56, 57]. The wetting characteristics of the mesh wire surface and its geometric parameters govern two critical constraints: the re-entrainment (**Figures 1.12-B**) of collected droplets from the wire and the clogging of mesh pores (**Figures 1.12-C**). Low adhesion between the collected droplets and the mesh fibers may lead to re-entrainment of the droplets back into the fluid stream (droplets being dragged away by the oncoming air), while high adhesion could result in droplets merging with neighboring ones, forming a liquid film and potentially clogging the mesh.

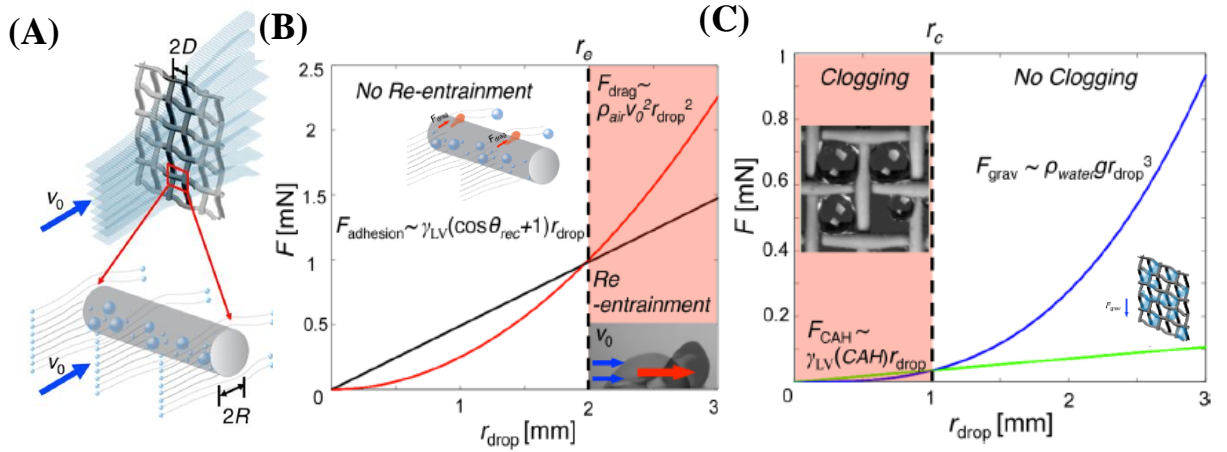


Figure 1.12: (A) Schematic showing fog flow and their deflection when passing through a woven mesh surface and a contour plot of the fog-harvesting efficiency. The enlarged portion marked in red, focuses on the interaction between the incoming fog droplets and a horizontal member of the woven mesh element. Fog droplets at the vicinity of the fiber are trapped and collected, while those at the periphery follow the streamline around the wire and escape. Droplets on the wire coalesce, and once they grow past a threshold size, they drain under gravity. Two adverse factors affecting collection efficiency are re-entrainment of collected fluid and clogging of mesh pore. A threshold for maximum and minimum droplet sizes to avoid (B) re-entrainment and (C) clogging respectively is depicted as contour plots, marking regions of stability of the drop on mesh as a function of drop radius. (reproduced with permission from reference [58])

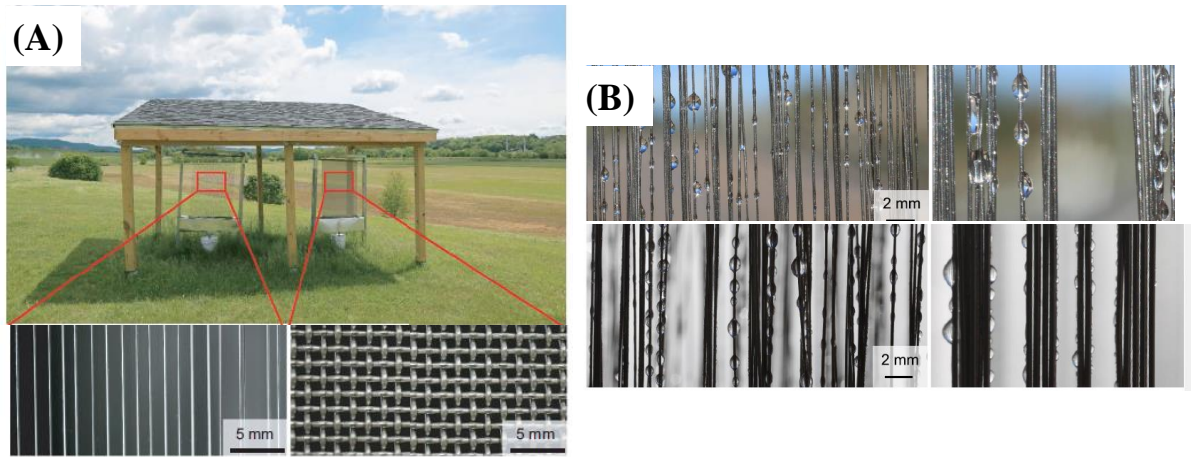


Figure 1.13: (A) Photograph of the fog harvesting installation made by [79, 80] at a farm in USA. (B) Photographs showing the issue of tangling for harps of various wire diameters and pitches, under heavy fogging [82]. (reproduced with permission)

Optimizing parameters like surface wettability, mesh wire radii, and wire spacing is crucial for enhancing fog collection efficiency, as they directly influence droplets-fibers interactions. Park

et al. [58] identified the stability regime of a drop on a mesh fiber based on the various forces acting on the drop. **Figures 1.12-B and C** demonstrate that to minimize re-entrainment, the force of adhesion must exceed drag forces, while to prevent mesh pore clogging, gravity forces should outweigh hysteretic pinning forces on the drop.

Therefore, droplet morphology, its solid-liquid footprint on the mesh fiber and relative size with respect to mesh dimensions, and fiber wettability play significant roles [59] in determining the fog-harvesting performance of a mesh.

Understanding droplet morphology on mesh fiber geometry based on surface wettability [60] and fiber diameter is fundamental to the design of the fog harvester mesh. It is hence favourable that a drop detaches early; but early detachment can also result in droplet loss by re-entrainment back into the fog stream, thereby reducing harvester efficiency. Drop-on-fiber morphology, its dimensions and its shedding under the influence of gravity, events which are often observed both in nature and in different engineering applications, like such fog harvesting mesh, can help design of better separation technology. In traditional meshes, a drop will often grow large enough to clog the mesh. A clogged mesh pore offers a greater aerodynamic resistance to the oncoming fog stream, which in turn diminishes the fog droplet deposition. The droplet shape on a fiber depends on its volume, the wettability of the mesh fiber and the fiber diameter [56, 57]. Therefore, the morphology of the droplet and its relative size with respect to the mesh dimensions, and the fiber wettability play important roles [59] in ascertaining the fog-harvesting performance of a mesh. Studying the droplet shape-on-fiber of specified dimension and surface wettability accurately for a given volume of liquid would allow for the design of ‘clog-proof’ meshes.

Wettability-engineering has been extensively leveraged by several researchers to enhance fog harvesting on sturdy impervious flat surfaces by advocating the use of three-dimensional features like cascading patterns [61], bumps [62] or bio-inspired surface modifications [63, 64, 65, 66] and micro-/nano-scale surface embellishments [67] for enhancing water capture. However, these impervious plates suffer from significant aerodynamic bypassing –[68] – leading to minimal fog deposition. Biomimetic surfaces, replicating the Namib desert beetle *onymacris unguicularis* [69, 70], cactus thorn-like geometries [71], or variations in surface wettability [72, 73] have shown attractive droplet drainage features for laboratory-scale setups, but they lack scalability of mass production for industrial or community fog harvesting applications [74, 75]. Considering these factors, mass-producible interwoven metal meshes may be best suited for fog-harvesting applications, and are scalable and structurally sound. It

is important to note here that the horizontal fibers of such a woven mesh can offer resistance to droplet drainage [76], and therefore lead to serious clogging issues [58, 77].

Vertical elements within these meshes play a pivotal role in facilitating the drainage of accumulated fog droplets [78], thus posing no threat related to clogging. In this context, Shi et al. [79, 80] and Goswami et al. [81] have underscored the effectiveness of harp-like mesh – the mesh has only an array of vertical elements (see **Figure 1.13-A**) – particularly in moderate fog conditions. However, the harp-design is found to be less viable in scenarios involving heavy fogging or in tilted arrangements (as one requires in cooling tower fog harvesters [32]) due to their structural weaknesses and susceptibility to tangling [82] (see **Figure 1.13-B**).

1.3 Gap area:

The highlights of the above discussions points to the necessity of reevaluating the design of meshes and filters, aiming to achieve high deposition efficiency without sacrificing aerodynamic performance or increasing the pressure drop across the filter.

Typical gap areas in the context of air filtration are:

- i) Research drive towards the development of filters for dispersed PM offering a better capture under lower pressure is never-ending endeavor. Prevalent literature extensively discusses various design modifications and the resulting enhancements in particulate capture in filters. Most of these designs employ dense meshes, exhibiting high deposition efficiency but increased pressure drop across. Conversely, rarer filters mitigate the problem of pressure drop across the filter, but at the expense of poor filtration efficiency. Therefore, there is a need for design, characterization, and optimization of filters that may offer good capture of suspended particulates, yet maintaining low pressure-drop across the filter.
- ii) Electrostatic separation, which leverages an imposed electric field and arrangement for space charge injection into the flow stream, have been explored to increase deposition efficiency, but this method suffers from potential hazards like corona discharge and ozone production.
- iii) The approach of inducing triboelectric charges on the mesh fibers to enhance deposition efficiency faces concerns over the limited durability of the filters that may often last a few hours; and therefore be typically used in face masks, but not in a broader context of industrial filtration.
- iv) Tunability of dielectrophoretic filtration to varying operational conditions, e.g., dispersed phase loading, particle size and flow velocity, is often restricted (e.g., voltage modulation in electrostatic filtration, which is limited by breakdown voltage limit). Although this technique has been investigated for separating dispersed phases in microfluidic devices, its application to open channel flow introduces a novel approach. Despite considerable advancements in the field of filtration science, achieving efficient separation of dispersed phases that vary greatly in size, while also minimizing pressure loss, continues to present a significant challenge.

In the realm of fog harvesting, certain facets of the aforementioned areas have remained less explored. For example,

- i) The issue of mesh pore clogging, particularly evident in fog collection worsens with continued use, as particulate matter and fog deposit, blocking the pores. Research links this to the surface tension between the PM/fog and the mesh fibers, strongly influenced by the fibers' wettability. Highly wettable meshes are prone to rapid clogging, significantly increasing pressure drop, while meshes with low wettability tend to have lower clogging rates but suffer from re-entrainment of particles into the airstream, reducing overall effectiveness; necessitating a need for optimization of mesh design.
- ii) Wettability-engineering to enhance fog harvesting has been advocated by several researchers. Use of three-dimensional features like bio-inspired cascading patterns, with micro-/nano-scale surface embellishments, on flat surfaces for enhancing water capture. However, these impervious plates suffer from significant aerodynamic bypassing leading to minimal fog deposition.
- iii) Certain bio-mimicking wettability patterns on surfaces prove to be highly effective in certain laboratory setups, but they lack scalability of mass production for industrial or community fog harvesting applications. Hence, prudent use of wettability engineering on mesh surfaces is needed so that the technology has an easier deployability.

Given these challenges, there is a clear need to redesign mesh pores, considering the interaction between mesh properties and particulates to develop meshes that are both effective and resistant to clogging.

Therefore, it is essential to bridge research gaps in two key attributes pertaining to dispersed phase separation:

- A.** developing a sparser mesh that achieves high particulate deposition efficiency yet having a tunability feature, so that they can adapt to operational variability in the dispersed phase flow, and
- B.** develop mesh-based dispersed phase (fog) separation system that is resilient to mesh pore clogging.

1.4 Objective:

This work addresses the challenge of efficiently capturing micron-sized particles, such as particulate matter and fog droplets, using mesh filters while overcoming two major obstacles: clogging of mesh pores and the associated high-pressure drop in clogged filters. While finer meshes demonstrate excellent filtration capabilities, they are prone to pore clogging, whereas sparse meshes with larger pores resist clogging but generally offer lower filtration efficiency. To bridge this gap, this study focuses on two key strategies: developing clog-resistant meshes through optimized design and surface treatments, and leveraging dielectrophoretic (DEP) forces to enhance droplet capture in sparse meshes.

By utilizing DEP forces, which act on polarizable but uncharged particles in a non-uniform electric field, this study explores a novel filtration approach where electrodes function as both the electric field source and the particle deposition surface. Unlike electrophoresis, DEP does not require space charge injection, thus mitigating associated safety risks. Furthermore, for applications like fog harvesting, where mesh clogging is a critical issue, incorporating optimal mesh design—accounting for fiber geometry and wettability—presents a promising solution for achieving high collection efficiency. This dual approach offers a significant step forward in developing efficient, clog-resistant filtration systems. The present study involves experimental investigations, numerical simulations, and analytical modelling to characterize transport and capture of dispersed phase in the context of air filtration and fog harvesting with the common aim of improving their performance.

Objectives of the present work may be summarized under two salient headings:

- A.** Characterization of dielectrophoretic separation of dispersed phase using three-phase ac voltage and evaluation of its performance in the context of an air-filtration system.
- B.** Design of a fog harvesting mesh that is resilient to clogging and characterization of its efficiency of collection of the dispersed phase.

A. Characterization of dielectrophoretic separation

One method to enhance the deposition efficiency of meshes is to use a near field force, such as dielectrophoresis, to alter particle trajectories away from the streamlines towards the fibers. This technique does not require space charge injection, which poses potential hazards. In dielectrophoresis, a force is exerted on dielectric particles that are polarizable but not necessarily charged, as they move through a non-uniform electric field. Despite considerable

advancements in the field of filtration science, achieving efficient separation of dispersed phases that vary greatly in size, while also minimizing pressure loss, continues to present a significant challenge. The DEP filter in this work is assumed as an array of cylindrical metallic fibers, doubling as both filtration elements and electrodes. The fibers are energized by an ac three-phase voltage. The transport model reckons the effects of particle inertia, viscous drag, DEP forces, and Brownian motion on particle trajectories, while the particle capture efficiencies are investigated through Lagrangian tracking of the particles. A numerical scheme that uses first-order time marching is used to track the trajectories of randomly dispersed particles as they pass over the charged electrode array. Specific objectives of this work are

- to evaluate the potential of dielectrophoresis (DEP) to segregate and collect dispersed water droplets from an air stream in a two-phase flow, using numerical simulations.
- to evaluate the statistical analysis of the simulation data to explore how variables such as electric voltage, frequency modulation, droplet sizes, fiber diameters, inter-fiber spacing, and air velocity impact filtering performance.
- to tune mesh and electrical attributes in determination of an operating regime for optimal filtration.
- to evaluate the pressure drop across the DEP filter designed and compare it against other well know technologies in filtration.

B. Design of a clog-proof mesh and its performance characterization

Fog water collection, from natural and industrial sources, has in recent years been considered as a feasible source of freshwater; which involves placing of metal or polyester meshes in the path of fog flow. Fog droplets impinge and deposit on mesh fibers, coalescing with previously deposited fog droplets to evolve as larger drops that eventually detach due to their weight. This phenomenon is largely influenced by mesh fiber wettability, diameter and its arrangement relative to the fog flow. Literature highlights the major problems in fog harvesting mesh to be its low fog collection efficiency primarily attributed to clogging of mesh pore, re-entrainment of already collected droplet and poor drainage. The present study tries to address the problem of clogging of mesh pores by some simple and frugal means. Specific objectives are

- to redesign traditional interwoven metal mesh structures involving optimization crucial mesh parameters, including mesh pitch, fiber diameter, and fiber wettability. These parameters need to be adjusted based on the numerically and experimentally observed

morphology of fog-water droplets under various operational conditions, namely mesh fiber diameter and its wettability.

- to modulate mesh wettability, ranging from superhydrophilic to hydrophobic fibers, to be undertaken in determination of the optimal shade coefficients that may facilitate the development of fog harvesting meshes resistant to clogging.
- to determine optimal shade coefficients to create clog-resistant meshes drawing from mesh wettability and droplet morphology.
- to estimate aerodynamic, deposition, and overall collection efficiencies for the optimized meshes.

The rationale and objectives of the present work are pictorially described below in **Figure 1.14**

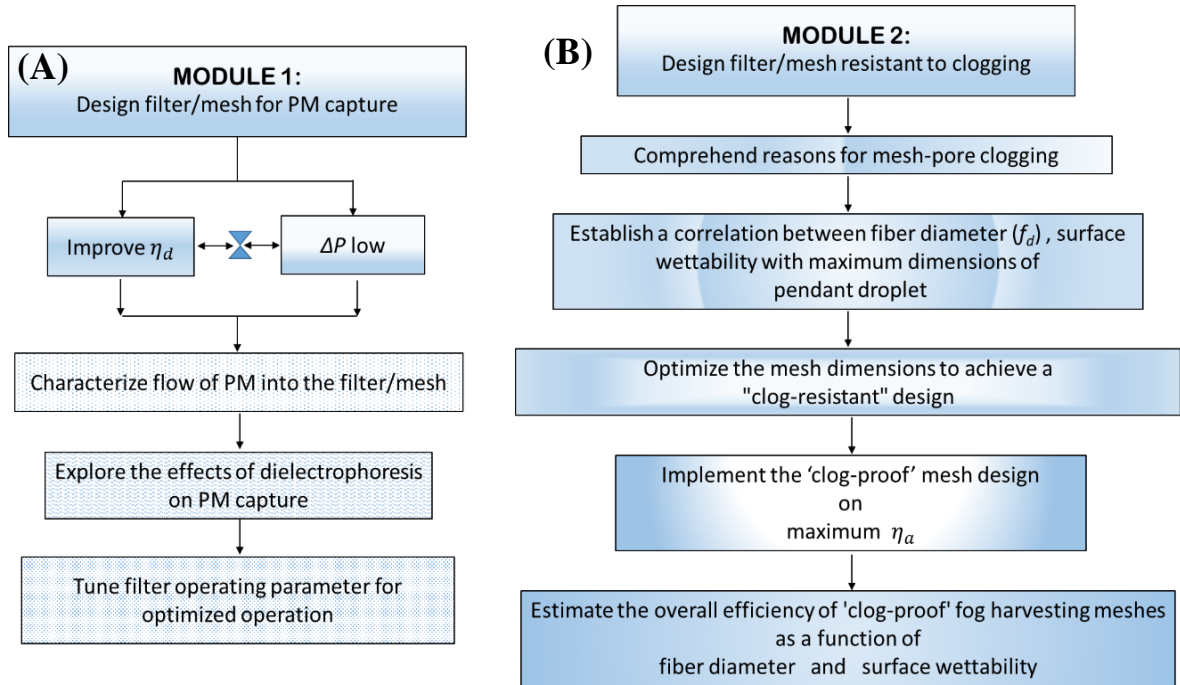


Figure 1.14: Rationale of the study: **(A)** Module 1 explores the possibility of enhancement in deposition efficiency of particulate matter (PM) on meshes leveraging DEP force produced by a 3-phase AC voltage. **(B)** Module 2 characterizes the shape and dimensions of deposited fogwater on the mesh fibers and deduces, for a given fiber diameter and the mesh fiber wettability, the mesh pitch to render the mesh “clog-proof”. Conditions suitable for enhancing the aerodynamic efficiency of fog collection are also identified for the clog-poof mesh.

Chapter 2
**Tunable dielectrophoretic (DEP) filters for air-
borne microdroplet capture**

2 A dielectrophoretic mesh filter for the capture of airborne liquid droplets

The need for effective filtration technologies has existed for a long time in different engineering applications, while more recently it has grown exponentially because of epidemic disease outbreaks like SARS, MERS and COVID-19. While the technology of air filtration is mature, and abundant literature exists on the fundamental aspects of filtration, large pressure drop and sensitivity to operating parameters have remained a challenge [83]; 84]. The need for personal air purification – household air purifiers or even face masks [85], which deals with dispersed droplets of largely divergent sizes, are some examples – have instilled a greater need for tunability, which allows facile modification of the design or operating conditions of the filtration system to achieve high capture and, at the same time, low pressure drop. The present work leverages dielectrophoretic air-purification systems to address some of the limitations seen in conventional filtration methods.

Traditional air filters like High Efficiency Particulate Air (HEPA) filters have played pivotal role in maintaining air quality and addressing waste gas treatment. These filters explore sieving, inertial impaction, interception, diffusion and electrostatic attraction [86];13; 87]. To enhance the removal of suspended droplets and particulates via mechanical means, they commonly incorporate fine fibrous materials characterized by diminutive fiber diameters and inter-fiber distances spanning from 0.1 to 10 μm , often accompanied by low porosity within the range of 0.5 to 10% [14; 88]. Nevertheless, this approach often entails a trade-off, manifested as increased pressure losses across the filters. This in turn can potentially compromise the overall energy footprint of these filtration systems, or the comfort of the users in case of face-mask application. Another crucial drawback in the traditional filtration system is their selectivity to the specific particle/droplet size – while fine filters get easily clogged by the larger droplets [89], coarser filters exhibit poor filtration against the smaller ones. This poses serious challenge when the oncoming dispersed phase had a large polydispersity index, for example, in air-filtration system high performance is often sought in the ranges of $\text{PM}_{1-2.5}$ and $\text{PM}_{2.5-10}$, [90]; [17; 18], considering their respective compositions and impact on overall air quality [91].

To overcome the limitations of conventional filters, dielectrophoretic air-purification may emerge as a promising alternative. The present study, as depicted in **Figure 2.1**, proposes dielectrophoretic (DEP) force, which arises due to the polarization of droplets in a spatially varying electric field, to capture droplets or droplets from a carrier stream efficiently. DEP filtration is effected by inducing motion in dispersed, polarizable droplets or droplets by applying a spatially non-uniform, unsteady electric field, thus capturing them on the electrodes from the dispersing flow.

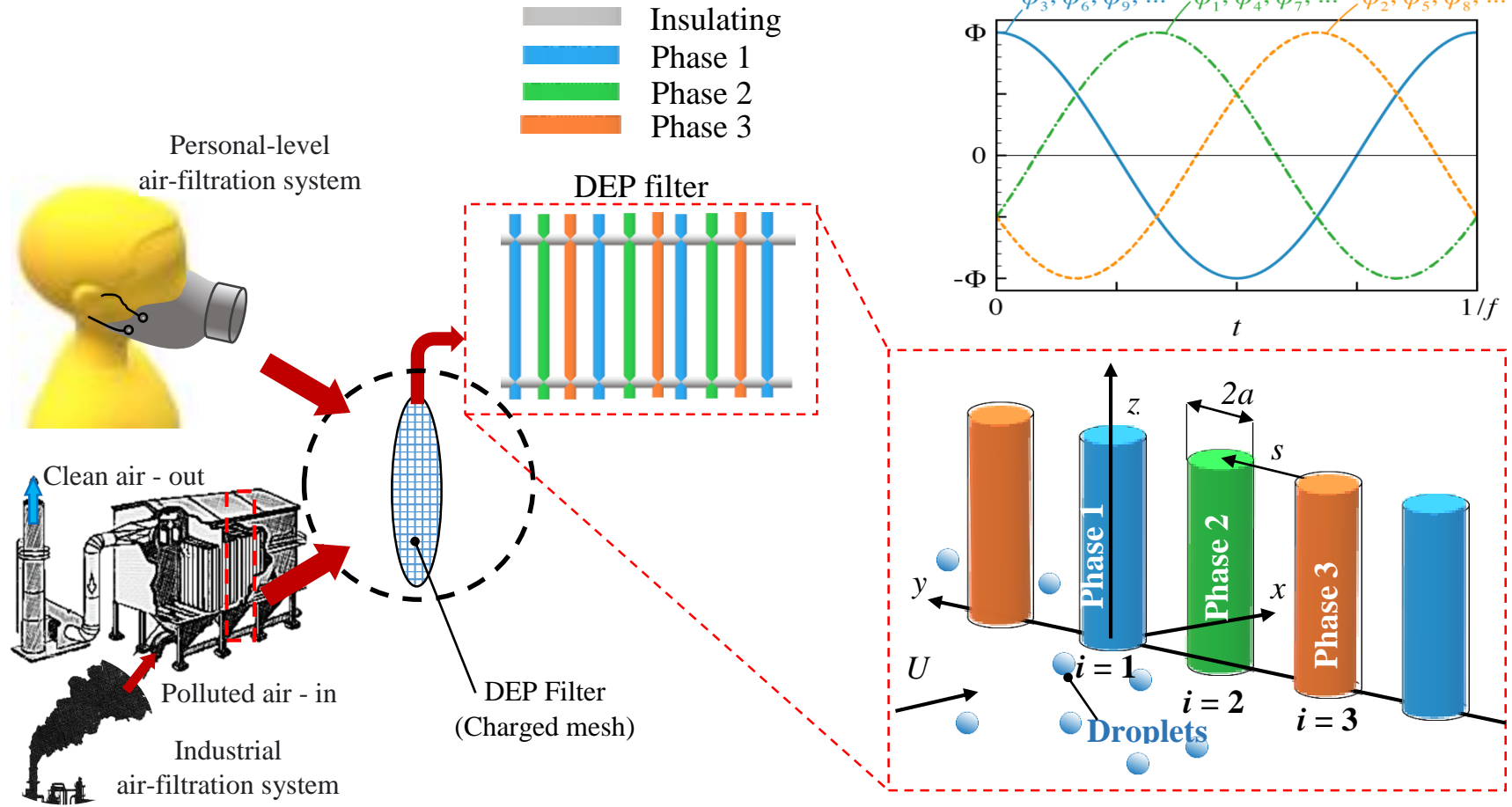


Figure 2.1: Representative schematic of the proposed DEP based air filtration system for personal-level (top) or industrial (bottom) air-filtration system. Droplets (5 – 50 μm diameter) are arrested on the charged mesh that has a 3-phase traveling voltage imposed on its electrically conducting parallel fibers [92]; 93] that also act as electrodes. The cross fibers (grey) are insulating in nature and maintains the safe inter-electrode distance to avoid voltage breakdown. **INSET** Geometric arrangement of electrodes in the charged mesh of the active filter. The droplets are shown to be moving with free stream velocity U towards the electrodes. The insulating members of the filter are not shown in the inset.

In contrast to traditional electrophoretic (EP) filters [50; 51] DEP filtration would be advantageous as no ionization of droplets or droplets is required. Potential hazards associated with ionizing the medium is thus mitigated. DEP force has proven highly effective in manipulating trajectories of a wide range of micro-droplets [94]; 95], including cells, viruses, proteins, and colloids [96]; 97] in membranes [98] and micro-channels [99] in liquids. However, its application for air filtration systems is a novel concept.

Herein we investigate the efficacy of dielectrophoresis for the separation and collection of a dispersed phase from a flowing stream of continuous phase through a numerical simulation. The dispersed phase consists of water droplets of varying diameters transported in an air stream. The DEP filter is made of an array of cylindrical fibers. The core functionality lies in the application of an alternating current (AC) voltage to the fibers, generating a traveling electric wave field. Droplets approaching the electric mesh acquire dipolar moments due to the electric fields and are subsequently attracted in the direction of the instantaneous field gradient. Eventually, the droplets are intercepted by the electrodes and deposited on them. The analysis takes into account drag, Brownian motion, and DEP forces [100]. An extensive study has been conducted to characterize the dependence of particle capture efficiency on parameters such as the flow velocity (U), droplet size (d_p), mesh configurations (s/a , the ratio of fiber spacing to fiber radius), electric field strength (E) and the frequency (f) of the applied 3-phase supply. We restrict our investigation to water droplets of diameters ranging from 5 to 50 μm , which encompasses the droplet size of saliva ejected during speaking and sneezing [101]. This size range also covers the particulate matter size found typically in urban [102] and industrial environments [103]. The free-stream velocity U is varied from 0.5 m/s to 10 m/s, which can represent various scenarios, including mask applications (velocity ~ 50 cm/s during coughing or sneezing [104]) or industrial filtration systems and fog harvesters (5-10 m/s) [32]. On the contrary, for HEPA filters, the maximum velocity does not exceed 0.5 m/s [105]. Compared to conventional fibrous filters, the present dielectrophoretic filtration system offers several advantages. For example, the fibers in DEP filtration system may be spaced more widely apart, eliciting lower pressure drop and a high-quality factor. Also, as demonstrated in the study, the operating parameters of the DEP filter may be tuned for high filtration efficiency even in the face of varying working conditions. The present study shows that the DEP filtration can be conceptualized either as a face mask or an industrial-grade air-filtration system.

2.1 Theoretical modelling and simulation

Figure 2.2-A shows the schematic diagram of the crossflow of the droplet-laden air over the array of electrodes. The dispersed phase comprising of micron-scale water droplets of diameter d_p is advected by a homogeneous one-dimensional (in x -direction) flow of the continuous phase (air) [106]. The flow, which enters the computational domain with a velocity U , passes over the array of cylindrical electrode-fibers [107]; a 3-phase AC voltage is applied to the electrodes in a prescribed sequence.

Since the dispersed phase droplets have very low Capillary, Bond and Weber numbers ($Ca = \frac{\mu U}{\gamma} \approx 10^{-4}$; $Bo = \frac{\rho_p g d_p^2}{4\gamma} \approx 10^{-4}$ or less; $We = \frac{\rho U^2 d_p}{\gamma} \approx 10^{-3}$) where ρ_p and ρ denote the droplet and air densities, μ the dynamic viscosity of air, g the gravity, and γ the surface tension of the liquid, droplets are assumed as rigid spheres; hence we have used the terms ‘droplet’ and ‘particle’ interchangeably in the remainder of the manuscript. An Eulerian-Lagrangian model, capable of simulating airflow with suspended droplets is considered. In this model, we consider one-way coupling from airflow to droplets, implying that the fluid drag influences the particle trajectory, but the reaction of the same drag force is too small to influence the fluid flow. This is a rational assumption because the volume fraction of droplets is typically low – in the order of 10^{-6} to 10^{-5} [108]; [109]; [110] – for our intended applications.

The dispersed phase moves towards the cylindrical electrodes, along with the flow (**Figure 2.2-A**). Transport of the droplets influenced by various forces which is expressed as

$$m_p \frac{d\mathbf{u}_p}{dt} = \mathbf{F}_D + \mathbf{F}_{DEP} + \mathbf{F}_B, \quad (2.1)$$

where m_p represents the particle/droplet mass, \mathbf{u}_p its velocity and t the time. This droplet dynamic is modelled with Stokes drag force (\mathbf{F}_D), the DEP force (\mathbf{F}_{DEP}), and a random force (\mathbf{F}_B) that accounts for Brownian fluctuations. The effect of gravity is neglected for simplicity.

A 3-phase alternating electric field \mathbf{E} of frequency f is applied to the electrodes (**Figure 2.2-B**). It generates a time-varying electric field illustrated by equipotential lines (**Figure 2.2-C**). For spherical droplets of dielectric constant ϵ_r , suspended in air, the DEP force can be expressed as [111]

$$\mathbf{F}_{DEP} = \frac{\pi d_p^3}{4} \epsilon_0 \epsilon_r K_{CM} \nabla E^2, \quad (2.2)$$

where the permittivity of free space is denoted by ϵ_0 . The Clausius-Mossotti factor (K_{CM}), is computed from the dielectric constant of the dispersed phase as [112]

$$K_{CM} = \frac{\epsilon_r - 1}{\epsilon_r + 2} \quad (2.3)$$

For water droplets, $\varepsilon_r = 80$ and $K_{CM} \approx 0.96$. The gradient of squared field strength \mathbf{E}^2 , as produced by the fiber electrodes remains to be directed towards the axes of the cylindrical fibers, as described by equipotential lines in **Figure 2.2-C & D**.

As droplets are transported in the flow, they experience viscous drag force which is assumed to follow the modified Stokes drag law so that

$$\mathbf{F}_D = \frac{3\pi\mu d_p}{C}(\mathbf{u} - \mathbf{u}_p), \quad (2.4)$$

where \mathbf{u} denotes the local fluid (the continuum phase) velocity, and C the Cunningham correction factor.

The continuous phase – the carrier gas phase in this case – follows the conservation equations of mass and momentum as it experiences a steady, incompressible flow past the array of the cylindrical fibers. As already mentioned, we have assumed a dilute suspension of droplets, which aligns with the underlying assumption of one-way coupling between the dispersed and the continuum phases. Therefore, dielectrophoretic transport of the droplets is not expected to alter the flow field and the continuum phase may be assumed to have a “frozen” flow field. In this study, the viscous flow of air at low Reynolds numbers passing over an infinite row of identical circular cylinders is represented using Stokes equation of motion, as computed by Miyagi [113] (see **Figure 2.2-E**).

The Cunningham correction factor [114] in **Eq. (2.5)** is expressed as

$$C = 1 + \frac{l}{d_p} \left(2.34 + 1.05e^{\left(-0.39/\frac{l}{d_p}\right)} \right), \quad (2.5)$$

where l denotes the mean free path of droplets. The correction factor takes into consideration the deviations from the Stokes law in the small particle-size limit. For the present study, small Knudsen numbers $l/d_p \lesssim 0.01$ confirm that air behaves as a continuum medium.

The Brownian fluctuations, arising from the random thermal motion of droplets, thus introducing stochastic displacements of the droplets, is described as [115]

$$\mathbf{F}_B = m_p \sqrt{\frac{216\mu k_B T}{\pi C \rho^2 d_p^5 \Delta t}} \mathbf{G}, \quad (2.6)$$

where k_B denotes the Boltzmann Constant, T the absolute temperature, Δt the time step used in the numerical integration of the equation of motion and \mathbf{G} a stochastic variable vector obeying the normal distribution [116]. Incorporating these forces, the droplet-transport equation reduces to

$$m_p \frac{d\mathbf{u}_p}{dt} = \frac{3\pi\mu d_p}{C}(\mathbf{u} - \mathbf{u}_p) + \frac{\pi}{4} d_p^3 \varepsilon K_{CM} \nabla E^2 + m_p \sqrt{\frac{216\mu k_B T}{\pi C \rho^2 d_p^5 \Delta t}} \mathbf{G}. \quad (2.7)$$

Instantaneous positions of a dispersed droplet are obtained through time integration of its instantaneous velocity, so that

$$\mathbf{x}(t) = \int_0^t \mathbf{u}_p dt + \mathbf{x}(0) \quad (2.8)$$

Eq. (2.8) is solved for each particle entering the computational domain to compute the particle trajectories in conjunction with **Eq. (2.7)** for the particle velocity, employing a forward-differencing time marching scheme. To ensure accuracy, the time increment (step) is determined based on the time required for the particle to move a maximum distance of 5% of its diameter under the given condition.

The electric field created by the array of wire electrodes is determined under the assumptions that the field is electrostatic and that the wire diameter is small compared to the inter-wire distance ($s/a \geq 10$). Potentials ϕ_i applied to wire-electrodes i ($i = 1, 2, \dots, 6J$), electric charges σ_i are induced at wire surfaces. The wire charges are computed by solving the following coupled equations,

$$\begin{aligned} c_{i1}^{inv} \sigma_1 + c_{i2}^{inv} \sigma_2 + \dots + c_{iJ}^{inv} \sigma_J &= \Delta\phi_i, \text{ for } i = 1, 2, \dots, J-1, \\ \sigma_1 + \sigma_2 + \dots + \sigma_J &= 0 \end{aligned} \quad (2.9)$$

where $\Delta\phi_i$ is the inter-electrode voltage: $\Delta\phi_i = \phi_{i+1} - \phi_i$. The coefficients c_{ij}^{inv} are of the inverse capacitance matrix for electrodes of diameter a placed at y_1, y_2, \dots, y_J ,

$$c_{ij}^{inv} = \frac{1}{2\pi\epsilon_0} \ln \left| \frac{y_i + a - y_j}{y_{i+1} - a - y_j} \right|, \text{ with } y_i = a \left(i - 3J - \frac{1}{2} \right). \quad (2.10)$$

The electric field is then computed by

$$\mathbf{E} = -\nabla\psi, \quad \psi = -\sum_{i=1}^J \frac{\sigma_i}{2\pi\epsilon_0} \ln \left(\frac{r}{a} \right). \quad (2.11)$$

The convergence of the electric fields at the middle level $0 \leq y < 3a$ is achieved when $J \geq 10$ for simulating the fields created by an array of infinite number of electrodes.

The particle transport and deposition model is validated against experiments of Gregory [117] and simulation results of Mirzaee et al. [118], detailed in **Appendix A Section A1**.

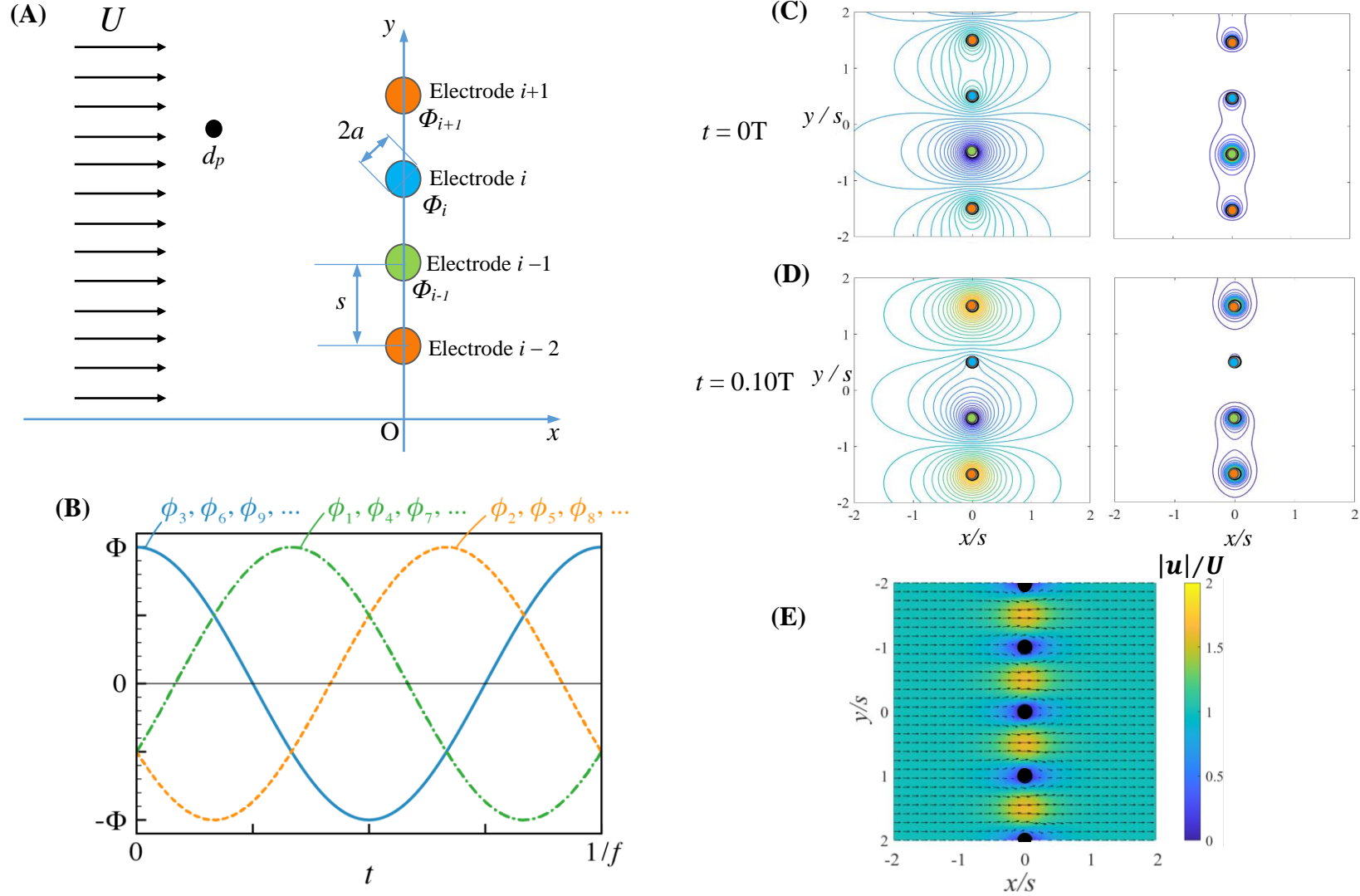


Figure 2.2: The geometric, flow and the electric field arrangements. (A) The configuration of the electrodes (red circles) having radius of a and spaced out at distance s apart. A droplet/particle (the black circle) of diameter d_p is advected towards the electrodes with a free-stream velocity of U . (B) Sequence of the 3-phase traveling voltage of magnitude Φ_0 and frequency f applied on the electrodes. (C) The electrostatic potential field Φ , and (D) the square of the electric field intensity (E^2) at different time instants (of the time period T) to describe the traveling nature of the fields. (See *ESI* video **S1** for further description of the travelling fields). (E) The normalized velocity field \mathbf{u}/U responsible for advecting the droplets.

Simulations are run for the dispersed phase droplets of varying size ($d_p = 5, 10, 25, 50 \mu\text{m}$) and inlet flow velocity of the continuous phase ($U = 0.5, 1, 2.5, 5, 10 \text{ m/s}$) to evaluate the DEP filter performance and optimize its design for different applications. The mesh electrodes are arranged with a defined spacing ($s = 500, 1000, 1500, 2000, \text{ and } 2500 \mu\text{m}$) and electrode/fiber radius ($a = 50, 100, 150, 200, 250 \mu\text{m}$) to maintain $s/a \geq 10$, ensuring low pressure drop (see Section 3.6 for explanation). Droplets are released from 20 equidistant initial positions along the y-axis, spanning from $y/s = -1$ to $+0.9$ with uniform spacing, and are tracked until they converge on the electrodes or exit the domain (i.e., $x/s \leq +2$). Both the x and the y axes are normalised with the inter-fiber spacing, s . Droplets are released with zero slip velocity along with the flow from the $x/s = -2$ plane ($x/s = 0$ denoting the electrode plane). A 3-phase supply of voltage magnitude Φ_0 is so applied to the electrodes that the nominal field intensity ($E_0 = \Phi_0/s$) remains at or below 2.8 kV/mm to prevent the dielectric breakdown of the surrounding medium. A baseline frequency of the 3-phase AC supply is assumed at 50 Hz , and it is varied up to 8 kHz to explore a range of operating conditions.

2.2 General description of particle trajectories

To describe the general transport behaviour of the droplets, we focus on a zone around two electrodes (located at $x/s = 0$ and $y/s = -0.5$ and $+0.5$; see the red circles in **Figure 2.3**) describing the trajectories of 20 representative droplets (released at uniform intervals, spanning from $y/s = -1$ to $+0.9$) for $U = 2.5 \text{ m/s}$. Two extreme cases of particle size, i.e., $d_p = 5.0 \mu\text{m}$ (**Figure 2.3-A**) and $50 \mu\text{m}$ (**Figure 2.3-B**) (see *ESI* video **S2**). A fiber radius of $a = 50 \mu\text{m}$ and an inter-electrode spacing of $s = 2500 \mu\text{m}$ have been considered. The 3-phase 50 Hz traveling voltage $\Phi_0 = 7 \text{ kV}$ applied to the electrode corresponds to $E_0 = 2.8 \text{ kV/mm}$. The motion of these droplets in the gas stream is governed by an interplay of hydrodynamic, electrodynamic and Brownian forces as mentioned in **Eq. (2.7)**. For smaller droplets, large Brownian fluctuations are observed (see **Figure 2.3-A**). Larger droplets are found to be less affected by Brownian force and align themselves better with the streamlines except for the vicinity of fibers (**Figure 2.3-B**). Distinct transverse deviations in the trajectories of the droplets are observed for both particle sizes due to the DEP force. This is more tangible near the electrodes, where the field gradients are strong. It is apparent from **Figures 2.3-A** and **2.3-B** that the interplay of the inertia, viscous, Brownian and DEP forces on the droplets are strongly influenced by particle size. For example, for large droplets, the trajectory is dictated more through the mutual interaction of inertia, drag and DEP forces. Conversely, smaller droplets experience relatively more pronounced Brownian force, which results in stochastic behaviour. A more detailed

account of the combined influence of these forces, especially concerning smaller versus larger droplets, is provided in **Figure A2** of *Appendix A*.

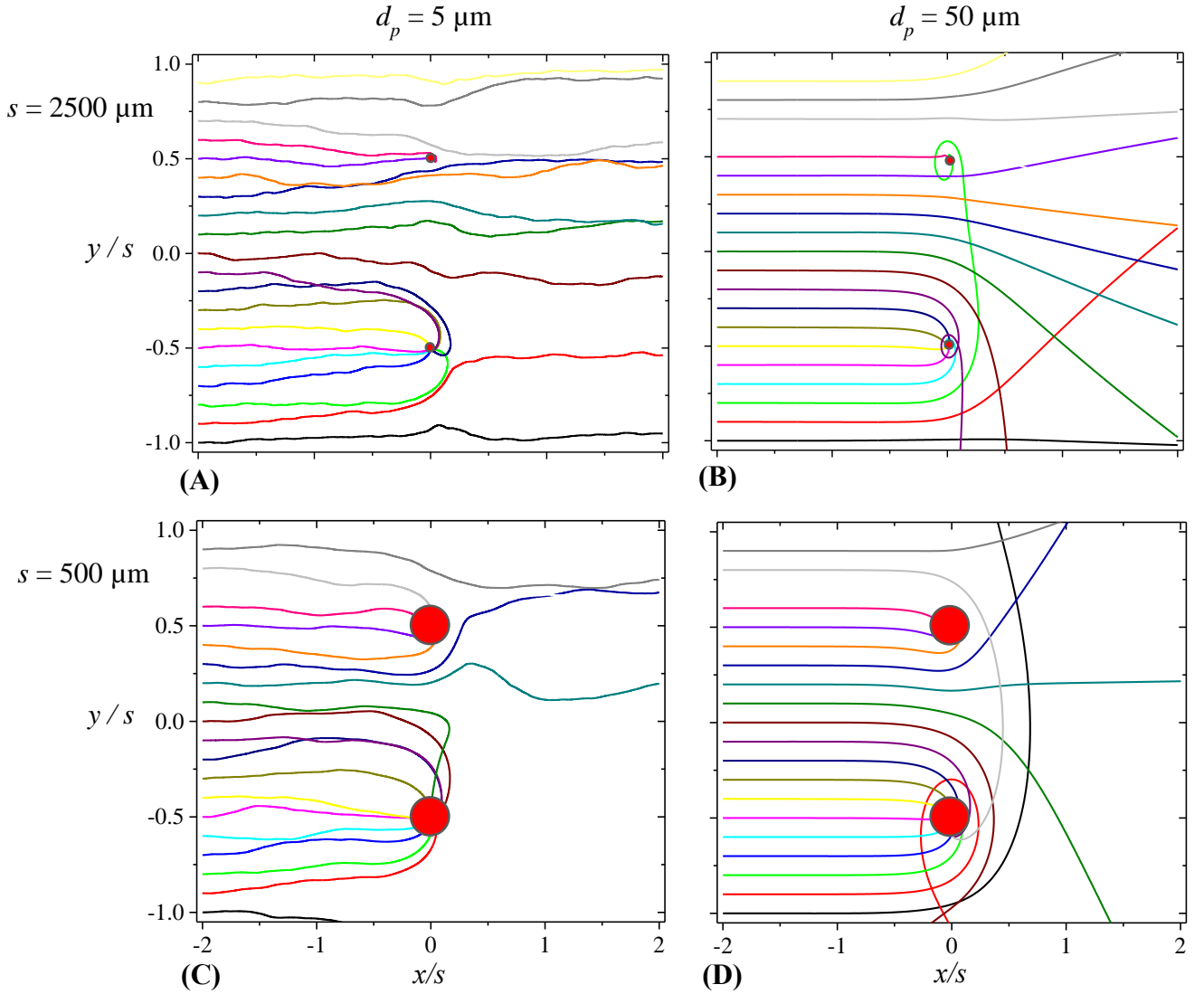


Figure 2.3: Particle trajectories for (A and C) $d_p = 5.0 \mu\text{m}$ and (B and D) $d_p = 50 \mu\text{m}$ during DEP capture with mesh of fiber radius $a = 50 \mu\text{m}$ and inter-electrode spacing (A and B) $s = 2500 \mu\text{m}$, and (C and D) $s = 500 \mu\text{m}$ operating at a 3-phase traveling-voltage, with a nominal field strength of $E_0 = 2.8\text{kV/mm}$ and frequency $f = 50 \text{ Hz}$. A free stream velocity $U = 2.5 \text{ m/s}$ is considered. Brownian fluctuation is more prominently observed for the smaller particle, i.e., for $d_p = 5.0 \mu\text{m}$. Both the axes are normalized by s . Fibers in C and D (i.e. for smaller s) appear to have larger diameter, since the length scale are normalized with the inter-fiber spacing s .

Despite the gross behavioural difference between the particle trajectories in **Figure 2.3-A** and **2.3-B**, both the cases exhibit nearly comparable outcomes in terms of particle capture. For example, 10 out of the 20 droplets with $d_p = 5.0 \mu\text{m}$ escape downstream, while the same configuration leads to the escape of 12 of the 20 droplets with $d_p = 50 \mu\text{m}$. **Figure 2.3-C** and **2.3-D** show the trajectories for the same two sets of droplets under the same conditions of a ,

U , E_0 , but the inter-electrode spacing is now reduced to $s = 500 \text{ } \mu\text{m}$. With decreased inter-electrode spacing, the extent of Brownian fluctuation is found to decrease, as particularly evident from a comparison of **Figures 2.3-A** and **2.3-C**. This indicates that the DEP force has a stronger influence with decreasing s . The particle capture is also found to be strongly enhanced in the case of smaller s as compared to the case of $s = 2500 \text{ } \mu\text{m}$. A reduced value of s creates a steeper gradient of electric field (i.e., $\nabla|E|$) in the inter-electrode space. Since the DEP force is proportional to E^2 (see the comparison of the time-averaged spatial distribution of E^2 for $s = 500$ and $2500 \text{ } \mu\text{m}$ in **Figure A3-A** and **B** respectively, in the *Appendix A*), it is stronger for $s = 500 \text{ } \mu\text{m}$ configuration, thus effecting a better particle capture. Additionally, particle capture with smaller s is facilitated due to the geometric factor – the fractional projected area of the electrodes in the dispersed phase flow is larger for $s = 500 \text{ } \mu\text{m}$, which leads to a greater degree of particle interception. For example, in **Figure 2.3-C** and **2.3-D**, only 4 and 6 droplets, respectively, are observed to escape downstream with the flow. To better demonstrate the stochastic behaviour of the droplets, refer to **Figure A2-A** and **B** in *Appendix A*, showcasing the trajectories (pathlines) of 10 droplets each of droplet size $5.0 \text{ } \mu\text{m}$ and $50 \text{ } \mu\text{m}$ respectively, released consecutively on to an incoming air stream, from an initial y/s , with a free steam velocity of 2.5 m/s . A mesh array with $a = 50 \text{ } \mu\text{m}$ and $s = 2500 \text{ } \mu\text{m}$ is considered. Despite being released from the same initial position, the droplets exhibit varied paths in ten consecutive runs due to the influence of Brownian motion.

2.3 Role of DEP in particle capture

In order to establish the role of DEP in the separation, we run the simulations without and with electric field for different electrode spacing, flow velocities and particle sizes. As the Brownian force induces a stochasticity in the particle dynamics, we strive to ensure the statistical significance of the data. For this, each simulation is run multiple times and we quantify the occurrence of capture (Π), normalized by the attempted runs.

$$\Pi = \frac{\text{Number of events of particle capture on any of the electrodes}}{\text{Number of runs with particle released from a particular position } y} \quad (2.12)$$

The denominator in **Eq. (2.12)** is 5 for our numerical experiments. The occurrence Π of particle capture will be a function of the transverse position of particle-release relative to that of the electrodes, unless the transverse displacement of the droplets due to the diffusion is significant compared to the inter-fiber distance s . **Figures 2.4** presents maps of the Π values for different s , d_p and U and a fixed value of fiber radius ($a = 50 \text{ } \mu\text{m}$) in the absence (**Panel A**) and presence (**Panel B**) of electric fields. Since each data-point in **Figure 2.5** represents the outcome of 5

simulations under identical set of parameters, Π assumes 6 discrete values. As can be seen from **Figure 2.4**, smaller inter-electrode spacing ($s = 500 \mu\text{m}$) consistently yields higher levels of Π across various particle sizes and free-stream velocities. This may be attributed to the greater extent of geometric interception due to the larger fractional area coverage by the electrodes (denoted by the grey shaded regions in **Figure 2.4**). Interestingly, the Π values for the smaller droplets are found to be higher than that of the larger droplets, particularly at the lower range of U , which is an outgrowth of the enhanced Brownian deposition. For larger droplets, this contribution diminishes, primarily due to the increase of the drag force relative to the Brownian force ($F_D/F_B \propto d_p^{1/2}$) with increasing particle diameter (d_p). Therefore, larger droplets are more easily carried along the flow streamlines. Furthermore, at larger flow velocity, inertial deposition is found to dominate, which is reflected in the very high occurrence of capture ($\Pi = 5/5$) in the electrode regions, flanked on its either sides by zones of extremely low Π values (1/5 or 0) in **Figure 2.4**. For more data on the impact of the electrode configurations on particle capture probabilities, refer to **Figure A4-A** in *Appendix A*, which presents a similar map of the Π values for different fiber diameters a while maintaining a fixed s in the absence of any electric field.

Having identified the trend of interception, inertial impaction and Brownian walk dominated particle capture under different design and operating conditions, we now investigate the influence of the DEP force on the particle capture. **Figure 2.4-B** shows the parametric mapping of Π for the same conditions described in **Figure 2.4-A**, with the exception that a 3-phase AC voltage (at $f = 50 \text{ Hz}$) is now imposed on the electrodes. Depending upon the inter-electrode spacing s , the applied voltage Φ_0 is adjusted to maintain the same nominal electric field E_0 of 2.8 kV/mm . As evident from the particle trajectories described in the previous section, the DEP force is at competition with the Brownian force for smaller droplets, while for larger droplets, the capture is decided through a competition between the inertial, drag and DEP forces. Comparison of **Figures 2.4-A** and **2.4-B** clearly shows improving influence of DEP force on the overall particle capture. The presence of traveling electric field significantly improves the occurrence of particle capture within the examined entire parameter space (s, d_p, U).

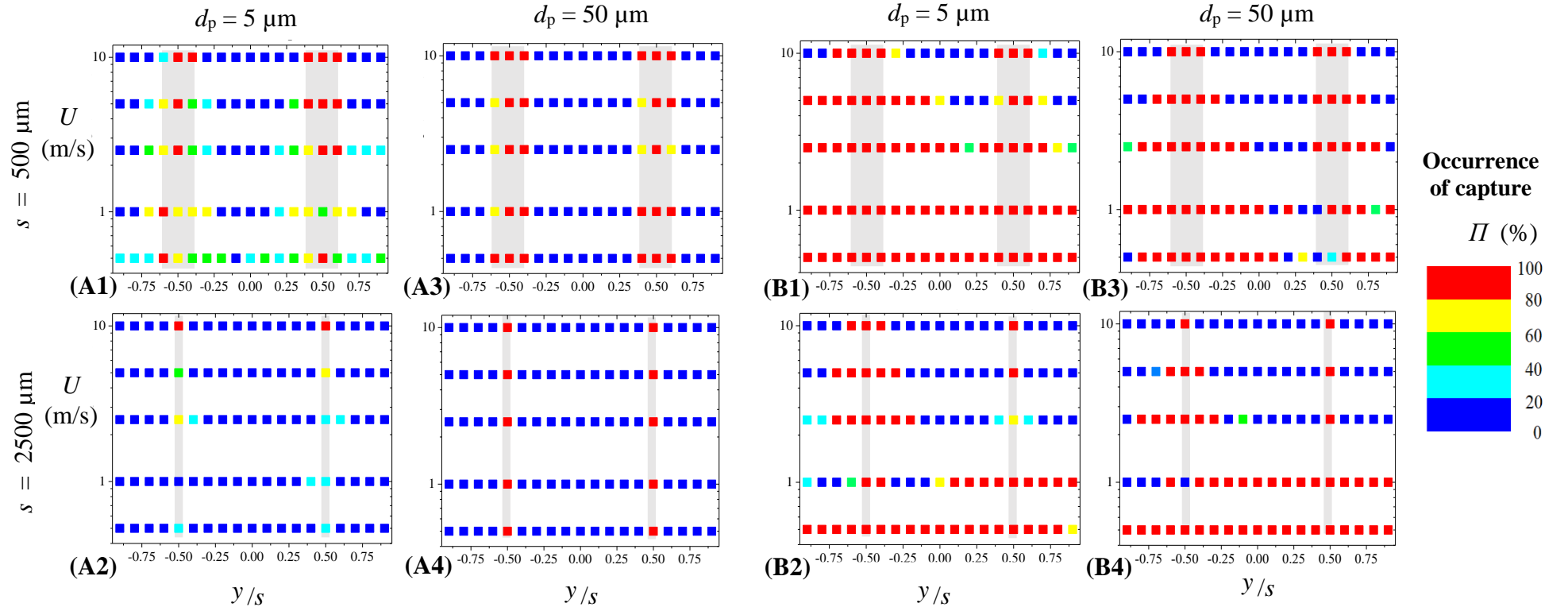


Figure 2.4: (A) Occurrence of capture Π mapped as functions of their transvers position of release ($-1 \leq y/s \leq +1$ at the inlet plane) and the inlet flow velocity U (0.5, 1, 2.5, 5 and 10 m/s), in absence of any electric field, for a constant fiber radius $a = 50 \mu\text{m}$. Fiber spacing and particle size are varied as $s = 500 \mu\text{m}$ (A1, A3) and $2500 \mu\text{m}$ (A2, A4) and $d_p = 5 \mu\text{m}$ (A1, A2) and $50 \mu\text{m}$ (A3, A4), respectively. (B1 through B4) Identical parametric plots under the same conditions, except that a 3-phase AC voltage (at $f = 50 \text{ Hz}$) is now imposed on the electrodes with electric field strength (Φ_0/s) of 2.8 kV/mm . Each data-point represents the outcome of 5 simulations under identical set of parameters, yielding 6 discrete values of Π . Colour legend: $\Pi = 5/5$ (red), $4/5$ (yellow), $3/5$ (green), $2/5$ (cyan), $1/5$ and 0 (shown together in blue). Grey-shaded regions indicate the obstruction in flow path by the fibers/electrodes.

At the lower regimes of U , nearly all the simulations yield capture. This implies that irrespective of the release location (y/s at the inlet plane), droplets are pulled by the DEP force to the electrodes, arriving at the zone of strong electric field intensity. On the contrary, at larger values of U , the droplets that are released from inlet y/s close to the transverse positions of the electrodes exhibit high values of Π . This clearly insinuates that the fluidic drag and axial inertia of the droplets act against the DEP capture. Like in the case of the zero-field capture (**Figure 2.4-A**), a closely spaced arrangement of electrodes ($s = 500 \mu\text{m}$, **Figures 2.4-B1 and B3**) shows greater trend of DEP-induced capture. For DEP capture, a reduced s implies that the zone of influence of the electric field gradient covers a wider space between neighbouring electrodes, and hence the droplets have a lower chance of escape. The influence of particle size on the capture is less prominent in the DEP-capture as compared to the no-field case. This may be attributed to the fact that both the inertial and DEP forces scale with the third power of d_p and these two competing forces mask the effects of the viscous drag (which scales linearly with d_p) and the Brownian fluctuations. At smaller particle size and smaller gas stream velocity, particularly for the case of large s (**Figure 2.4-B2**), the Brownian capture is more apparent than the other three conditions, as marked by a larger occurrence of the intermediate Π values (e.g., $4/5$, $3/5$ or $2/5$). **Figure A4-B** in the *Appendix A* presents a detailed outcome of a similar parametric variation of **Figure 2.4**, except that the fiber inter-spacing is held constant (at $s = 1500 \mu\text{m}$) while the fiber diameter is varied between 50 to $150 \mu\text{m}$.

2.4 Effects of varying electric field strength

While the impact of DEP on particle capture is evident from the previous section, we now show the effect of varying the electric field strength on the particle capture probability for a given particle size and electrode radius. **Figure 2.5** presents maps of the Π values for different inlet flow velocity U (0.5 , 1 , 2.5 , 5 and 10 m/s) for a fixed fiber radius $a = 50 \mu\text{m}$ and particle size $d_p = 10 \mu\text{m}$ under three different field strengths. The nominal electric field strength $E_0 = (\Phi_0/s)$ in **Figures 2.5-A, B, and C** are 2.8 , 0.93 and 0.56 kV/mm , respectively. This is achieved by keeping the imposed voltage $\Phi_0 = 1.4 \text{ kV}$ and varying the inter-electrode spacing as $s = 500$, 1500 and $2500 \mu\text{m}$, respectively. The nominal electric field E_0 for the case shown in **Figure 5-D** is maintained at 2.8 kV/mm (corresponding to $\Phi_0 = 4.2 \text{ kV}$ with $s = 1500 \mu\text{m}$), which is equal to the E_0 for the case of **Figure 5-A**. For all the cases, 3-phase AC at $f = 50 \text{ Hz}$ is used. A comparison of **Figures 5-A, B and C** reaffirms that the DEP collection decreases with decreasing the field strength. At higher field strength (**5-A**), particle capture is nearly pervasive irrespective of its y/s location of release up to a flow velocity of 1 m/s , while at lower

field strengths (**Figure 5-B and C**), regions of high occurrence of capture get narrowed down only around the electrodes. Also, with increasing flow velocity, these capture regions progressively narrow down and localize near the electrodes, irrespective of the applied electric field. This trend underscores the critical role of particle velocity in determining capture probability within mesh configurations – with higher velocities leading to narrower capture regions, primarily influenced by Stokes drag.

It is also interesting to compare the capture patterns between Figures 5-A and 5-D, for which the for which the $E_0 = \Phi_0/s$ values are the same, but the difference in geometric coverage of the electrodes lead to different extents of electric field gradients ($\nabla|E|$). (see Figure S2 of the *ESI*) For the case of closely spaced electrode arrangements (Figure 5-A), the field gradient is stronger than that with sparsely placed electrodes (Figure 5-D). Therefore, the DEP force, which scales proportional to ∇E^2 , is stronger in the former case, leading to the higher values of Π values on the U - y/s plane. It is also interesting to note in **Figures 2.5-A and 2.5-D** that the spatial distribution of Π values with respect to the two electrodes are asymmetric, displaying higher range of Π around the left electrode. This trend is perceptible, albeit with a scatter due to the Brownian stochasticity at small d_p , under all the DEP-capture cases in **Figure 2.4-B and 2.5**. This asymmetry is attributed to the phase sequence of the 3-phase voltage waveform applied to the electrodes. A study with different phase sequence (See **Figure A5** in the *ESI*) reveals that the distribution is skewed differently when the phase sequence is advanced by $2\pi/3$ or $4\pi/3$. This trend also underlines the dynamic nature of the DEP capture effected by the travelling 3-phase electric field.

2.5 Effect of varying operating frequency

Figure 2.6 describes the impact of frequency modulation of the 3-phase traveling electric field on particle capture for three representative particle sizes, viz., $d_p = 5, 10$ and $50 \mu\text{m}$. The frequency of the applied 3-phase field is increased from 50 Hz to 8000 Hz, while keeping the voltage constant. We focus on the sparsest filter configuration, featuring an electrode radius $a = 50 \mu\text{m}$ and an inter-fiber spacing $s = 2500 \mu\text{m}$, so that the effects of interception is minimal and the DEP force is not pervasively overpowering everywhere. Also, an intermediate level of velocity, $U = 2.5 \text{ m/s}$, is chosen so that the inertia and drag forces are comparable to the DEP forces at locations away from the electrodes. This is intentionally chosen to ensure that a wide spatial variation of Π is observed over the operating regime. For all the three particle sizes and operating frequency, **Figure 2.6** shows capture of the droplets are high in the electrode regions.

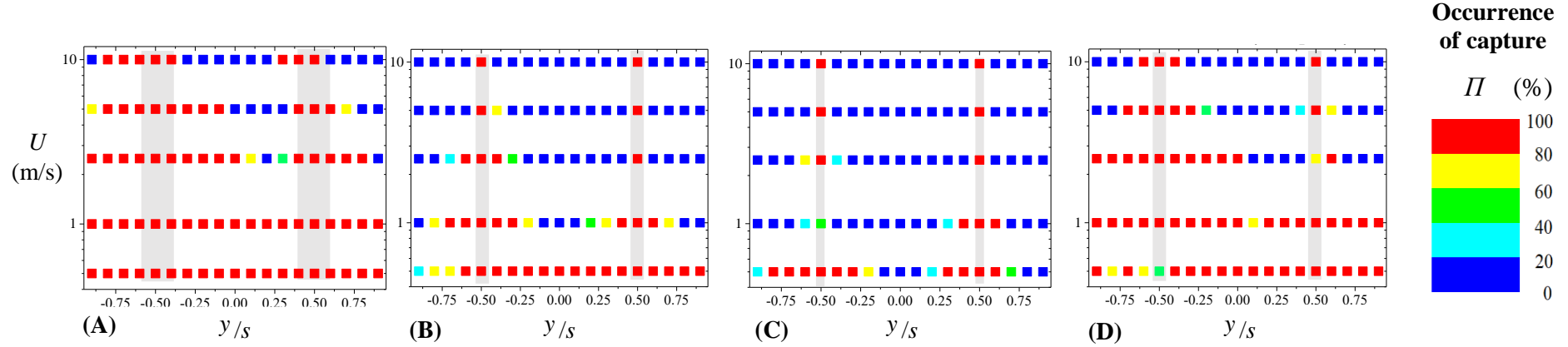


Figure 2.5: Effect of varying the electric field on Π vs y/s plots for different inlet flow velocity U (0.5, 1, 2.5, 5 and 10 m/s) for a fixed fiber radius $a = 50 \mu\text{m}$ and particle size $d_p = 10 \mu\text{m}$. Variation of $E = (\Phi_0/s)$ is obtained either by keeping the voltage constant at $\Phi_0 = 1.4 \text{ kV}$ and varying the inter-electrode spacing as (A) $s = 500 \mu\text{m}$, (B) $s = 1500 \mu\text{m}$ and (C) $s = 2500 \mu\text{m}$, or by (D) adjusting the applied voltage at $\Phi_0 = 4.2 \text{ kV}$ while maintaining the inter-electrode spacing $s = 1500 \mu\text{m}$. For all cases, 3-phase AC at $f = 50 \text{ Hz}$ is used. The imposed electric field magnitude scales with (Φ_0/s) , implying that the E fields in (A) and (D) are the same, while those in (B) and (C) are, respectively, $1/3^{\text{rd}}$ and $1/5^{\text{th}}$ of that in (A). Colour legend: $\Pi = 5/5$ (red), $4/5$ (yellow), $3/5$ (green), $2/5$ (cyan), $1/5$ and 0 (shown together in blue). Grey-shaded regions indicate the obstruction in flow path by the fibers/electrodes.

However, in the inter-electrode space, the value of Π is found to depend on the frequency; this variation is non-monotonic in nature as the frequency is increased. A close look of the Π in **Figure 2.6** shows that the extent of particle capture is high at some frequency (e.g., $\Pi = 5/5$ for droplets released from 14 of the 20 normalised y locations for $f = 4000, 4500$ and 8000 Hz in **6C**) and low very next to it (e.g., $\Pi = 5/5$ for 10 of the 20 normalized y locations for $f = 2000$ Hz, or in 11 of the 20 normalised y locations for $f = 3500$ Hz in the same plot).

This provides an inkling that the combined dynamics of particle motion and the speed of the travelling electric field plays a key role in deciding the extent of particle capture. As may be seen from **Figure A6** in the *ESI*, the effect of varying the frequency of imposed electric field ($f \in [50, 8000]$ Hz) on Π vs y/s plots for other velocities also (viz. $U = 1$ m/s and 5 m/s) agree with the general trend of **Figure 2.6**. Although the trend in **Figure 2.6** hints at the dependence of particle capture on frequency modulation, it does not offer definitive evidence regarding the direct impact of frequency on particle capture efficiency. To understand the intricate interplay amongst the geometric and flow parameters and the magnitude and frequency of the applied voltage it is important that the effects are examined collectively on an array of droplets that are released from different normalised y locations.

2.6 Average collection efficiency

The collective impact on particle capture on the electrode assembly is denoted by an average collection efficiency η_a which is defined as the overall incidents of capture when the droplets are released from 20 transverse (i.e., normalised y) positions, with 5 repeat runs for each release location. Therefore,

$$\eta_a = \frac{\text{Number of droplets captured at any of the electrodes}}{\text{Number of droplets released from all the normalised } y \text{ positions}} \quad (2.13)$$

The denominator in **Eq. (2.13)** is, therefore, 100 for a particular operating condition (d_p, U, s, a) , rendering statistically significant data of particle capture efficiency. Since the interaction between the travelling electric field and the flow field is dynamic in nature, it is imperative that the particle capture behavior is resolved in terms of the pertinent time scales. It appears from the foregoing results that the dispersed phase flow involves not just one-time scale, which is derived from the supply voltage frequency; there is a time scale associated with the flow as well (the Brownian time scale, which gives rise to stochasticity in the particle dynamics is ostensibly much smaller than the flow and electric field time scales, and its influence is averaged out over the repeat runs; therefore, we do not reckon this time scale).

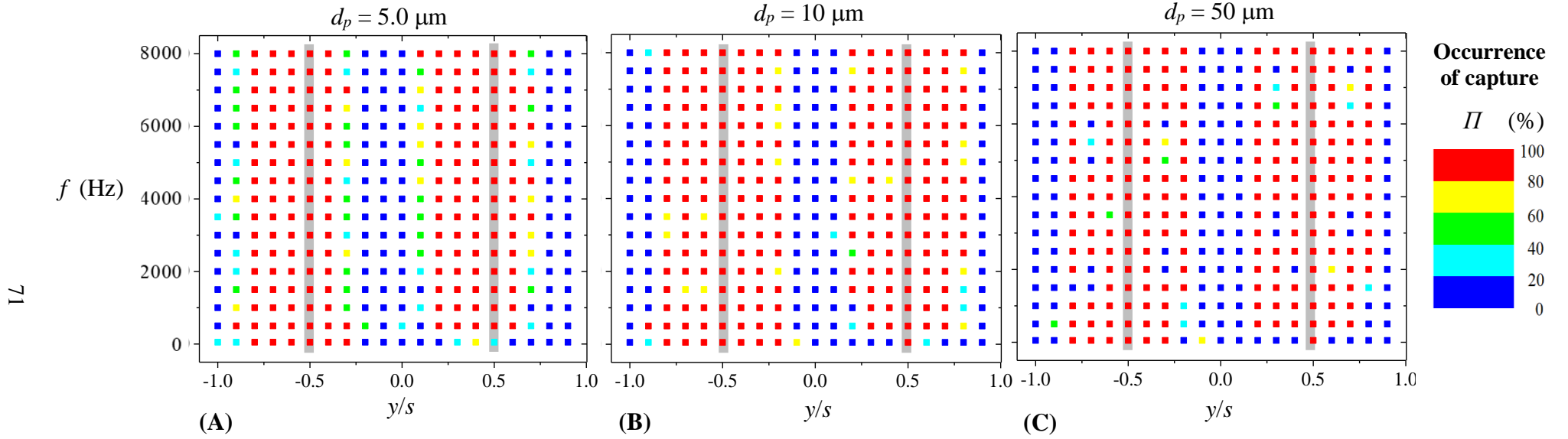


Figure 2.6: Effect of varying the frequency of imposed electric field ($f \in [50, 8000]$ Hz) on Π vs y/s plots for three different particle size, viz., (A) $d_p = 5 \mu\text{m}$, (B) $d_p = 10 \mu\text{m}$, and (C) $d_p = 50 \mu\text{m}$. For all the cases, $U = 2.5 \text{ m/s}$, $s = 2500 \mu\text{m}$ and $a = 50 \mu\text{m}$ and, $\Phi_0 = 7 \text{ kV}$, corresponding to a nominal electric field $E = 2.8 \text{ kV/mm}$. Colour legend: $\Pi = 5/5$ (red), $4/5$ (yellow), $3/5$ (green), $2/5$ (cyan), $1/5$ and 0 (shown together in blue). Grey-shaded regions indicate the obstruction in flow path by the fibers/electrodes.

To comprehensively grasp the intricate interplay of factors influencing particle trajectories, an analysis of particle response with respect to the major forces is essential. The dynamics of particle transport and capture by the electrodes is governed by a balance of the DEP, inertia and drag forces.

The DEP force has a spatiotemporal distribution, with a temporal frequency of f giving a time scale $\tau_f = 1/f$, which characterizes how slowly the directionality of the 3-phase voltage changes. Considering the fact that the DEP force is spatially confined to a narrow region (which has a length-scale of the inter-electrode spacing s) around the electrodes, it only has a limited time-window to compete with the drag and inertial forces and influences the particle trajectories (i.e., whether it will be captured or will escape) as the droplets pass through the electrode region. Therefore, the flow residence time-scale ($\tau_r = s/U$) represents the duration it takes for a particle to traverse a distance s in a cross-flow over the electrode assembly. The ratio of τ_r to τ_f characterizes the effects of unsteadiness of electric fields on the particle dynamics:

$$\frac{\tau_r}{\tau_f} = \frac{fs}{U} \quad (2.14)$$

A smaller τ_r/τ_f ratio implies more sluggish (but not necessarily weak, as the DEP force magnitude in **Eq. (2.2)** does not depend on the frequency) dielectric response, implying that the droplets pass through the electrode region only during a small part of one complete voltage cycle. Conversely, a larger τ_r/τ_f ratio indicates a longer flow residence time, allowing droplets to interact with traveling electric field over several voltage cycles as they pass over the electrode array section.

Figure 2.7 presents the frequency-dependent behavior of η_a against the time-scale ratio τ_r/τ_f for four particle diameters (5, 10, 25 and 50 μm) and three different free-stream velocities ($U = 1, 2.5, \text{ and } 5 \text{ m/s}$) for a given mesh geometry and electric condition: $s = 500 \mu\text{m}$, $a = 50 \mu\text{m}$ and $E_0 = 2.8 \text{ kV/mm}$ (i.e., $\Phi_0 = 1.4 \text{ kV}$). Colored dots on the plot represent the average capture efficiency estimated from 100 individual runs. Highlight of **Figure 2.7** is the occurrence of distinct localized regimes of high and low η_a values as the τ_r/τ_f ratio is changed due to the variation of the imposed field frequency within the range $f \in [50, 8000] \text{ Hz}$. For $U = 1 \text{ m/s}$ (**Figure 2.7-A**), the η_a value is observed to peak in a near-cyclic fashion with an average $\frac{\tau_r}{\tau_f}$ interval of ~ 0.35 (6 collection peaks between $0.25 \leq \tau_r/\tau_f \leq 2.0$). For $U = 2.5 \text{ m/s}$ (**Figure 2.7-B**), and 5 m/s (**Figure 2.7-C**), similar periodicity prevails with comparable peak-to-peak interval. The range of variation of the η_a values (i.e., the difference between the maximum and minimum η_a) is found to be more prominent with increasing U . With the increase of the flow velocity, however, the η_a values consistently decreases across the entire spectrum of τ_r/τ_f , regardless of particle diameter. This trend aligns well with the findings reported in the preceding sections. It

is interesting to note that the periodic fluctuation of the η_a value is almost not perceptible in for $d_p = 5 \mu\text{m}$ (**Figure 2.7-A**), which may be attributed to the strong Brownian fluctuations of these droplets under the lowest U . The high capture efficiency, in this case, occurs primarily due to the Brownian walk of the droplets, and hence its trend is insensitive to the flow or the voltage time scales. However, at higher velocities (**Figure 2.7-B and 2.7-C**), the Stokes drag becomes stronger and, akin to the other droplets, the capture efficiency for the $5 \mu\text{m}$ droplets shows the cyclic variation with τ_r/τ_f .

Figure 2.7 suggests the presence of optimal frequencies of the imposed voltage waveform, at which the filter operates most efficiently. This implies that it is possible to “tune” the electrode assembly for augmentation of the particle capture efficiency. The tuning parameters, and the extent of improvement of capture through frequency modulation will however be dependent on the other design and operating parameters. In order to develop a generalized strategy of tuning the particle capture, we reckon the other pertinent time constants associated with the particle transport. As the droplets experience transverse force due to DEP while passing through the electrode region, they experience a departure from the flow streamline, and develop a slip velocity. The response time for the resulting Stokes drag force, τ_{St} , reflects how quickly particle responds to changes in slip velocity. This may be obtained by balancing the particle inertia with the drag force, so that

$$m_p \frac{U}{\tau_{St}} \sim \frac{3\pi\mu d_p}{C} U \quad (2.15)$$

Expanding the particle mass in terms of its density and size, the Stokes time constant is estimated as

$$\tau_{St} \sim \frac{C\rho_p d_p^2}{18\mu} \quad (2.16)$$

In contrast, the response time τ_{DEP} for dielectrophoretic force indicates particle response to changes in the electric field, which may be deduced by equating the particle inertia with the DEP force. Considering that the electric field scales with Φ_0/s , and its gradient involves the same length scale s , the balance may be expressed as

$$m_p \frac{U}{\tau_{DEP}} \sim \frac{\pi}{4} d_p^3 \varepsilon_0 \varepsilon_r K_{CM} \frac{1}{s} \left(\frac{\Phi_0}{s} \right)^2, \quad (2.17)$$

and the pertinent DEP time scale reduces to

$$\tau_{DEP} \sim \frac{2\rho_p U s^3}{3\varepsilon_0 \varepsilon_r K_{CM} \Phi_0^2} \quad (2.18)$$

The relative significance of these forces is assessed through the ratio $\frac{\tau_{St}}{\tau_{DEP}}$ which is expressed as

$$\frac{\tau_{St}}{\tau_{DEP}} = \frac{C\varepsilon_0 \varepsilon_r K_{CM} d_p^2}{12\mu U s} \left(\frac{\Phi_0}{s} \right)^2 \quad (2.19)$$

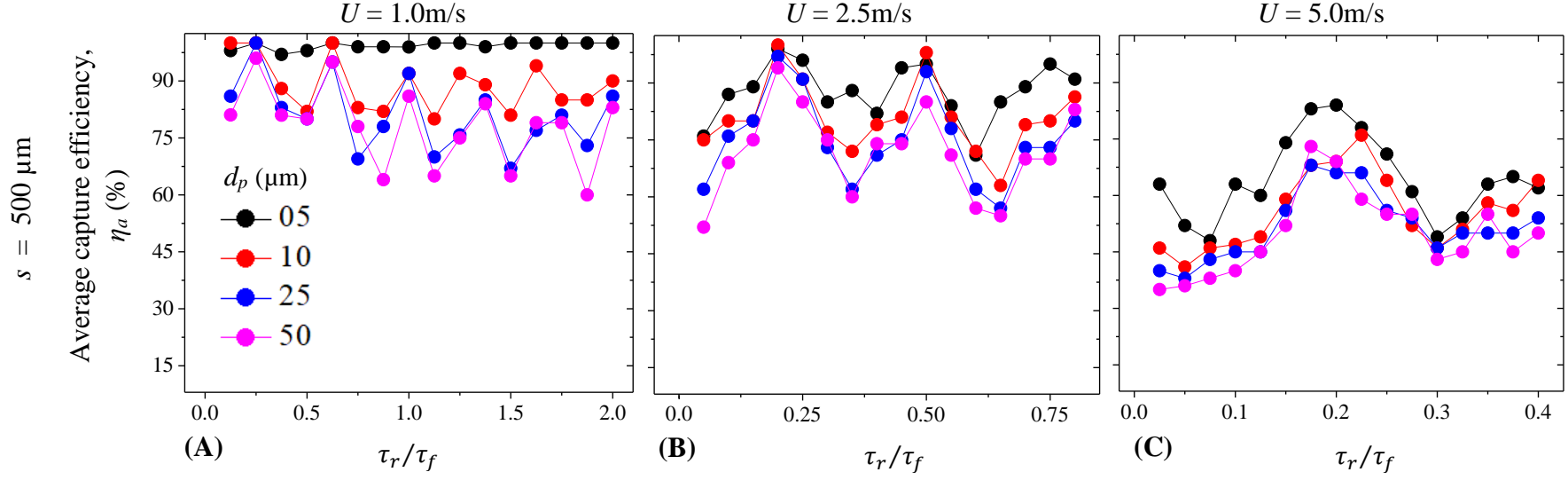


Figure 2.7: Average capture efficiency, η_a , (computed over 100 runs), plotted against the $\frac{\tau_r}{\tau_f} = \frac{f \times s}{U}$ for different particle size and flow velocity, U (A) 1 m/s (B) 2.5 m/s and, (C) 5 m/s for the densest filter ($a = 50 \mu\text{m}$, $s = 500 \mu\text{m}$) is plotted. The electric field strength (Φ_0/s) has been maintained at 2.8 kV/mm. As frequency increases, local maxima and minima appear, indicating a critical factor in designing dielectrophoretic filters. η_a exhibits cyclic maxima and minima as the frequency is varied over the spectrum $f \in [50, 8000]$ Hz.

When $\frac{\tau_{St}}{\tau_{DEP}} \gg 1$, dielectrophoretic forces take precedence, causing swift alterations in the particle trajectories towards the electrodes. Conversely, when $\frac{\tau_{St}}{\tau_{DEP}} \ll 1$, Stokes drag forces dominate, and the droplets primarily respond to fluid flow changes. Therefore, to get a quantifiable estimate of the overall performance of the DEP-based droplet/particle filtration system, the average capture efficiency η_a is mapped on the normalized scales of $\frac{\tau_{St}}{\tau_{DEP}}$ (along the ordinate) and $\frac{\tau_r}{\tau_f}$ (along the abscissa) in **Figure 2.8-A** through **2.8-D** for four different particle sizes. Data represented in **Figure 2.8** lie within the parametric operation regimes of U ($\in [0.5 - 10]$ m/s) and f ($\in [50, 8000]$ Hz), while for all simulations $a = 50 \mu\text{m}$ and $s = 500 \mu\text{m}$ and E_0 is maintained at 2.8 kV/mm. The colour maps represent η_a , ranging from the high (100% capture, marked in red) to the low (0% capture, marked in blue). The dotted boundaries at the top and bottom of the plots represent the lower (0.5 m/s) and the upper (10 m/s) extremes of U , respectively; the inclined regime boundaries on the left and right coincide with the frequency limits of 50 and 8000 Hz, respectively. The white regions lie beyond the operating regime. The general trend observed in the four plots of **Figure 2.8** agrees with the argument that a larger value of $\frac{\tau_{St}}{\tau_{DEP}}$ associates with a higher DEP force, and hence a higher η_a . All the four plots in **Figure 2.8-A** through **2.8-D** show self-similar regime maps in the operating range, with its ordinate of

iso- η_a lines shifting upward nearly in proportion to d_p^2 as the particle diameter is increased from 5 to 50 μm . This trend can be explained from a simple scaling argument of the driving forces on the droplets. In general, for a successful capture of the particle, the DEP force (F_{DEP}) must overpower the drag (F_{drag}) and the inertial ($F_{inertia}$), components, which implies

$$\frac{F_{inertia} + F_{drag}}{F_{DEP}} < \Gamma, \quad (2.20)$$

where Γ , is a constant signifying the regime of high capture. **Eq. (2.20)** may be rearranged as

$$\frac{F_{DEP}}{F_{drag}} > \frac{1}{\Gamma} \left(1 + \frac{F_{inertia}}{F_{drag}} \right). \quad (2.21)$$

By definition, the left hand side term of **Eq. (2.21)** scales with the $\frac{\tau_{St}}{\tau_{DEP}}$ ratio. Also, since the inertia and drag forces scale with d_p^3 and d_p , respectively, the ratio $\frac{F_{inertia}}{F_{drag}}$ on the right-hand side scales with d_p^2 . Therefore, **Eq (2.21)** reduces to

$$\frac{\tau_{St}}{\tau_{DEP}} > \frac{1}{\Gamma^*} (1 + \Psi d_p^2), \quad (2.22)$$

where Γ^* and Ψ are also some constants. **Eq. (2.22)** explains the general trend of increased threshold requirement of $\frac{\tau_{St}}{\tau_{DEP}}$ to attain a target η_a , which is exactly what is observed in **Figure 2.8**. Also, across the range of the investigated operating parameters, the overall spread of high-

η_a regime is found to be the highest for the smallest particle, i.e., $d_p = 5 \mu\text{m}$ (**Figure 2.8-A**); this decreases with increasing d_p (**Figure 2.8-B through D**). The trend may also be attributed to the more stringent requirement of $\frac{\tau_{St}}{\tau_{DEP}}$ for larger droplets for successful capture (see **Eq. 2.22**). Therefore, the proposed DEP filtration is particularly advantageous for the smaller particle range in a practical filtration system, where the particle polydispersity is an unavoidable scenario.

Besides these general observations on **Figure 2.8**, it is interesting to note the existence of conspicuous vertical bands of high η_a , appearing at $\frac{\tau_r}{\tau_f} = 0.2, 0.5$ and 0.8 for all the four particle sizes. There are also less conspicuous peaks of η_a at higher $\frac{\tau_r}{\tau_f}$ values, e.g., $1.1, 1.4$, etc. which are, apparently uniformly spaced on the $\frac{\tau_r}{\tau_f}$ axis. This implies that, for the range of operating conditions and particle size investigated here, particle capture efficiency can be significantly improved by appropriately “tuning” the value of $\frac{\tau_r}{\tau_f}$ – by varying either U or f – as described in **Figure 2.8**.

Figure 2.8.

Since $\frac{\tau_r}{\tau_f} = \frac{fs}{U}$, it is also vital to verify if this feature of tunability persists even when the frequency is held constant, and the other two parameters, viz., U and s are varied. With this aim, **Figure 2.9-A through 2.9-D** shows maps of efficiency η_a on the $\frac{\tau_{St}}{\tau_{DEP}}$ versus $\frac{\tau_r}{\tau_f}$ plane for four particle sizes, viz., $d_p = 5, 10, 25$ and $50 \mu\text{m}$, for the same set of parameters of **Figure 2.8**, i.e., $E_0 = 2.8\text{kV/mm}$, $a = 50 \mu\text{m}$ and $U \in [0.5 - 10] \text{ m/s}$, with the exceptions that the electrode spacing s is varied ($\in [500, 2500] \mu\text{m}$), and the operating frequency is held constant at $f = 50 \text{ Hz}$. Like in **Figure 2.8**, the capture regime maps observed in the **Figure 2.9** also indicate that a higher η_a value is realized at larger values of $\frac{\tau_{St}}{\tau_{DEP}}$, and the threshold of $\frac{\tau_{St}}{\tau_{DEP}}$ for a desired capture efficiency increases in proportion to d_p^2 .

Moreover, within the range of operating parameters, the capture efficiency map of **Figure 2.9** also shows local regimes of higher η_a value at discrete points on the $\frac{\tau_r}{\tau_f}$ axis, e.g., 0.02 and 0.1 . However, the effect of variation of electrode spacing on the tunability aspect is less as compared to varying the operating frequency.

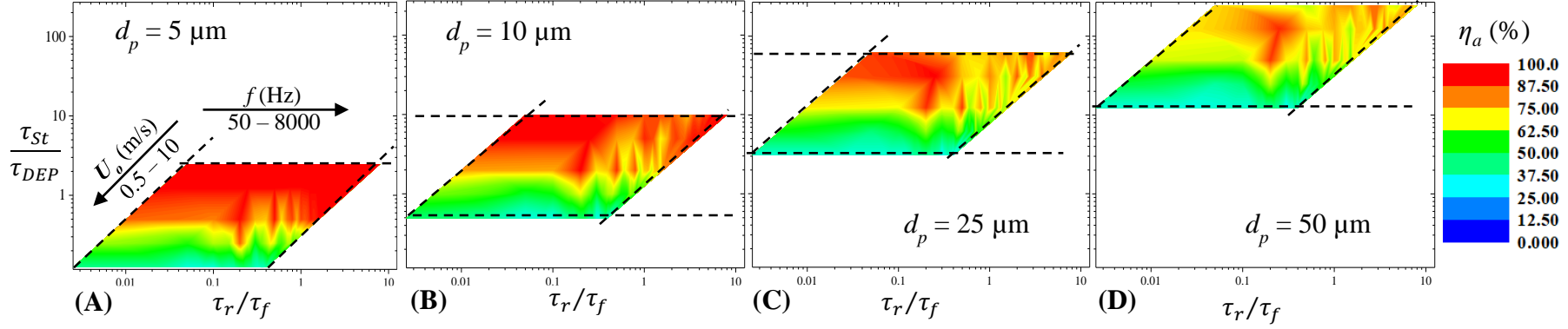


Figure 2.8: Average capture efficiency map, with η_a plotted against $\frac{\tau_{St}}{\tau_{DEP}} = \frac{C\varepsilon_0\varepsilon_r K_{CM} d_p^2}{12\mu U s} \left(\frac{\Phi_0}{s}\right)^2$ and the $\frac{\tau_r}{\tau_f} = \frac{f \times s}{U}$ within the parametric operation regimes of U ($\in [0.5 - 10]$ m/s) and f ($\in [50, 8000]$ Hz), for four different particle sizes. For all simulations the mesh geometry is constant, i.e., $a = 50 \mu\text{m}$ and $s = 500 \mu\text{m}$, and $E_0 = 2.8$ kV/mm. The white regions, lying beyond the dotted black lines, represents conditions beyond the regimes of current investigation.

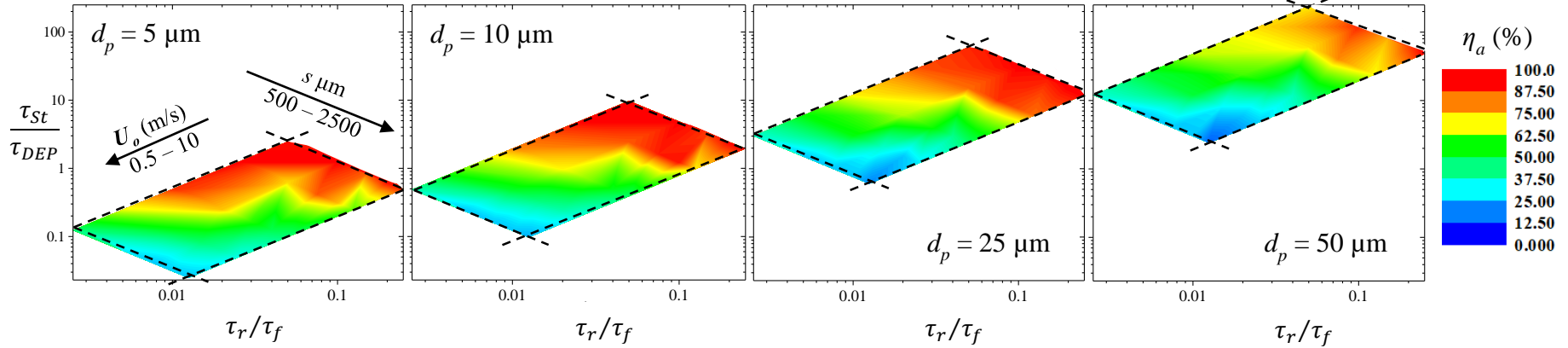


Figure 2.9: Average capture efficiency map, with η_a plotted against $\frac{\tau_{St}}{\tau_{DEP}} = \frac{C\varepsilon_0\varepsilon_r K_{CM} d_p^2}{12\mu U s} \left(\frac{\Phi_0}{s}\right)^2$ and the $\frac{\tau_r}{\tau_f} = \frac{f \times s}{U}$ within the parametric operation regimes of U ($\in [0.5 - 10]$ m/s) and s ($\in [500, 2500]$ μm), for four different particle sizes. For all simulations $a = 50 \mu\text{m}$ and $f = 50$ Hz, and $E_0 = 2.8$ kV/mm. The white regions, lying beyond the dotted black lines, represents conditions beyond the regimes of current investigation.

2.7 Merits of DEP filtration

An efficient air filter must strike a balance between maintaining high particle capture efficiency and keeping the airflow resistance at an acceptable level. Hence, both filter penetration and aerodynamic resistance are pivotal when evaluating a filter performance. The filter quality factor, Q_F , which serves as a measure of the performance of the filtration device, and is also referred to as figure of merit in previous studies [119]; 120], is calculated as

$$Q_F = \frac{\ln\left(\frac{1}{1-\eta_a}\right)}{\Delta P} \quad (2.23)$$

Here, η_a represents filtration efficiency, and ΔP is the pressure drop across the filter. The quality factor signifies capture efficiency per unit pressure drop across a filter. An effective filter, characterized by a high filter quality, should exhibit both high collection efficiency and minimal air resistance, as indicated by a low maximum pressure drop across the filter. Achieving this balance often involves factors like lower packing density (such as increased inter-fiber spacing, thinner fiber diameter, or a large s/a ratio), all of which can result in lower collection efficiency. Therefore, it is crucial to determine the optimal trade-off between these requirements.

Figure 2.10 shows the non-dimensionalized pressure drop $\left(\frac{\Delta P}{\mu U/s}\right)$ across the electrode array, computed following Miyagi's solution [113], for $s \in [500, 2500]$ and $a = 50 \mu\text{m}$. This allows us to compute the pressure drop across the mesh for all considered free stream velocities and is highlighted in red. The inset in the figure presents the pressure drop incurred for the various velocities considered. For $s/a = 10$, $a = 50 \mu\text{m}$, our DEP-based filters exhibit a maximum pressure drop (ΔP) of 4.53 Pa at $U = 10 \text{ m/s}$, and a minimum of $\Delta P = 1.90 \times 10^{-2} \text{ Pa}$ (at $U = 0.5 \text{ m/s}$ (inset)). Our DEP-based filter offers a remarkably low pressure drop due to the sparse arrangement of fibers ($s/a > 10$). This in turn results in a high Q_F as compared to the other commercially available filters in **Table A1** of the **Appendix A**. This approach offers advantages over electrophoresis-based filters, such as not requiring arc discharge and the ability to use AC power. This feature, coupled with the option of “tunability” of the filter shows its advantageous deployment in crucial healthcare environments, advanced face masks, home air filters, and even in industrial settings like oil-vapour extraction.

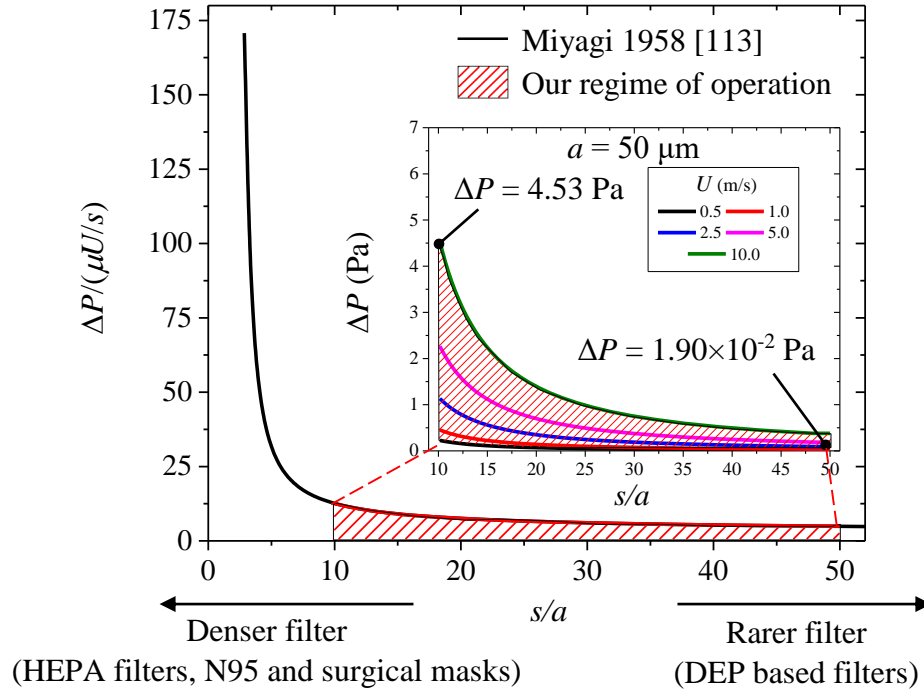


Figure 2.10: Normalized pressure drop as a function of s/a computed from the analytical solution of Miyagi [113]. The **INSET** displays the dimensional pressure drop across filters for $a = 50 \mu\text{m}$, meeting the condition $s/a \in [10, 50]$, for different free stream velocities. Our operational regime is highlighted in red.

Chapter 3
**Droplet morphology-based wettability tuning and
design of fog harvesting mesh to minimize mesh-
clogging**

3. Clog resistant meshes for efficient fog capture

Traditional metal or polyester meshes are susceptible to clogging [121]. To overcome this issue, a comprehensive approach to optimize mesh design parameters and surface characteristics, with the goal is to develop highly efficient fog collectors that resist clogging and maximize water yield is needed. For optimal collection efficiency, the fog net should intercept fog, and the collected droplets should smoothly slide down the mesh to the designated collector. Clogging of mesh pores should be avoided, as it obstructs the oncoming fog stream, diverting the fog plume and significantly reducing collection efficiency. The fraction of fog deposited on the fog collecting mesh is determined by the product of the mesh's aerodynamic and deposition efficiencies. Aerodynamic efficiency (η_a) represents the fraction of the unperturbed oncoming flow directed towards the mesh fibers, while deposition efficiency (η_d) represents the fraction of directed fog droplets that eventually deposit on the fibers. Aerodynamic efficiency depends on the shade coefficient, defined as the fraction of projected mesh area blocked by the fibers or water droplets adhering to them.

Progressive deposition of these fog-droplets and subsequent coalescence of the deposited liquid lead to the formation of bigger droplets (O (~1 mm)) of different shapes on the fibers. These growing droplets may eventually touch the neighboring mesh fibers, when they clog the mesh pore either partly or completely (see **Figure 3.1-A**).

The vulnerability of a mesh to clog, as already mentioned, depends on the geometry of the mesh and its surface wettability (characterized by the apparent contact angle; see **Figure 3.1-A inset**). This leaves rooms for mesh design improvement through appropriate choice of mesh wettability and geometry. To design a 'clog-proof' interwoven metal mesh (**Figure 3.1-B**), it is logical to comprehend the behaviour and morphology of deposited fog-water droplets during their evolution (see **Figure 3.1-C**) on the mesh elements [122, 123].

A drop on the fiber of a fog harvesting mesh grows by consequent droplet coalescence and fog deposition, wherein it can assume either an axisymmetric barrel shape or an asymmetric clamshell shape (see **Figure 3.1-C**) [124, 125]. The droplet detaches from the fiber when its weight exceeds its adhesion force with the fiber [126, 127]. However, there is another possibility: the droplet may stretch transversely or laterally to reach neighboring mesh fibers and form capillary bridges, thereby leading to an increase of surface adhesion force and preventing detachment [77]. A droplet interacting with more than one fiber can therefore acquire larger volumes before it would detach [128], and hence accentuate the chance of clogging up the mesh pore. This would not only reduce the intended drainage of the collected

fog-water (into the designated collector) but also increase aerodynamic resistance, thereby reducing total mesh efficiency. While there have been multiple studies on the development of novel mesh designs or suitable surface modifications [129] to improve fog collection, few have investigated into the understanding of the interwoven mesh geometry parameters and droplet morphology interactions that lead to clogging [32]. Herein, the study attempts to theoretically design the salient fog harvesting mesh parameters, viz., the fiber diameter and inter-fiber spacing, by drawing heavily from droplet morphology, such that a pendant droplet on a fiber does not grow large enough to contact the neighbouring mesh fibers thereby ensuring a clog-proof design.

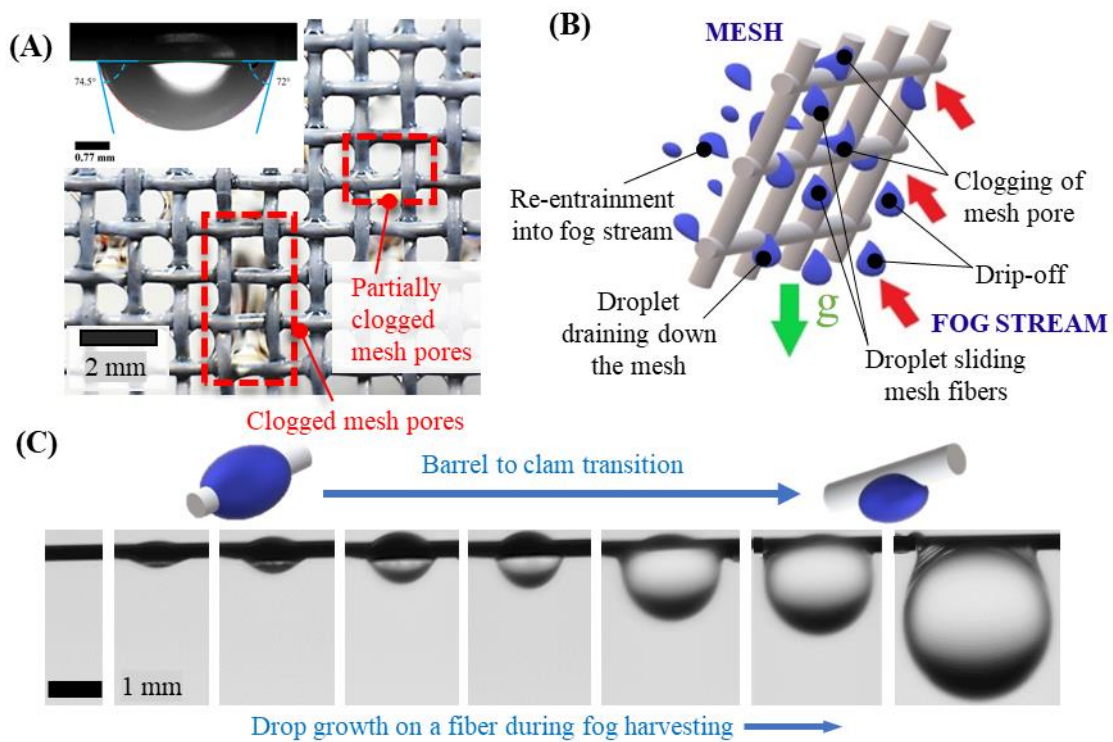


Figure 3.1: (A) Traditional interweaved metal meshes are prone to clogging of mesh pores. Mesh clogging has strong dependence on the apparent contact angle of the liquid droplet on the fiber surface (inset). (B) A typical mesh arrangement in cooling tower fog harvesters showing deposited and detached droplets. (C) A growing droplet on a thin fiber can undergo dramatic morphological variations: from axisymmetric barrel shaped droplets to clamshell shapes.

As already mentioned, the wettability of the mesh fibers, represented by its apparent contact angle (θ), plays a strong role in determining the droplet morphology and whether it will clog the mesh under standard operation scenarios [130]. The droplet morphologies arising during fog harvesting is investigated, both experimentally and numerically, and the optimal design to

avoid the formation of such clogging is identified. Effects of varying fiber diameter and fiber surface wettability were also characterized to arrive at the design of *clog-proof* meshes.

3.1 Experimental

Experiments were carried out to characterize the morphology of water droplets on horizontally mounted mesh fibers through direct imaging. Fibers of three different wettability, viz., untreated fibers (control), superhydrophilic (SHPL), and hydrophobic (HPB) were chosen. For the control surfaces, stainless steel fibers (SS-304), with measured roughness (R_a) $\sim 0.29 \pm 0.11$ μm and outer diameters varying from 0.25 – 6 mm were used to mimic the fibers of a fog harvesting mesh. The fiber diameters were measured with a digital screw gauge (Yuzuki, least count of 0.001 mm). All surface roughness measurements were carried out using a contact stylus profilometer (Landtek Instruments). All the fibers were cleansed via bath sonication (PCI Analytics), first in acetone and then in distilled water for 10 minutes. Thereafter, the apparent contact angle (θ) measurements were performed using an optical goniometer (Holmarc), for sessile droplets in the clamshell shape, as depicted earlier in **Figure 3.1-A (inset)** [131, 132]. Smooth aluminum cylinders of outer diameter 2 – 6 mm and $\theta \sim 71^\circ \pm 3^\circ$ were turned SHPL by sandblasting, followed by etching in 3N hydrochloric acid (HCl) solution which creates micro-nano roughness on the surface. The SHPL surfaces were then passivated in boiling water for 30 minutes thereby creating stable hierarchical böhmite structures [133] (see **Figure 3.2-A-i**). The fibers displayed a very low θ ($< 5^\circ$) with a roughness of $R_a \sim 4.01 \pm 0.22$ μm [134]. The control fibers were turned HPB ($\theta \sim 104^\circ \pm 3^\circ$, measured roughness, $R_a \sim 0.58 \pm 0.31$ μm) by dip-coating with polydimethylsiloxane (PDMS): fibers were first ultrasonicated in acetone and water, dried and then dip-coated (NXT dip-KPM, Apex Instruments) in a PDMS solution (SYLGARD™ 184 Silicone Elastomer, Dow; premixed thoroughly with a crosslinking agent at a ratio of 10:1 by weight) at an axial draw-out velocity of 10 mm/s. The coated fibers were then cured in a hot-air convection oven at 120 °C for ~ 2 hours (see **Figure 3.2-A-ii**).

An experimental setup as shown in **Figure 3.2-B** was developed for obtaining the droplet morphology and dimensions through direct imaging. A horizontally positioned three-jaw chuck was used to firmly hold onto the wettability-engineered cylindrical fibers. A flicker-free LED-powered (LT Max, GSVitec) white screen was used as a background for all imaging purposes. Live feed from a digital camera (Nikon D7200, with Nikkor AF-SDX 50 mm lens, mounted on 12 – 36 mm extension tubes) was stored onto a computer and viewed simultaneously on a monitor during experimentation.

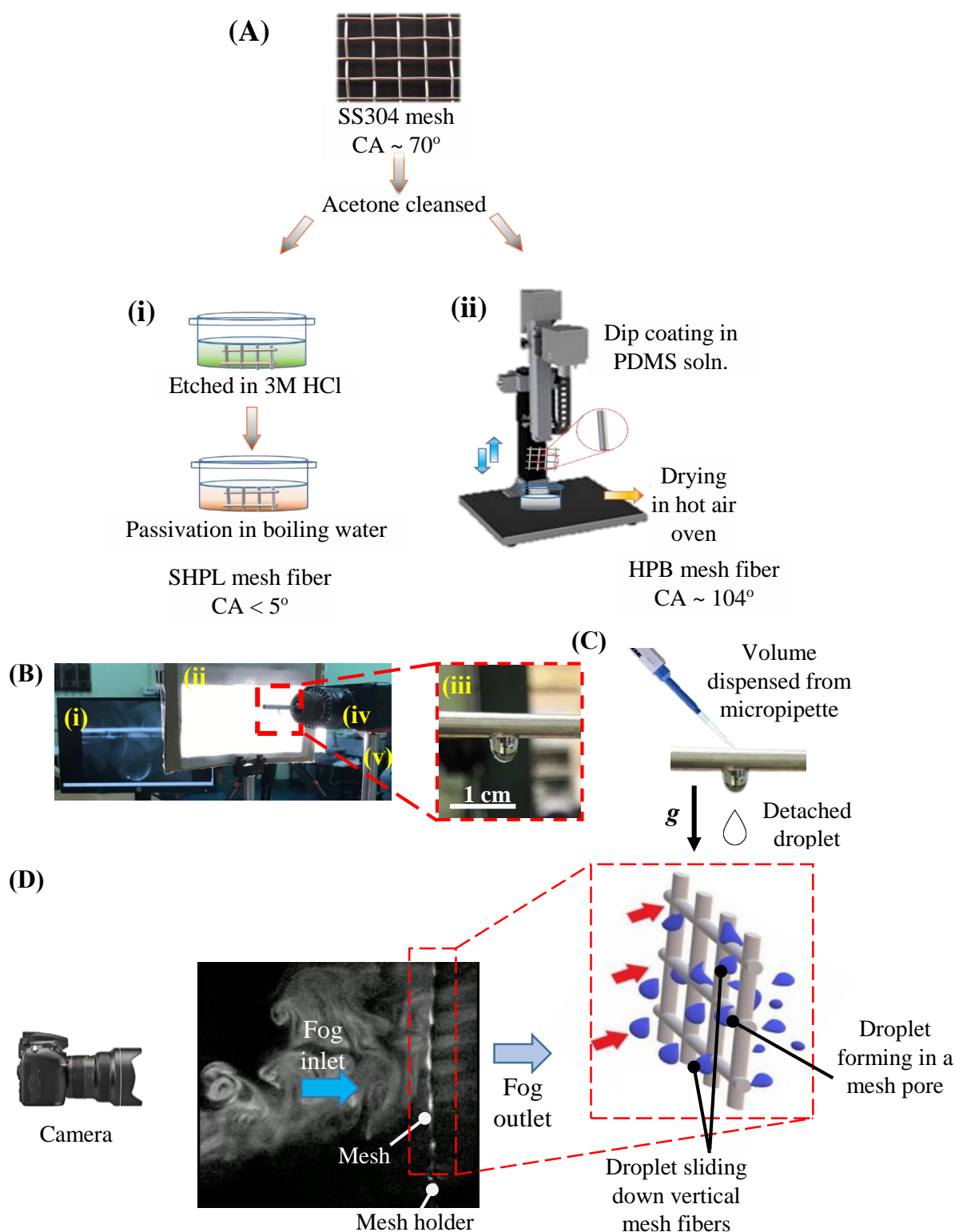


Figure 3.2 (A) Schematic of the sample preparation process: (i) to achieve superhydrophilic (SHPL) properties, the mesh fibers are etched in a 3M HCl solution followed by passivation in boiling water and (ii) to render the mesh fibers hydrophobic (HPB), they are dipped in PDMS solution followed by hot air drying in an oven. (B) Experimental setup with a computer display (i) and an illuminated white background (ii) to capture droplet morphology on a wettability-engineered metal fiber (iii, the zoomed-in section). The metal fiber was held by a horizontally placed three-way chuck (iv), which in turn was affixed to a firm stand (v). (C) Schematic of

the arrangement for droplet volume addition using a micropipette. The volume was incremented, in steps of the least dispensable volume (V_{LD}) of the micropipette, until the droplet detached at V_{CR} . (D) A vertically oriented mesh positioned orthogonally to the path of fog to observe fog deposition, droplet capture on mesh fiber and drainage.

A micropipette (Thermo Scientific) was used to gently dispense liquid volumes on top of the fibers (see **Figure 3.2-C**) in quanta of $V_{LD} = 1.0 \mu\text{L}$ (the least count of the dispenser). After each droplet had coalesced with the previously deposited droplet, images were recorded, and the process of dispensing another droplet was repeated until the accumulated droplet detached from the fiber; the corresponding volume was termed the critical volume of droplet detachment (V_{CR}). Care was taken while dispensing the droplet, such that the pipette tip did not touch the fiber – the droplets were dispensed with minimum disturbance to the fiber – to avoid any external perturbations (e.g., wind shear, vibrations, etc.) and to minimize any unwanted dynamic behavior leading to droplet detachment. This technique is in-line with previously reported approaches adopted to replicate liquid deposition from fog impingement [135, 136]. As the drops grow on the mesh fiber via coalescence, it is indeed probable that it comes in contact with neighbouring mesh fibers, forming capillary bridges with the crossed-mesh. However, as our general observations with the weaved SS mesh with control surface go (see **Figure 3.5-C-v**), such capillary bridges drain easily by gravity along the vertical fiber. Earlier studies by Shi et al. [137] and Gilet et al. [138] have also shown that vertical members in fog-capturing meshes can serve as drainage points.

To investigate fog droplet capture, coalescence, and detachment, a separate experimental setup was designed with a vertically oriented wire mesh positioned orthogonal to the fog flow, as illustrated in **Figure 3.2-D**. Observations from this setup, detailed in **Figure 3.5-C**, reveal that droplets forming in the center of mesh pores are more prone to clogging, whereas those forming near vertical fibers tend to drain downward upon contact with the nearest vertical fiber.

While the present study aims to optimize the mesh pore by drawing from droplet morphology dimensions on a horizontal member before gravimetric detachment, the capillary forces arising from the intersection of fibers [139] under different degrees of fiber wettability, intersection angle and inter-fiber spacing may be taken as a future exercise.

3.2 Simulation

Surface Evolver (SE) simulations [140] were conducted with horizontal fibers of different diameters and wettability regimes, with droplets of different volumes deposited on them. The SE simulation implicitly assumes a smooth surface for the fibers, notwithstanding their micro-

and nanoscale surface roughness features in reality. Keeping in view that surface roughness plays a key role in determining the apparent contact angle θ of water ($\gamma_{LV} = 72 \text{ mN/m}$) on a surface [141, 142], experimentally recorded θ values from goniometer measurements were used as input in the SE simulations [143, 144]. The results from the SE simulations were compared with pre-existing data from Carroll's analytical expression for barrel-to-clamshell shape transitions [145] and pre-existing data of the group [146, 147]. To further generalize the theory, the simulation results have also been compared with the experiments over a wide range of wettability for both superhydrophilic and hydrophobic fibers.

3.3 Results and Discussions

3.3.1 Barrel or clamshell shape?: Surface Evolver (SE) simulations

As per the literature, a liquid droplet on a horizontal, cylindrical fiber can assume either an axisymmetric barrel shape or an asymmetric clamshell shape (see **Figure 3.1-C**). For example, a barrel shape is energetically preferred in cases where liquid volume is high, and the sessile droplet contact angles (of the droplet on the fiber) are low. On the contrary, clamshell shapes are energetically stable at lower liquid volumes or for high sessile droplet contact angles [146]. However, in-between such regimes of absolute stability, there exist metastable regimes wherein both shapes emerge as energetically preferred. Factors like diameter and surface chemistry of the underlying fiber significantly influence the wetting properties, thereby playing a strong influence on the final droplet morphology on the fiber [148]. For example, decreasing the reduced volume ($V_R = V/(r_f)^3$, where r_f = the fiber radius and V = the volume of the fiber-attached droplet) or rendering the surface hydrophobic ($\theta > 90^\circ$) results in a “roll-up” of the barrel to clamshell shape [145, 146]. For low fiber Bond number ($Bo = \rho g r_f^2 / \gamma_{LV}$, where r_f = the fiber radius, ρ = liquid density, g = acceleration due to gravity, and γ_{LV} = surface tension at the air-water interface) scenarios, both these shapes can be energetically feasible [149]. To ascertain the regimes of droplet morphology and its dependence on V_R and θ , simulations were carried out in SE for drop-on-fiber systems for fixed r_f (corresponding to fixed fiber Bo).

From previous publications of the group [147] it has been established that within the morphological phase diagram that for V_R , θ , and r_f considered in this study, clamshell shaped droplets are only relevant for the fog harvesting scenarios. Hence, in the following sections describing the experimental observations, and in further investigations for the design of *clog-proof* meshes, the study limits the discussions only to clamshell shaped drops.

3.3.2 Estimation of maximal droplet dimensions from SE simulations

To estimate the maximal droplet dimensions during each converged simulation, images of the evolved droplet for each fiber diameter at specified wettability and droplet reduced volume were extracted from SE, and droplet height and width were measured using a Python-based image processing code. From each converged SE simulation, a side view of an evolved droplet and that of the fiber are reckoned for estimation of the droplet dimensions (H and W , as illustrated in **Figure 3.3-A**).

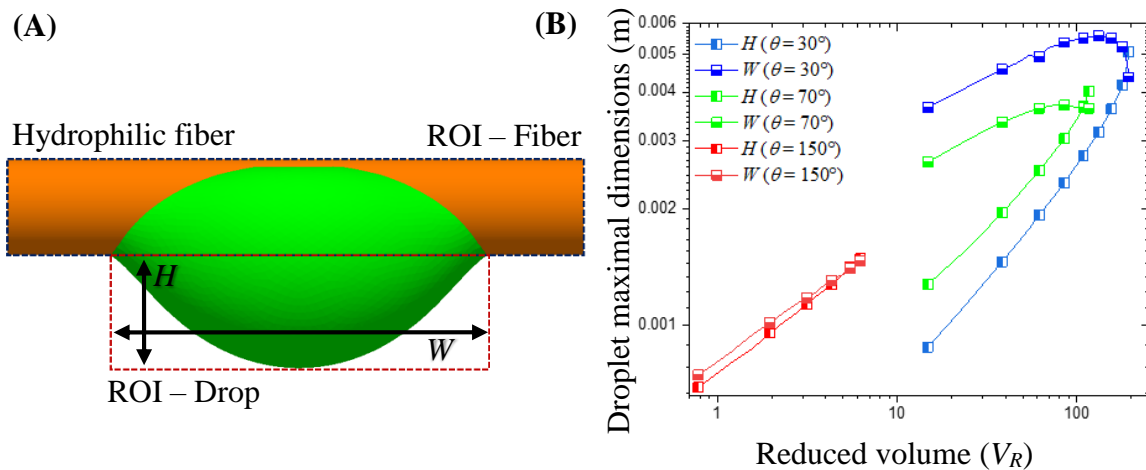


Figure 3.3: (A) Estimation of droplet dimensions via image processing in Python. Final images from the evolved surfaces were stored and later processed. ROI = Region of interest. (B) SE simulation results for variation of droplet dimension (H and W) with change of V_R until droplet detachment for a 1.27 mm diameter fiber and three different wettability levels.

For each case of fiber radius r_f and wettability (θ), simulations were run up to a limiting V_R beyond which gravitational energy was too big to produce a total energy minimum. In experiments, such situation corresponds to gravity-induced detachment of the droplet from the fiber. The values of H and W depends on the droplet shape, which in turn depends on V_R , r_f and θ .

As an example, the variation of W and H is plotted in **Figure 3.3-B** as function of V_R for three different values of θ and a fiber of diameter 1.27 mm. The largest V_R value for each plot in **Figure 3.3-B** marks the detachment volume. While it can be easily observed that the detachment volume is dependent on the fiber wettability – the curves terminate at greater V_R for a decrease in the θ – an interesting trend emerges with the resulting maximal hang (H_{max}) and width (W_{max}) of the droplet with varying V_R . As has been elucidated earlier in the main

text, these maximal droplet dimensions (for a given V_R , r_f and θ), are representative of the competition between surface-adhesion and gravitational forces.

A careful observation of **Figure 3.3-B** reveals that as the gravitational force increases (with increasing V_R), H increases irrespective of fiber wettability till the detachment (H_{max}). However, W , which represents the self-balancing surface-adhesion forces, varies based on the fiber wettability and the gravitational interaction. Therefore, W first increases, as the droplet grows, while increasingly wetting the surface, reaches a limit (W_{max}) and then starts to decrease until the droplet detaches from the fiber. Hence, from the above discussion it is essential to note that H_{max} and W_{max} are not simultaneously observed at any particular V_R , but arises from different convergent morphologies. Therefore, all H and W , recorded for a given θ over the entire range of V_R (up to the droplet detachment level) must be considered for determination of the maximum values of width (W_{max}) and height (H_{max}).

3.3.3 Experimental investigations into droplet morphology

As explained earlier, experiments were undertaken on wettability engineered fibers to evaluate droplet morphologies and to attest to the simulation results obtained from SE. A series of images to capture the droplet growth on varying fiber diameters have been provided in **Figure 3.4**. It was observed that there is significant difference in the droplet morphology for variations in fiber diameter or wettability. As is evident from Figure 4A, droplets on SHPL fibers had a greater lateral spread compared to their vertical extent, while droplets on HPB fibers had smaller contact areas. Such a morphology can be explained theoretically by taking the surface energies into consideration: SHPL fibers have greater surface energy, therefore sessile droplet geometries result in maximized contact area and vice versa. Furthermore, the extent of the droplet morphology was also limited by its critical volume of detachment (V_{CR}), wherein the droplet detached from the fiber. As the volume of the droplet is increased, the lateral extent of droplets on SHPL fibers kept on increasing till they reach a maximum, as opposed to their HPB counterparts (wherein, extension of the vertical hang is favored compared to the increase in contact area of the drop-on-fiber system).

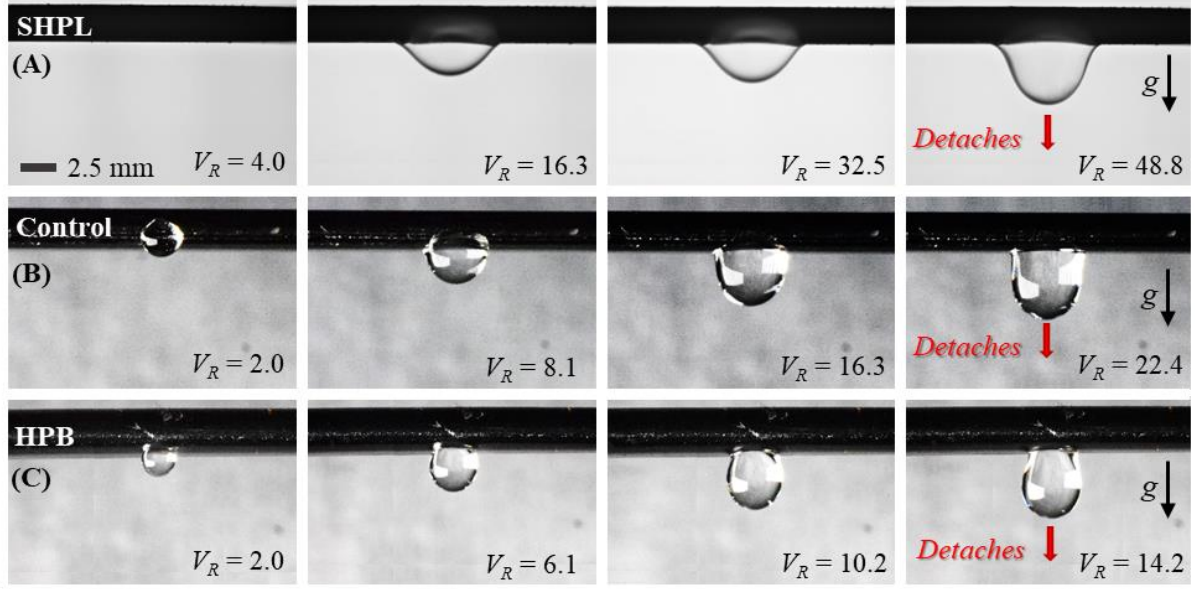


Figure 3.4: Clamshell droplet morphologies (for varying V_R) on wettability engineered fibers, as observed during experimentation. Droplets on SHPL fibers (A), were seen to spread laterally and had a greater lateral extent. Droplets on control fibers (untreated SS) showed no preference in change of lateral or vertical spread on increase of droplet volume (B), whereas droplets on HPB surfaces minimized their contact area while extending vertically with increase of volume (C). Comparisons between lateral and vertical extent of varying drop-on-fiber morphologies have been carried out in the next section. All experiments were carried out until the droplet reached the critical volume of detachment (V_{CR} , as seen in the last frame from each sequence), any volume addition after this would lead to droplet detachment. All images have the same scale bar, while each image show a fiber of diameter 2.7 mm.

The study characterizes the change of such extents by describing morphological parameters and using them to characterize *clog-proof* meshes in the following sections. Furthermore, for all the experimental trials conducted throughout this study, the control fiber ($\theta \approx 70^\circ$) diameters were varied from 0.25 mm to 6 mm, which corresponds to fiber Bo of 0.00212 and 1.22625 [123]. Again, for experiments in the super-hydrophilic regime ($\theta < 5^\circ$), surface-treated aluminum fibers had diameter variations from 2 mm to 6 mm, corresponding to Bo variations from 0.13625 to 1.22625. From earlier stability regime plots in [146], it is evident that for both these sets of experiments, barrel-shaped droplets would not be energetically preferred for any V_R . Similarly, barrel-shaped droplets for fiber radii in the order of ~ 1 mm (corresponding Bo of 0.0340), in hydrophobic regimes ($\theta > 90^\circ$) are impossible under normal gravitational ($g = 9.81 \text{ m/s}^2$) scenarios. Therefore, and as explained earlier, realistic barrel-shaped droplets do not appear both during numerical simulations and in experimental investigations of collected droplets on fog harvesting meshes, and understanding morphologies of clamshell droplets hold key in design of *clog-proof* meshes.

3.3.4 Design and characterization of “clog-proof” meshes

3.3.4.1 Droplet maximal dimension

As evident from the SE simulations and the experiments described in the previous sections (refer to **Figure 3.3-A** or **Figure 3.4**), a clamshell droplet growing on a cylindrical fiber extends its vertical hang (H) and its lateral spread (W , measured at the base or the girth of the droplet, whichever was greater), until the droplet detaches from the fiber because of its weight. These characteristic dimensions have been described in Figure 5A, wherein the consistency between the experimentally observed and simulated droplet morphology have also been demonstrated for stainless steel control (SS 304, $\theta \sim 70^\circ$) fibers of diameter 1.27 mm (top image, droplet volume 10 μL , $V_R = 39.1$) and 4 mm (bottom image, droplet volume 45 μL , $V_R = 5.6$). It is seen from **Figure 3.5-A** that the droplet hanging from the 1.27 mm fiber has $W > H$, while that from the 4 mm fiber exhibits $W < H$. It was also observed that while H kept on increasing until detachment, the lateral spread only increased up to a certain maximum (W_{max}) and then decreases as the “detachment neck” forms in the droplet. Therefore, while H_{max} occurs just prior to the detachment (i.e., $V_R = V_{CR}$), W_{max} is observed at $V_R < V_{CR}$. Such a behavior ensues from the variation of the self-adjusting surface adhesion forces with the changing droplet footprint as it attempts to balance the gravitational influence on the droplet. To examine the relative extents of H and W of a clamshell-shaped pendant droplet from the fiber, the SE simulations and experiments were further extended to describe the W and H values for different droplet-fiber θ and fiber diameters ($2r_f = 0.4, 1.27, 2.0, 4.0, 5.0$ and 6.0 mm, where r_f is the fiber radius). For SE simulations, droplet morphologies for varying $\theta = 15^\circ, 30^\circ, 70^\circ, 110^\circ$, and 160° were estimated, while for experiments the SHPL ($\theta < 5^\circ$), control ($\theta \sim 70^\circ$), and HPB ($\theta = 104^\circ$) surfaces were chosen. For both SE simulations and experiments, stable droplet morphologies and the corresponding H and W values were noted for different values of V_R – starting from zero to V_{CR} with incremental steps of V_{LD} . The largest values of W and H assumed by the droplet in the volume range ($0 \leq V_R \leq V_{CR}$) are recorded from each data set as W_{max} and H_{max} , respectively. The methodology of extracting the H_{max} and W_{max} from the SE simulation and the experimentally obtained images. These values of W_{max} and H_{max} , obtained over the entire parametric regime of θ and r_f are used to arrive at the fog harvesting mesh design criteria as described below. As shown in **Figure 3.5-B**, a droplet on the fiber of a mesh could always

interact with its neighboring fibers to form capillary bridges, which would clog the mesh pore and impact fog capture adversely.

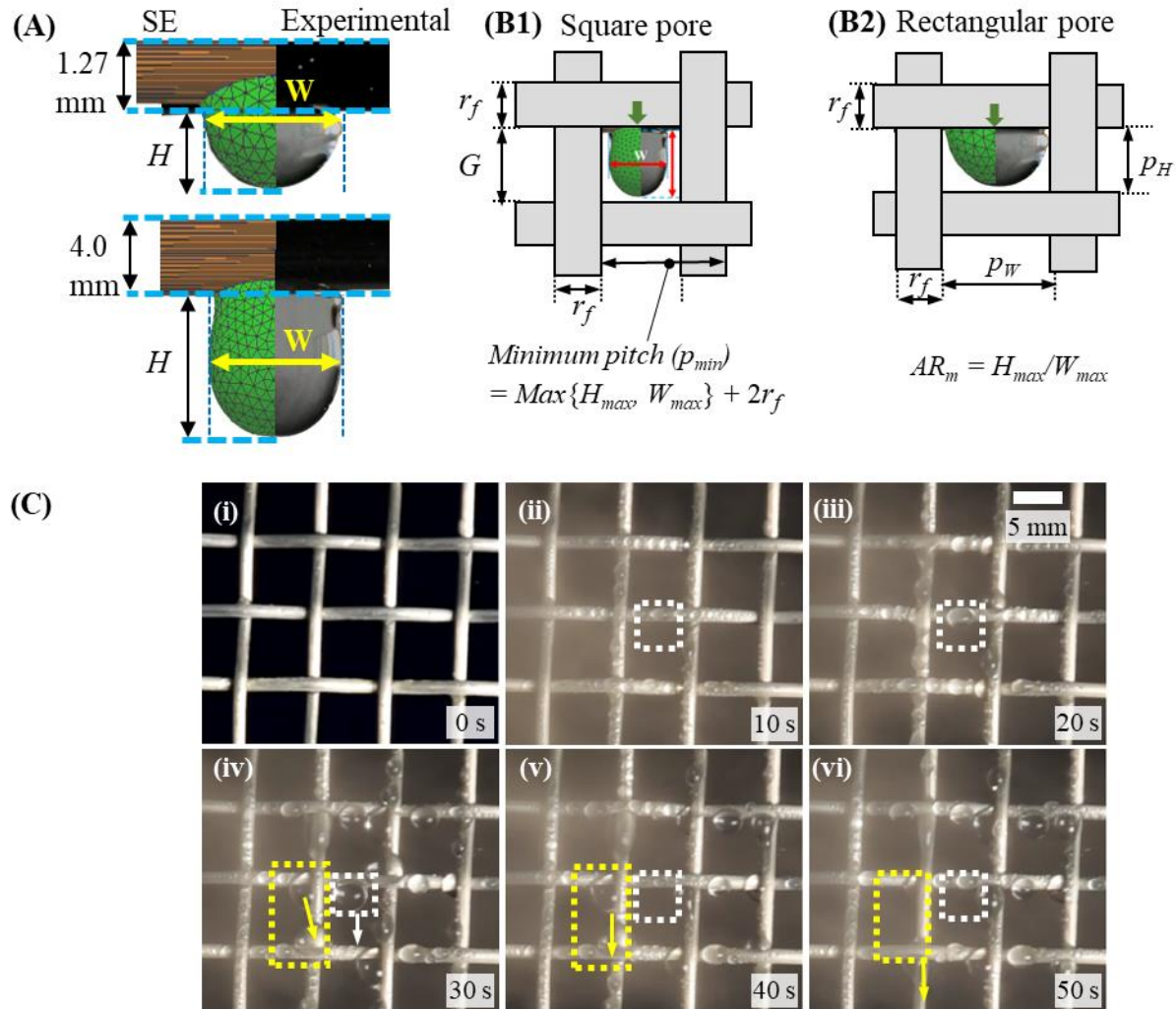


Figure 3.5: (A) Measurement of maximal width (W_{max}) and maximal vertical hang (H_{max}) in droplets hanging from 1.27 mm (top, droplet volume 10 μL) and 4 mm (bottom, droplet volume 45 μL) fibers (stainless steel 304, $\theta \sim 70^\circ$). Each figure comprises of two halves: the left half (colored in green) corresponds to SE simulations, while the other half is an experimental image. (B) Rationale for the design of *clog-proof* mesh with square pores (B1) and rectangular pores (B2): The mesh pitch should be such that a symmetrically growing droplet should not touch any other fiber, either on the side or at the bottom, as it grows until its detachment. The mesh pore dimensions, viz., the pore height and width have been marked as p_H and p_W respectively. (C) Fog droplets growing from the middle of the mesh pore have a greater probability of clogging the mesh (marked in dashed white box), while droplets near a vertical fiber (marked in dashed yellow box) can drain down after contact with the nearest vertical fiber).

Hence, for a given fiber radius of the mesh that has square-shaped pores, the pitch (distance between two fiber centerlines) needs to be greater than the maximal dimensions of the droplet spread or hang (viz., H_{max} and W_{max} respectively) to ensure that it never clogs. The underlying

assumption is that the fog-water droplet grows symmetrically from a central point marked by the green arrows in **Figure 3.5-B**. Although, in reality, fog droplets grow at multiple locations on the horizontal fiber of a mesh cell, this assumption serves the purpose without eliciting much error because of a practically observed phenomenon. It was noticed from the experiments that fog droplets growing asymmetrically, or near the corners of a mesh pore touches the nearest vertical fiber and drains down, leaving little chance of clogging the mesh pore. On the contrary, a droplet that grows from the middle of the mesh pore is at a greater risk of clogging the mesh pore as it will almost simultaneously touch vertical fibers on either side (**Figure 3.5-C**). Therefore, the study treats this configuration of fiber-attached droplet as the representative case to design clog-proof meshes.

To further generalize the design of *clog-proof* fog harvesting meshes, both square and rectangular mesh pores have been considered. It is evident from **Figure 3.5-B1** that the pitch (p) between the fibers for a square mesh is the sum of the mesh pore side (G , corresponding either of p_W or p_H for a square-pored mesh) and the fiber diameter, i.e.,

$$p = G + 2r_f \quad (3.1)$$

Once maximal droplet dimensions viz., H_{max} and W_{max} , had been evaluated for a specific combination of fiber radius and wettability, the minimum mesh pore dimensions $p_{min}(\theta, r_f)$ for a square-pore fog harvesting mesh were set equal to maximum of either H_{max} or W_{max} added to the mesh-fiber diameter, i.e.,

$$p_{min}(\theta, r_f) = \text{Max}\{H_{max}, W_{max}\} + 2r_f \quad (3.2)$$

This design approach for square-pored meshes would ensure that the droplet detaches before contacting any neighboring fibers. The maximal droplet dimension, evaluated for the first term on the right-hand side of Equation 2, is shown in Figure 6A as a function of the fiber diameter for different levels of fiber wettability as considered for SE simulations or measured (for experiments) θ .

For rectangular pore mesh designs (as previously illustrated in **Figure 3.5-B2**) the height- and width-wise dimensions, denoted as p_H and p_W , respectively, are not necessarily equal, and for designing such mesh, one should also keep in mind the aspect ratio (AR), i.e., the ratio of the height- and width-wise droplet dimensions. The AR estimated for the maximal dimensions of the droplet (for a particular fiber diameter and level of surface wettability), have been defined as the maximal aspect ratio and denoted as ($AR_m = H_{max}/W_{max}$). For a mesh with rectangular pores, the minimum value of the longer pitch (measured either height- or width-wise) should be linked with the maximal droplet dimension as

$$p_{min,longer}(\theta, r_f) = \text{Max}\{H_{max}, W_{max}\} + 2r_f, \quad (3.3a)$$

while the minimum value of the shorter pitch may be evaluated as

$$p_{min,shorter}(\theta, r_f) = \frac{\text{Max}\{H_{max}, W_{max}\}}{F} + 2r_f \quad (3.3b)$$

$$\begin{aligned} \text{where } F &= AR_m \quad \forall \{H_{max} > W_{max}\}; \\ &= 1/AR_m \quad \forall \{H_{max} < W_{max}\}; \text{ and} \\ &= 1 \quad \forall \{H_{max} = W_{max}\} \end{aligned} \quad (3.3c)$$

Therefore, for rectangular mesh design, both the droplet maximal dimension (i.e., $\text{Max}\{H_{max}, W_{max}\}$) and the droplet aspect ratio AR_m are needed to ascertain the minimum pitches in the two orthogonal directions. While the former is already available in **Figure 3.6-A**, the AR_m values have been plotted in **Figure 3.6-B** against different fiber radii and for different wettability levels. Furthermore, a series of images in **Figure 3.6-C** (taken during the experiments) show this variation of AR , at V_{CR} , for droplets on unmodified stainless steel control fibers. The maximal droplet dimension (**Figure 3.6-A**) and droplet aspect ratio (**Figure 3.6-B**) data show that both the SE simulations (filled symbols with dotted lines) and the experimental runs (half-filled circles) exhibit similar trend of variation with increasing r_f . The vertical dotted line in both the figures mark the capillary length scale of water (~ 2.7 mm). While the maximal droplet dimension (and hence the minimum mesh pitch length) is found to increase with the fiber diameter (**Figure 3.6-A**), trends in variation of AR_m are seen to be different on either side of the capillary length scale. For fiber diameters smaller than the capillary length (i.e., on the left side of the dashed line in **Figure 3.6-B**), AR_m is seen to converge near unity for a wide range of variation in wettability. This indicates that square shaped mesh pores are best suited for small fiber diameters. The final geometry of such *clog-proof* meshes would however depend on the wettability of the mesh fiber, and the *clog-proof* nature would rely on the minimum mesh pitch length as elucidated in **Equations 3.2** and **3.3**. Furthermore, for hydrophobic meshes, square mesh pores with appropriate minimum mesh pitch length appears to be *clog-proof*, since $AR_m \sim 1$ for almost all fiber diameters with $\theta = 110^\circ$ or 150° (from the SE simulations) and $\theta = 104^\circ$ (from the experimental measurements). Therefore, it is evident from **Figure 3.6-A** and **B** that the mesh-pore dimensions p_H and p_W are physical parameters entirely dependent on the drop-on-fiber morphology, the fiber diameter, and its wettability. While it is important in design of rectangular-pored *clog-proof* meshes, AR_m can also be interpreted as the ratio of the gravitational and surface-adhesion length scales acting on the droplet. A low AR_m (< 1.0) indicates greater lateral spread of the droplet throughout its growth (i.e., stronger influence of surface adhesion between the droplet

and the fiber). On the other hand, a high AR_m (> 1.0) value will imply that the droplet-fiber contact width is less, and gravitational influence is more predominant. This interpretation is further invigorated by the fact that hydrophilic fibers ($\theta < 90^\circ$) are observed to have decreasing AR_m values with increasing fiber radii. The increasing lateral spread characterized by the decreasing AR_m is prominent from the experiments and simulations involving very low θ ($< 15^\circ$).

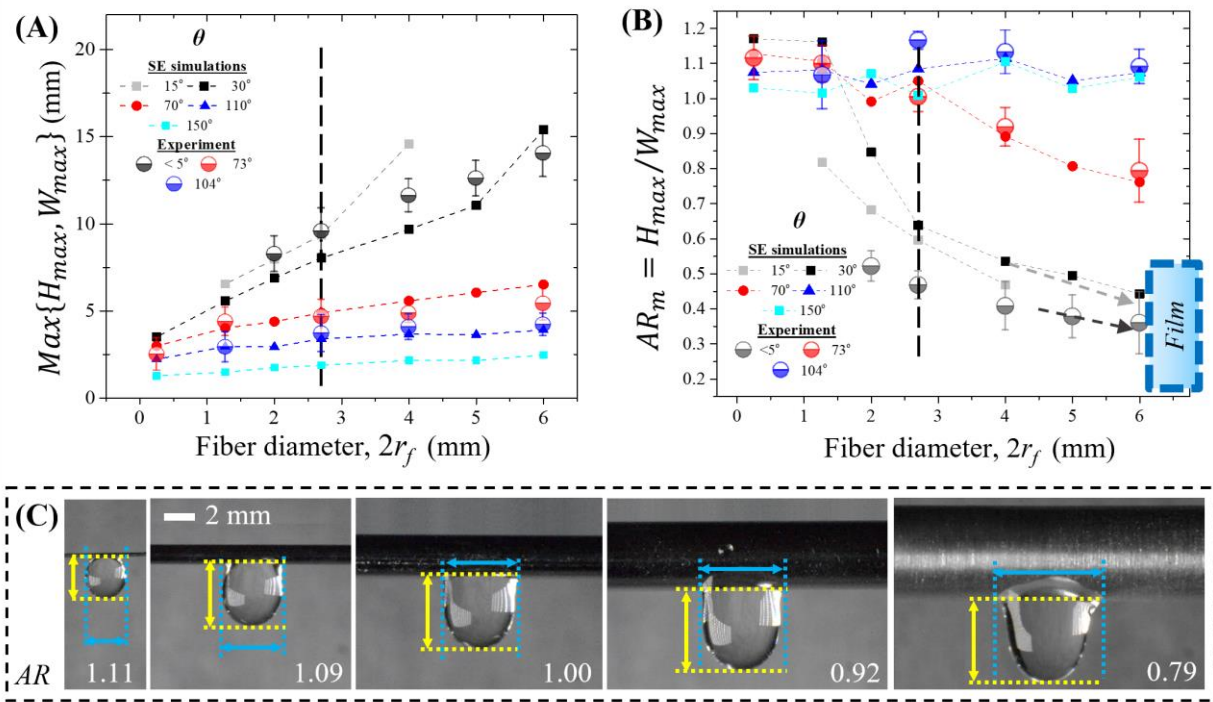


Figure 3.6: Variation of (A) the maximal droplet dimension ($Max\{H_{max}, W_{max}\}$) with the fiber radius, for the estimation of the minimum mesh pitch (as per Equation 2 or 3), and (B) the corresponding pore dimension maximal aspect ratio ($AR_m = H_{max}/W_{max}$, for the estimation of the minimum mesh pitch of a rectangular mesh as per Equation 3), plotted as functions of the fiber diameter for different mesh wettability. Legend: Filled symbols with dotted lines denote SE simulation results, half-filled circles denote the experimental data. Vertical dotted lines in both figures, mark the capillary length scale of water (~ 2.7 mm). (C) A series of experimental images showing the $AR=H/W$ calculated at the respective V_{CR} for different control fiber diameters ($\theta = 73^\circ$); H and W are marked in yellow and blue, respectively.

For such highly wettable surfaces, an increase in fiber diameter sharply increases the maximal lateral spread (thus decreasing AR_m) and the droplet eventually spreads as a film, as indicated at the bottom right corner of the plots in **Figure 3.6-B**. For SE simulations, runs with large fiber diameters (5 mm and 6 mm), did not to converge for very low θ ($< 15^\circ$), as the droplet kept on spreading, forming a liquid film on the underside of the fiber. This observation also concurred with the experiments, where the contact line could no more be observed for

superhydrophilic fibers, but the droplet would spread to form a film. The study hypothesizes that such film formation happens as capillary forces between the fiber and the droplet, at higher fiber diameter and lower θ , are sufficiently larger than gravitational forces and maximum energy minimization is obtained by assuming a film shaped morphology in place of a droplet. The present study therefore excludes this film regime, since the mesh pitch dimensions, the study intends to investigate here are in the millimetric range, which is at least an order of magnitude higher than the film thickness.

3.3.5 ‘Clog-proof’ mesh selection criteria and efficiencies

Once the droplet morphology parameters, necessary to define the geometry of *clog-proof* meshes, are determined and relevant mesh design parameters viz., r_f , p_H and p_W calculated, it becomes pertinent to evaluate the fog-collection performances of such optimally designed meshes. Furthermore, the estimation of fog harvesting mesh efficiencies require knowledge of shade coefficient, which depends on the fiber radius and the mesh pore geometry. The shade coefficient encompasses all parameters relevant to the mesh pore geometry, including the mesh pore aspect ratio (AR_m), and therefore estimation of mesh efficiencies can be carried out for all *clog-proof* meshes described herein. However, while the design criteria for both square-pore and rectangular-pore fog harvesting *clog-proof* mesh geometries have been specified earlier, only investigation of fog-capture performance of square-pored meshes have been taken up. The efficiencies of rectangular pored meshes can be evaluated in similar ways as described in the following sections.

As fog harvesting meshes intercept fog-laden wind, to collect droplets via subsequent deposition and coalescence on its fibers, it also offers a significant pressure drop to the flow. The deposited droplet eventually drains down the mesh for collection and later use. The total capture efficiency of such meshes are determined from the product of aerodynamic, deposition, and drainage efficiencies [77, 82]. The study uses the aerodynamic theory for the fog laden airflow through the mesh and the deposition dynamics of the fog droplets in the mesh that is designed for *clog-proof* operation following the minimum-pitch criteria described in the previous section. However, estimation of the drainage efficiency for such meshes is beyond the scope of the present study and may be taken up as a future exercise.

3.3.6 Aerodynamics of flow through a mesh

Fog capture meshes intercepting fog laden winds, present an interesting, but complicated flow over several bluff bodies, which causes a pressure drop across the mesh. The fluid dynamics

of such an interception via a porous blunt mesh can be considered analogous to flow across a porous media, and modeled by considering three regions of interest during the flow as depicted in **Figure 3.7-A** – *Region 1* wherein the upstream fog flow gets deflected owing to the obstruction imposed by the mesh in its path, *Region 2* denotes the location just after the net, while *Region 3* is located at the far downstream. As shown in **Figure 3.7-A**, a stream tube (denoted by the blue-dotted lines) of cross section A_1 , smaller than the area A of the fog mesh, is defined to quantify the volume flow rate of the fog-laden flow through the mesh. Following the principle of continuity, for a fog stream approaching the mesh with free-stream velocity u , it can be shown that the cross-section areas A_1 and A are related with upstream velocity, u , and velocity of the fog-stream just after interaction with the mesh, w (as depicted in **Figure 3.7-A**) as

$$A_1 u = A w \text{ or, } \frac{A_1}{A} = \frac{w}{u} = u^* \quad (3.4)$$

Here, u^* is defined as the “velocity ratio” for the given fog-flow conditions. For better estimation of the fog mesh aerodynamic efficiency, the study resorts to approximations as previously implemented by Koo [150] and Steiros [151]:

- Fog flow in region 1 is outside the stream tube encompassing the mesh and are inviscid and irrotational (potential flow approximations)
- In region 2, the fog flow follows the streamlines and is inviscid.
- Fog flow in region 3 is viscous, and characterized by significant mixing with the outer flow.
- There is significant mixing of the wake with outer flow in the interface between regions 2 and 3 which is independent of the induced velocity w .

The “fog interception ratio”, $\varphi = (A_1/A)$ (also referred in earlier studies as the “filtered fraction”) represents the fraction of the unperturbed flow reaching the mesh without getting diverted. From this, the aerodynamic efficiency (η_a , the fraction of the unperturbed oncoming flow which is directed toward the projected solid area of the mesh) can be estimated as by $\eta_a = \varphi \cdot SC$ where SC is the shade coefficient of the mesh [68]. Therefore, the aerodynamic efficiency can be expressed both as a function of the velocity ratio and the fog-interception ratio, by combining the definition of η_a with **Eq. 3.5**, such that,

$$\eta_a = \frac{w}{u} SC = u^* \cdot SC = \varphi \cdot SC \quad (3.5)$$

Therefore, for estimation of the fog-interception ratio (φ), pressure drops at the microscale (for inviscid flows through a porous substrate) are compared with the resulting pressure drop at the macroscale arising due to interaction of the fog-stream with a blunt body (herein the fog-mesh)

at higher Reynolds number [152]. This comparison leads to a direct definition of the fog-interception ratio (φ) as shown in **Eq. 3.6**,

$$\varphi = \frac{w}{u} = u^* = \frac{A_1}{A} = \sqrt{\frac{C_D}{k}} \quad (3.6)$$

where C_D and k are the drag and pressure drop coefficients arising from the fluid mechanical analysis of the problem at the macroscale and the microscale approach to the problem respectively [152]. Furthermore, such coefficients in inviscid flows through a solid blunt porous body for potential flow approximations have been extensively explored in earlier research by Koo [150] and Steiros [155]. k and C_D are directly related to the velocity ratio (u^*) and the shade coefficient (SC) as expressed in equations 3.7 and 3.8, respectively.

$$k = \left(\frac{1}{(1-SC)^2} - 1 \right) - \frac{4}{3} \frac{(1-u^*)^3}{u^{*2}(2-u^*)^2} \quad (3.7)$$

$$C_D = \frac{4}{3} \frac{(1-u^*)(2+u^*)}{(2-u^*)} \quad (3.8)$$

Using equations 5 – 8, the velocity ratio can be implicitly solved for $SC \in [0,1]$, and may be expressed as a function of the shade coefficient or, $u^* = f(SC)$, using a linear regression fit (**Eq. 3.9a**). This explicit form may, in turn, be used to estimate the aerodynamic efficiency as a function of SC in a fog harvesting mesh (**Eq. 3.9b**).

$$u^* = 1.09 - 1.05SC, \quad R^2 = 0.99 \quad (3.9a)$$

$$\eta_a = 1.09SC - 1.05SC^2 \quad (3.9b)$$

Figure 3.7-B shows the aerodynamic efficiency of square-pore fog harvesting meshes of varying fiber diameter and wettability, wherein the SC was chosen using the criteria of minimum mesh pitch $p_{min}(\theta, r_f)$ based on the maximal droplet dimensions (Figure 6A), to realize the *clog-proof* nature of the mesh. Therefore, for a given fiber diameter and wettability,

$$SC = \left[1 - \frac{2r_f}{p_{min}(\theta, r_f)} \right]^2 \quad (3.10)$$

Each curve for *clog-proof* mesh SC in **Figure 3.7-B** – drawn at a specified wettability values – divides the graph into two regions. The region upwards of each curve (i.e., at a greater SC , implying that the mesh pitch for a given fiber diameter is smaller than that obtained from **Eq. 3.3**) indicates a regions of mesh design prone to clogging. Whereas the region below the optimal SC curve implies that the mesh pitch is larger than the limit set by **Eq. 3.3**, and hence the mesh will remain clog-free. To describe the overall performance of the mesh, both in terms of its aerodynamic efficiency and ability to avoid clogging, **Figure 3.7-B** is also shaded with the color map contours of aerodynamic efficiencies, as computed from **Eq. 3.9b**. For better clarity, the aerodynamic efficiency - SC curve is also shown by the side in **Figure 3.7-B (ii)**,

wherein the aerodynamic efficiency is seen to peak ($\eta_{a,max} = 28.31\%$) at an optimum of $SC_{opt} = 0.52$. **Figure 3.7** indicates that, besides keeping the mesh design *clog-proof*, it is further possible to optimize the mesh geometry to maximize the aerodynamic efficiency close to the aforementioned value of $\eta_{a,max}$.

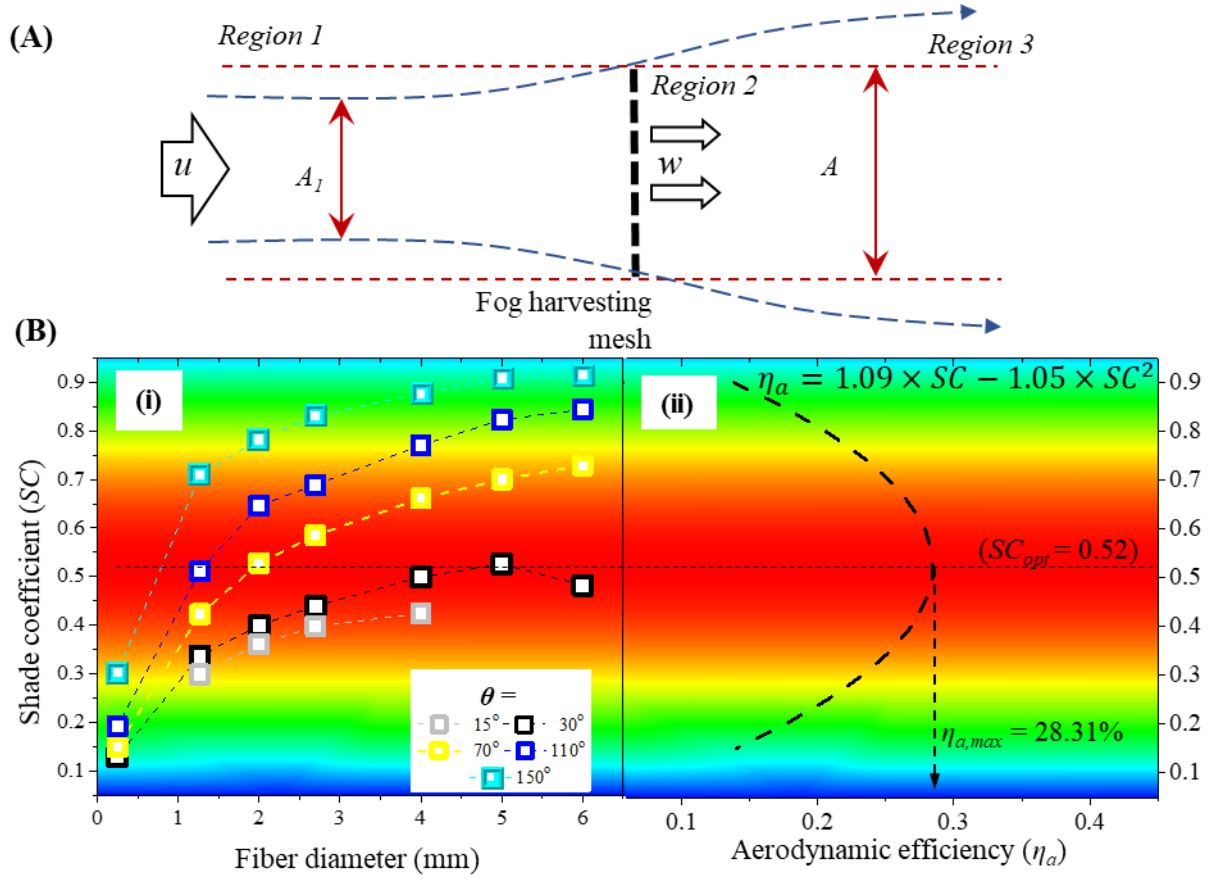


Figure 3.7: (A) Schematic of flow through a mesh placed in the path of fog laden wind (after Steiros [155]). Flow in *Region 1* deviates and goes around the mesh; fog within the upstream cross-sectional area A_I (less than the projected mesh area) interacts with the fog mesh. *Region 2* occurs just after the mesh, while *Region 3* is located at far downwind where mixing of flows from *Regions 1* and *2* occur. (B-i) Variation of the *clog-proof* SC values with the mesh fiber diameter for different fiber wettability. The *clog-proof* SC is calculated corresponding to the minimum mesh pitch lengths for square-pore fog meshes as suggested in Figure 6A. Regions above each curve (corresponding to a greater SC for a particular fiber diameter and wettability) are prone to clogging. Background color map denotes the corresponding aerodynamic efficiency as evaluated from (B-ii), which describes the variation of aerodynamic efficiency (also the black dashed curve) with the SC for square-pore fog-harvesting meshes. The color map background in (B-ii) is the same as that in (B-i), for easy comparison of η_a with *clog-proof* SC s.

This is illustrated in **Figure 3.8-A** by showing the *clog-proof* design regimes of mesh fibers of three representative wettabilities (viz., $\theta = 30^\circ$, 70° and 150°) on the SC vs fiber diameter plane. The shaded regions (cross-hatched in respective colors) below each curve designate the design regime of *clog-proof* operation, while unshaded parts above the curves denote regimes of

potential clogging. The rationale of mesh design would, therefore, be to remain within the shaded region (of the respective mesh-wettability), and have SC as close as possible to $SC_{opt} = 0.52$. It may be seen from **Figure 3.8-A** that a highly hydrophobic ($\theta=150^\circ$) mesh, which has a relatively smaller $p_{min}(\theta, r_f)$ may be designed as *clog-free* and also with $SC = SC_{opt}$ ($= 0.52$) for any fiber diameter greater than 0.8 mm. Therefore, the mesh is expected to remain clog-free and yield $\eta_{a,max} = 28.31$ % for $2r_f > 0.8$ mm. For thinner fibers (i.e., $2r_f < 0.8$ mm), the maximum allowable SC for clog-proof operation will have to be lower, and hence the efficiency will be lower than $\eta_{a,max}$. For fibers with $\theta = 70^\circ$, only meshes having $2r_f > 2.0$ mm may be designed with the optimum SC . Similarly, for a wettable mesh ($\theta = 30^\circ$), $p_{min}(\theta, r_f)$ is much larger, and only meshes having $2r_f \sim 5$ mm can be designed with $SC = SC_{opt}$.

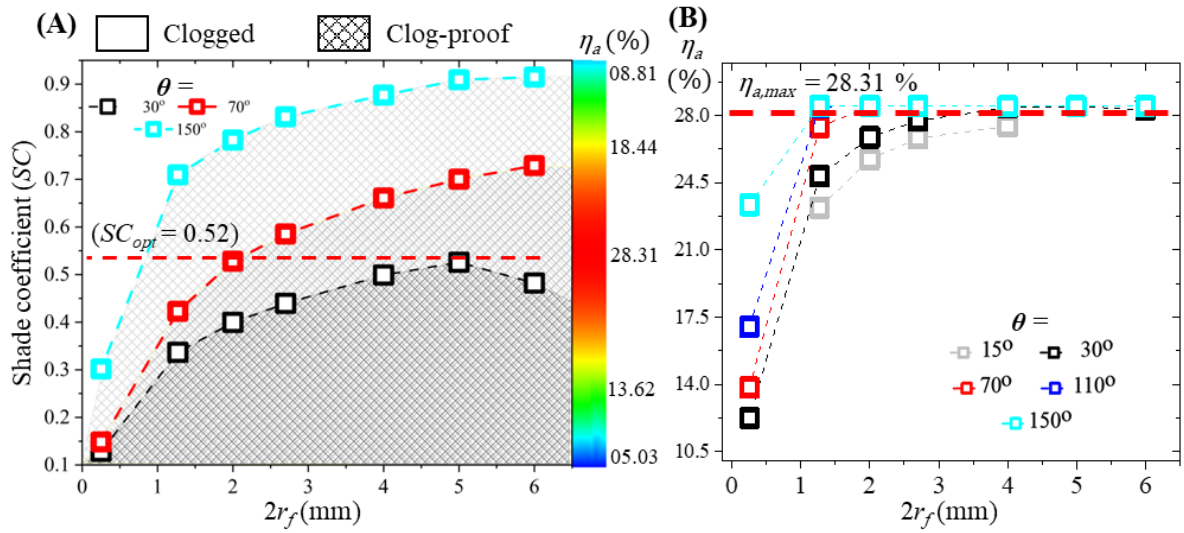


Figure 3.8: (A) Optimal shade coefficients for varying fiber diameter and wettability. The optimal mesh SC is calculated corresponding to *clog-proof* mesh pitch lengths from Figure 3.6-A. Regions above each curve (for a specific level of fiber wettability) are prone to clogging (trends with only 3 representative fiber-wettability are shown for clarity). (B) The resulting maximum achievable aerodynamic efficiency for *clog-proof* square meshes as a function of fiber diameter for different fiber wettabilities.

Therefore, the corresponding plots of maximum achievable η_a values of the clog-proof meshes of different fiber diameters and for varying levels of fiber-wettability have been shown in **Figure 3.8-B**. It is imperative from **Figure 3.8-B** that η_a increases with the fiber diameter and attains maximum η_a , beyond a certain value. It also transpires from **Figure 3.8-B** that with smaller fiber diameter meshes, it is better to have a hydrophobic mesh to maintain both the attributes of high aerodynamic efficiency and clog-proof nature. Therefore, from the results the study concludes that clog-proof meshes with lower fiber diameters results in lower aerodynamic efficiency and provides greater impedance to the flow of fog and vice versa.

Furthermore, variation of the fog-mesh fiber wettability was also seen to have a considerable impact on the design and resulting aerodynamics of *clog-proof* meshes. While it might be *wrongly* inferred here that clog proof meshes with larger fiber diameters are best suited for fog harvesting, this is not always true as the effect of deposition efficiency must be taken into consideration before commenting on the overall mesh efficiency.

3.3.7 Deposition and total efficiencies

Having established a high aerodynamic efficiency is not the only precondition of high overall capture efficiency. The fog droplets should also have a high deposition rate (and deposition efficiency) on the fiber meshes. Langmuir and Blodgett [153] in their seminal work developed a correlation for deposition of small droplets headed towards an infinitely long cylinder, thereby demonstrating the effects of the inertial and viscous forces. The capture efficiency of such a fog particle from a flow field is determined by its Stokes number (St), defined as the ratio of the characteristic time of the particle (t_p) to the characteristic time of flow (t_f) around the collector (herein, a smooth cylindrical fog-mesh fiber element). The stopping time of the particle is conventionally computed using Stokes linear drag law and in such reversible Stokesian flow regimes wherein the inertial forces are small and the particles can be assumed to be perfect solid spheres, the drag force on a fog particle can be estimated as $F_D = 6\pi R_{fog}\mu_{air}u$, where R_{fog} is the radius of the fog particle, ρ_{fog} the density of fog water, μ_{air} the dynamic viscosity and u the flow velocity of the carrier medium (herein air), respectively. For a particle moving initially with the free stream velocity, the deceleration can therefore be simply estimated from Newton's second law as

$$a = \frac{F_D}{m} = \frac{6\pi R_{fog}\mu_{air}u}{(4/3)\pi R_{fog}^3\rho_{fog}} = \frac{9\mu_{air}u}{2R_{fog}^2\rho_{fog}} \quad (3.11)$$

The characteristic stopping time (t_p) after which the fog particle gets deposited on the fiber, may be estimated by momentum balance of a fog particle, such that,

$$t_p = \frac{u}{a} = \frac{2R_{fog}^2\rho_{fog}}{9\mu_{air}} \quad (3.12)$$

The characteristic time of flow (t_f) can be defined as the ratio of the length scale of the fog flow around a mesh fiber to the velocity of the free stream ($t_f = 2r_f/u$). Plugging the values for the characteristic times, the Stokes number (St) can be represented in terms of the mesh fiber Reynolds number ($Re_{fiber} = \rho_{air}u_{slip}(2r_f)/\mu_{air}$) as

$$St = \frac{2}{9} Re_{fiber} \frac{\rho_{fog}}{\rho_{air}} \left(\frac{R_{fog}}{2r_f} \right)^2 \quad (3.13)$$

The fog droplet deposition efficiency (η_d) for millimeter sized mesh-pores can be calculated directly by using the empirical expression that is widely acceptable in the literature [154] as

$$\eta_d = \frac{St}{(\pi/2) + St} \quad (3.14)$$

However, such estimation of deposition efficiency is limited only to very low fog particle Reynolds number, defined as $Re_{fog} = 2\rho_{air}uR_{fog}/\mu_{air}$. The average fog droplet diameter ($2R_{fog}$) and has been assumed to be $\sim 5 \mu\text{m}$ throughout the remainder of this study. The estimation of deposition efficiencies at higher Re_{fog} , calls for the definition of a generalized Stokes number (St_g). Similar proposition for a generalized St had been earlier put forth by Israel and Rosner [155], to account for any non-Stokesian drag on a particle in a stream. According to the revised analysis (see **Appendix B** for the derivation), the deposition efficiency η_d may be expressed in terms of the generalized Stokes number St_g as

$$\eta_d^{-1} \cong 1 + 1.25 \left(St_g - \frac{1}{8} \right)^{-1} - 1.4 \times 10^{-2} \left(St_g - \frac{1}{8} \right)^{-2} - 0.508 \times 10^{-4} \left(St_g - \frac{1}{8} \right)^{-3} \quad (3.15)$$

for $St_g > 0.14$. Thus, for all fog deposition efficiency estimations, the study resorts to using the Israel and Rosner generalized deposition efficiency (**Eq. 3.15**) for any $St_g > 0.14$, while using the Langmuir-Blodgett [153] equations with St_g (**Eq. 3.14**) for $St_g \leq 0.14$. **Figure 3.9-A** plots the different deposition efficiencies for variations in fiber radii for different realistic sets of fog free-stream velocities ranging up to 10 m/s. A higher fog stream velocity is seen to result in a higher inertial deposition of the fog droplets, thereby leading to an increase in the deposition efficiency for all fiber diameters (**Figure 3.9-A**). However, smaller fiber diameter result in better deposition than that observed on larger ones. This may be attributed to the fact that a slender fiber gives rise to a sharper deviation of the streamlines as the flow encounters it, leading to a larger inertial effect as the particles attempt to flow past the fibers. For further characterization of overall efficiencies of the *clog-proof* meshes, a free fog stream flow velocity of 5 m/s is chosen, since it is typical in industrial cooling tower fog harvesting applications.

Reckoning the optimum shade coefficients pertaining to the maximum aerodynamic efficiency for design of *clog-proof* meshes corresponding to their wettability and fiber diameters (**Figure 3.6-B**) and the deposition efficiencies from **Figure 3.9-A** are combined to deduce the overall efficiency $\eta_d \times \eta_a$ of the *clog-proof* fog harvesters, which is reported in **Figure 3.9-B**. As can be understood from the variation of both the efficiencies, deposition efficiency plays a stronger

role and dominates to determine the final trend of the overall efficiency. Although, there is an increase in aerodynamic efficiency with increasing fiber radii (as discussed in the last section), this is not sufficient to compensate for the decrease in deposition efficiency. It is also noted that for fiber radii below ~ 2.7 mm (the capillary length-scale of water), the fog collection efficiency improves with increased hydrophobicity of the fiber, while retaining the *clog-proof* of the mesh. However, for larger mesh fiber diameter, the mesh fiber wettability is found to play very little role. This arises from the fact that the maximum achievable η_a of the *clog-proof* design of the mesh became almost insensitive to the mesh wettability for fiber diameter exceeding ~ 2.7 mm.

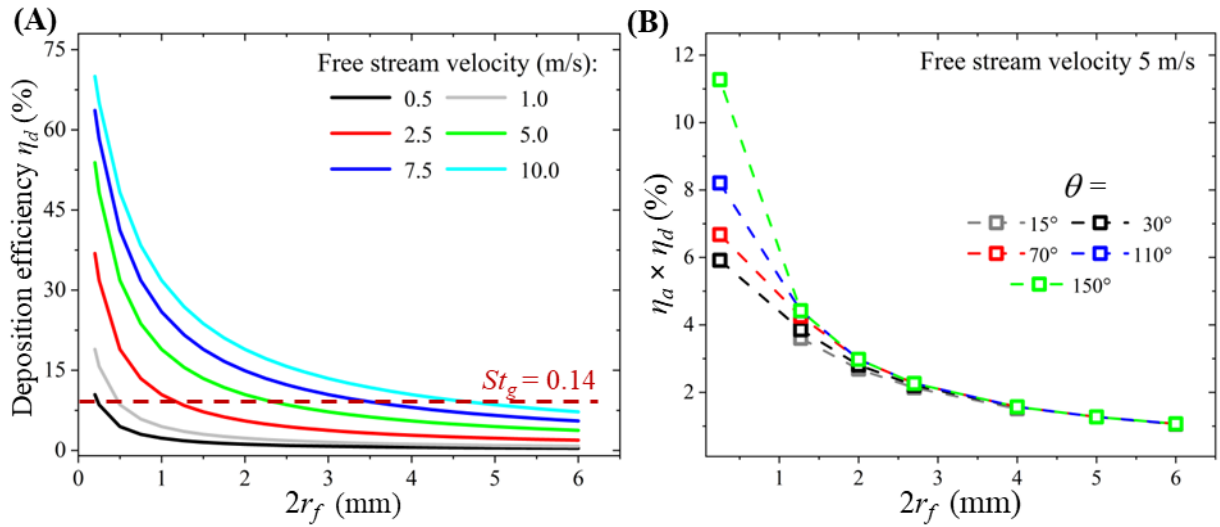


Figure 3.9: (A) Variation of deposition efficiencies (η_d) as function of fiber diameters at different fog flow velocities as evaluated from Equation 14 for $St_g \leq 0.14$ and from Equation 15 for $St_g > 0.14$. η_d resulting from $St_g = 0.14$ has been marked with a dashed red line. (B) Variation of ($\eta_d \times \eta_a$) at different optimal *clog-proof* shade coefficients for different mesh fiber diameters and wettability conditions. Total efficiencies have been estimated for a representative fog flow velocity of 5 m/s.

The study provides the basis for the design of a fog harvesting mesh that estimates the optimal mesh pitch for a combination of mesh fiber diameter and the fiber wettability to ensure clog-free operation and maximizes the overall collection efficiency.

Chapter 4

Concluding remarks

4.1 Summary of work

4.1.1 Dielectrophoretic separation of dispersed phase in air

This part of the study focuses on developing a filter that separates suspended dispersed phase in air, modelled as micrometer-sized water droplets or particulate matter (PM) using metal meshes. It attempts to strike a balance between the two cardinal challenges faced in traditional filtration technology – low deposition efficiency in sparsely woven filters and significant aerodynamic loss in denser configurations due to clogging – using a tunable dielectric filtration system.

The work introduces a novel approach involving an actively charged array of parallel metal fibers, on which a 3-phase AC is applied to influence the trajectories of droplets and particles. With variation in operating parameters like the electrode diameter and spacing, and other influencing factors, such as droplet size, gas flow velocity, voltage and frequency, the study seeks to map optimal conditions for attaining a high capture efficiency.

Key findings and characteristics of the dielectrophoretic (DEP) filter are outlined below:

- Particles of 5 μm experience larger Brownian fluctuations under the considered flow conditions, leading to stochastic capture; while the capture of larger particles is dictated through the relative importance of inertia, drag and DEP forces.
- The presence of traveling ac electric field significantly improves the occurrence of particle capture within the entire parametric plane.
- DEP capture is found to increase with the applied electric field, which may be brought about either by increasing the applied electric potential, or by decreasing the inter-electrode spacing. The influence of the latter is more, since it also increases the gradient of the electric field, thus augmenting the DEP force.
- With increased flow velocity, inertial effect of the particles gets stronger, and the effective zone of relative influence of DEP force gets more and more confined around the electrodes.
- Particle capture shows a non-monotonic behaviour with respect to changing frequency.
- The average capture efficiency for different particle size and over the entire range of operating parameters show similar behaviour when plotted in a non-dimensional time-ratio plane, viz. – the ratio of the Stokes to DEP time scales along the ordinate, and the ratio of flow-time to the AC electric field time scales along the abscissa.

- The DEP filter exhibits overall better η regime for smaller particles, a trend that is opposite to that exhibited by the traditional HEPA filters.
- The DEP capture system exhibits bands of high capture-efficiency regimes at some specific values of flow-time to the AC electric field time scale ratios. This signifies the possibility of “tuning” the operating frequency, flow velocity or electrode spacing to achieve selectively high capture efficiency.
- The fact that the DEP filters offer remarkably low pressure drop, a high Q_F , offers arc discharge-free operation, and is able to use AC power, makes it a promising contender for air-filtration in crucial healthcare environments, advanced face masks, home air filters, and even in industrial settings like oil-vapour extraction.

4.1.2 Meshes for filtering dispersed phases, particularly designed for fog harvesting:

This section of work attempts to ameliorate the problem of filter-clogging, which is often a pestering problem during filtration from a relatively dense dispersed phase, such as fog harvesting. The study reevaluates design modifications to traditional interwoven metal meshes, making them clog-resilient through passive methods. It assesses the stability of droplet morphology, which ranges from barrel to clam-shaped depending on fiber diameter and wettability, thus impacting mesh design. The present study proposes constructing mesh pores larger than the stable droplet dimensions to encourage detachment by gravity before clogging can occur. This passive design strategy is explored to enhance aerodynamic efficiency and assess the overall efficiency of the new mesh configurations in capturing dispersed phases.

Salient features of clog-resistant designs of metal meshes:

- Both simulation and experiments were conducted to observe quasi-static growth and morphology evolution of water droplets on horizontally placed fibers with different diameters and surface wettability.
- The study examined the development of a clog-free mesh design by incorporating critical droplet morphology parameters (H_{max} or W_{max}) into the geometry of fog harvesting meshes.
- Optimal minimal shade coefficients (SC) for square mesh pore fog harvesters based on the estimated minimum mesh pitch is defined.
- Hydrophobic fibers ($\theta > 90^\circ$) with diameters below the capillary length scale is shown to demonstrate superior overall efficiency in fog harvesting.

- A decrease in overall efficiency with increasing fiber diameter is noted, and is attributed to lower deposition efficiency despite a constant aerodynamic efficiency at an optimal SC of 0.52.

4.2 Future scope of work

While the present work provides a theoretical platform for characterizing DEP capture and a theoretical cum experimental approach of developing a clog-free fog harvesting mesh, several works stem from it to be undertaken for translating the current results to full-scale practical implementations.

- Further investigation is needed to explore the capture efficiency of dispersed phases at higher concentrations using dielectrophoresis, as the current study only examined very low concentrations.
- Field trials should be conducted to implement full-scale versions of filter meshes incorporating both design modifications and active dielectrophoretic filtration.
- The role of surface wettability of the electrodes on retaining dielectrophoretically captured droplets may be examined. The shape of deposited liquid is also expected to alter under the influence of the electric field, which needs to be captured through an incorporation of dielectric energy into the surface evolver simulation. Experimental investigation of the same may also be taken as a future exercise.
- In the study pertaining to fog harvesting, thin hydrophobic fibers are found perform efficiently due to high deposition efficiencies in optimal SC *clog-proof* designs. However, it is important to keep in mind that they tend to suffer from re-entrainment and premature drainage in fog harvesting applications [32]. Incorporation of drainage efficiencies and re-entrainment factors to better realize such *clog-proof* meshes, remains a future direction. Although the current study does not take into consideration the events of premature dripping and flow-induced re-entrainment, it attempts to ameliorate the occurrence of mesh clogging, which is a major component attributing to the fog harvester performance degradation during field deployment.
- While the role of the underlying surface texture (and pertinent physicochemical properties) were captured in the SE simulations by using goniometric measurements of apparent contact angles, the model did not account for contact line-pinning effects or frictional forces at the contact line [156]. Keeping in view that in realistic situations, mass-manufactured, wettability-engineered fog-harvesting meshes would entail surface

imperfections at the micro-scale and even surface impurities (e.g., oil, volatile organic compounds, chemicals, scales and dust), investigation into the role of contact-line pinning in clogging of fog harvesting meshes may be taken up as a future exercise.

- Similar exploits into wettability engineered mesh durability, reliability of performance and maintenance aspects also remain to be investigated under realistic scenarios [157, 158] to estimate the impact of ageing on the clog-free operation of the mesh.
- Also, it is worth noting that the actual metal mesh is often formed by weaving, where the gaps between the crossed mesh wires can create additional capillary effect, leading to pinning of droplets and partial clogging as shown in **Figure 3.1-A**. The present model may be extended in future to investigate the capillary forces arising from the intersection of fibers [76, 78] under different degrees of fiber wettability, intersection angle and inter-fiber spacing.

Appendix A
on
**Tunable dielectrophoretic (DEP) filters for air-
borne microdroplet capture**

A1 Validation

The model for particle transport and deposition is validated against benchmark experimental investigations of Gregory [117] and simulation results of Mirzaee et al. [118]. Both these works reported capture efficiency from a particle-laden flow by a single fiber (a typical fundamental building block of a classic filtration process). To mimic these configurations, simulation of particle capture dynamics is carried out in a two-dimensional rectangular domain with an array of fibers with large inter-fiber spacing (to avoid interference from neighbouring fibers on the particle trajectories). Following the definitions of Ref. [117] and [118], particle collection efficiency of the single-strand fiber is calculated as the ratio of the number of particles captured on the fiber to the number of particles that originally entered computational domain through an area that measures equal to the projected area of the fiber plus one particle radius on either sides at the upstream plane (inclusion of one particle-radius margin accounts for the particle-capture by interception mechanism). The particle and fiber diameters are selected to match those used in Gregory's experiments [117], and the Stokes number is varied between 0.1 and 25. For each Stokes number, 500 particles are uniformly injected from different transverse locations on the stipulated area on the inlet plane.

The simulation results for particle capture efficiency (see **Figure A1**) demonstrate very good agreement with the experimental [117] and numerical [118] data, with negligible differences in most cases instilling confidence in the simulation.

A2 Stochasticity in particle trajectory

Figure A1 depicts the stochastic behaviour of particles of two different size (viz. $d_p = 5.0$ and $50 \mu\text{m}$) released from the same transverse position at the inlet plane in a free stream velocity $U = 2.5 \text{ m/s}$. The electrode array has fiber-radius $a = 50 \mu\text{m}$ and an inter-electrode spacing $s = 2500 \mu\text{m}$; a 3-phase traveling voltage of 7 kV (producing a nominal field strength of $E_0 = 2.8 \text{ kV/mm}$) at a frequency $f = 50 \text{ Hz}$ is applied at the electrode array. In both cases, trajectories from ten repeat runs are reported. The particle trajectory shows a clear stochastic behavior due to the inherent randomness of Brownian fluctuations. Comparing the trajectories in **Figure A2-A** and **A2-B** reveals that the particle with the smaller size has a more pronounced Brownian fluctuation in its trajectory. The normalization of both the y-axis and the inter-electrode spacing, s allows for a clear comparison of particle trajectories for the two cases. This stochasticity introduces complexity to particle dynamics, significantly impacting their paths in the air stream and, consequently, the collection efficiency of the DEP filtering system.

Therefore, to ensure the statistical significance of the data, we have defined occurrence of capture, Π as per **Eq. (2.12)**.

A3 Time-averaged spatial distribution of E^2 field around the electrodes

As the dispersed droplets/particles approach the charged fiber array, they experience DEP force in the direction of the instantaneous field gradient. This DEP force directs the particle trajectories toward the electrodes, often resulting in particle interception and deposition onto the electrode surfaces. **Figure A3** provides a comparison of the time-averaged spatial distribution of the E^2 field around the electrodes – the time-averaging is performed over one complete cycle of the 3-phase travelling wave – for two inter-electrode spacing, viz., $s = 500 \mu\text{m}$ (**Figure A3-A**) and $s = 2500 \mu\text{m}$ (**Figure A3-B**). The applied voltage in both the cases corresponds to $E_o = \Phi_o/s$ of 2.8 kV/mm at a frequency of 50 Hz. For $s = 500 \mu\text{m}$ case, the reduced electrode spacing results in a notably steeper gradient of E^2 , indicating a more intense electric DEP force. This intensified force corresponds to the observed trend in particle trajectories, aligned with the observation of enhanced capture efficiency (see **Figure A4 - B1–B2** and **B3–B4**). **Figure A3** provides a visual representation of how the geometric arrangement of electrodes influences electric field dynamics, crucial for interpreting particle trajectory and capture efficiency under different operational conditions.

A4 Role of DEP forces in particle capture

Figure A3 illustrates the occurrence of capture (Π) of particles that are released from 20 individual transverse positions ($-1 \leq y/s \leq +0.9$) and inlet velocities ($U_o \in [0.5, 10]$) for different fiber radii ($a=50$ and $150 \mu\text{m}$, in subfigures A and B respectively), and particle sizes ($d_p = 5$ and $50 \mu\text{m}$), and at a constant inter-fiber spacing $s = 1500 \mu\text{m}$. The colour legend represents discrete values of Π , providing a comprehensive understanding of particle capture dynamics. The grey-shaded regions indicate flow paths obstructed by the fibers (/electrodes). **Figures A4-A1-A4** shows the values of Π mapped as functions of the transvers position of particle release in absence of electric field, while **Figure A4-B1-B4** correspond to the same in presence of a 3-phase AC voltage for which $E_o = 2.8\text{kV/mm}$. In the absence of an electric field, (**Figure A4-A**), particles are captured primarily near the electrodes due to inertial impaction, while those in and around the electrodes follow the streamlines dictated by drag forces and escapes capture. This corroborates the findings of **Figure 2.4** in the main text.

Introducing the 3-phase AC voltage (**Figure A4-B**) significantly enhances particle capture, underscoring the role of DEP forces in particle filtration systems. The traveling electric field significantly enhances particle capture across the entire parameter space (s , d_p , U). At lower U , almost all simulations show capture, indicating the dominance of the DEP force over the drag. Conversely, at higher U , particles released only near the electrode positions display high Π values, indicating that the fluidic drag and axial inertia counteract DEP capture. Comparing **Figure A4-B1–B2** (for $d_p = 5 \mu\text{m}$) and **A4-B3–B4** (for $d_p = 50 \mu\text{m}$), it transpires that for a given inter-fiber spacing ($s = 1500 \mu\text{m}$ in this case), a thicker fiber results in a stronger electric field gradient (see the discussion in section S2.0), which in turn minimizes the chance of particle escape chances.

A5 Particle capture asymmetry attributed to 3-phase voltage waveform on electrodes

Figure A4 describes the spatial distribution of Π values on the U - y/s plane for different inlet flow velocity U (0.5, 1, 2.5, 5 and 10 m/s) for $a = 50 \mu\text{m}$, $s = 2500 \mu\text{m}$ and $d_p = 10 \mu\text{m}$ under three different phase sequence of the 3-phase travelling wave. The figure sequentially advances the phase by $\frac{2\pi}{3}$ (from A through C), demonstrating the fluctuations in Π asymmetry around the electrodes. As the phase sequence changes, the spatial distribution of Π values around electrodes undergoes variations, highlighting the sensitivity of DEP capture dynamics to the temporal aspects of the electric field. A $\frac{4\pi}{3}$ phase shift results in a mirror-symmetry in the pattern of Π distribution; comparing **Figure A5-A** and **A5-C**, indicating that the pattern of Π distribution on the right electrode in **A** mirror those on the left electrode in **C** and vice versa. On the other hand, a phase shift by $\frac{2\pi}{3}$ leads to a noticeable decrease in Π values on both electrodes (see **Figure 2.4-B**). This observation underscores the influence of geometric factors and phase sequence in influencing particle capture efficiency. The influence of the phase shift in the 3-phase traveling electric field is not investigated further, and the phase depicted in **Figure 2.4-A** is adopted throughout the remainder of the study.

A6 Effect of varying operating frequency

Figure A6 provides an insight into the influence of varying the frequency of the imposed electric field on Π for different velocities ($U = 1 \text{ m/s}$ and 5 m/s). The frequency range spans from 50 Hz to 8000 Hz, corresponding to $E_0 = 2.8 \text{ kV/mm}$. This figure aligns with the observations in **Figure 2.6**, offering a broader perspective on the non-monotonic variation in

particle capture dynamics under frequency modulation. The plots illustrate Π vs y/s for diverse particle sizes with d_p varying at 5.0 μm , 10 μm , and 50 μm (illustrated in subfigure A through C respectively), emphasizing the interplay between particle diameter, free stream velocities, and the frequency of the traveling electric field.

A7 Merits of the DEP filters over the existing technology

Table A1 presents a comparison of various existing filter types, including High-Efficiency Particulate Air (HEPA), Ultra-Low Penetration Air (ULPA), N95 respirators, surgical masks, non-woven filters, cotton filters, combined fabrics, and the present DEP-based tunable dielectrophoretic filter. The table includes key metrics such as filtration efficiency (η), flow velocity, pressure drop (ΔP), and the quality factor (Q_F), as defined by **Eq. 2.20**.

Notably, the DEP filter discussed in this paper exhibits an attractive combination of high filtration efficiency and low pressure drop, resulting in a superior quality factor, compared to other filters. This advantage is attributed to the sparse arrangement of fibers ($s/a \geq 10$). The filter's tunability and compatibility with AC power position it as a promising solution in critical applications, ranging from healthcare environments to advanced face masks and industrial uses like oil-vapour extraction. The reported performance range acknowledges variations observed in the filter's filtration efficiencies across diverse operating conditions.

Table A1: Comparison of filtration efficiency, pressure drop across the filters and their respective quality factor

Filter type	η (%)	Velocity (cm/s)	ΔP (Pa)	Quality factor (Q_F)	Ref.
HEPA	99.97	50	245.16375	0.03308698	[159]
ULPA	99.9995	50	245.16375	0.049787428	[160, 161, 162]
N95 respirators	97	26	53.936025	0.06501328	
Surgical masks	82	26	21.966672	0.078063642	
Non-woven	73	26	10.6891395	0.122491929	
Cotton	32	26	55.6031385	0.006935984	
Combined fabrics	80	26	37.26489	0.043189123	
Current study*	76-100	50	4.53 - 1.90×10^{-2}	14 - 1818.89	—

*showcasing data for filter size $s = 500 \mu\text{m}$, $a = 50 \mu\text{m}$, $d_p = 10 \mu\text{m}$ operated at a 3-phase electric field of strength 1.4kV and $f = 50\text{Hz}$.

Supplementary videos:

- Visualization of equipotential lines φ and E^2 fields of a 50 Hz 3-phase AC electric field (MP4*)
- Visualization of particle trajectory in the proposed dielectrophoretic filter (MP4*)

*<https://drive.google.com/drive/folders/1Fd9TxE01nK58dRhcxVW1jOOLGbghd2dC?usp=sharing>

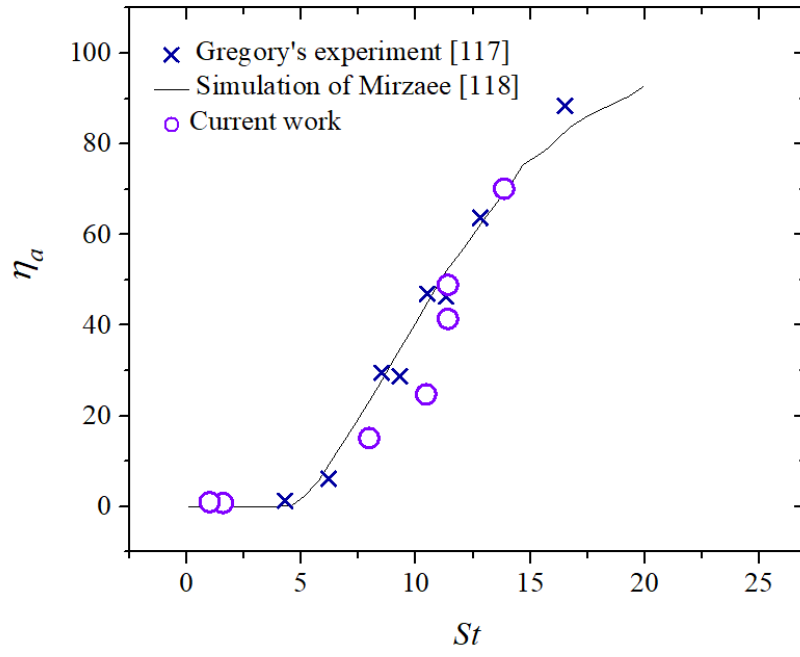


Figure A1: Validation of the current simulation with Experiments of Gregory [117] and simulations of Mirzaee [118]

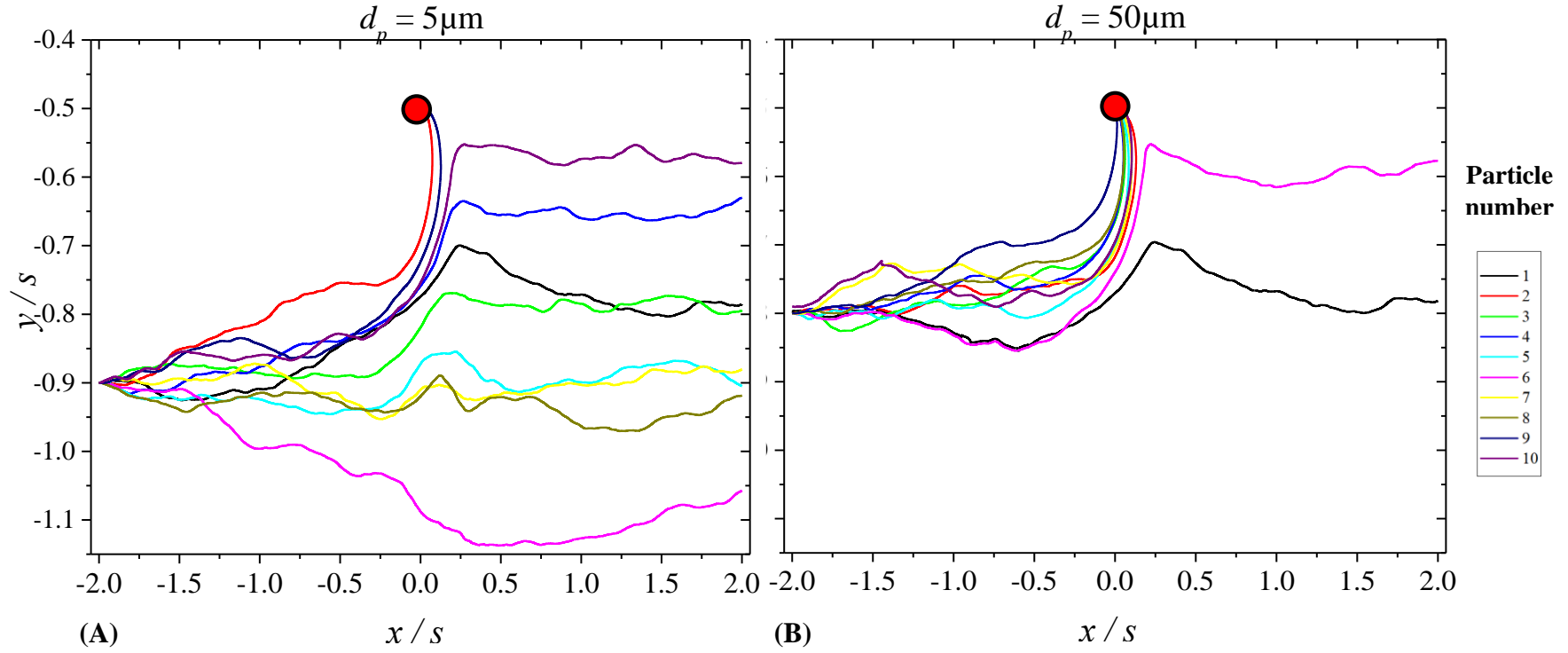


Figure A2: Extent of stochastic behavior of the particles trajectories for (A) $d_p = 5.0 \mu\text{m}$ and (B) $d_p = 50 \mu\text{m}$. For both the cases, $a = 50 \mu\text{m}$, $s = 2500 \mu\text{m}$, the 3-phase traveling-voltage $\Phi = 7 \text{ kV}$ (corresponding to $E_0 = \Phi \mathbf{o} / s = 2.8 \text{ kV/mm}$) at $f = 50 \text{ Hz}$ and the inlet flow has $U = 2.5 \text{ m/s}$. Brownian walk is prominently observable in smaller particle size. For each case, trajectories of ten identical particles, released from the same transverse position of the inlet plane are superposed.

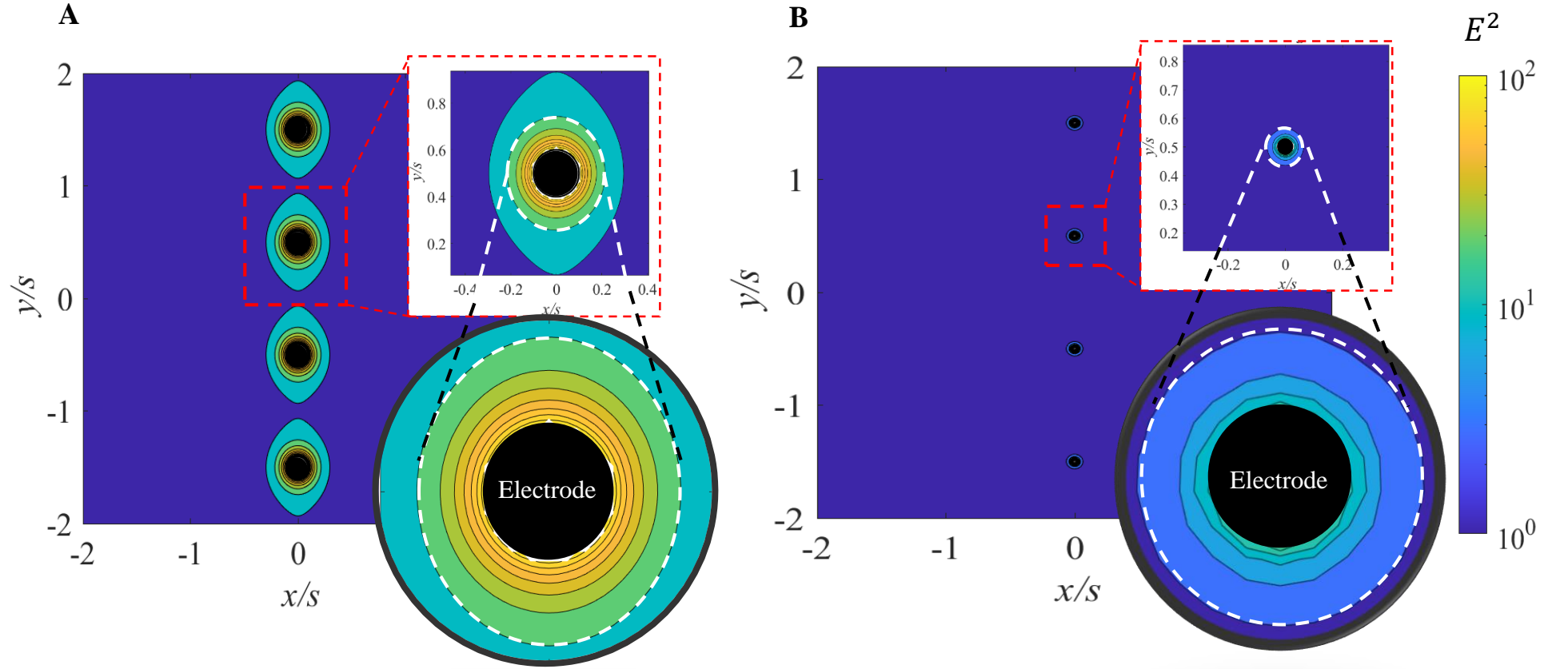


Figure A3: Comparison of the time-averaged spatial distribution of E^2 field for (A) $s = 500$ and (B) 2500 μm , averaged over the time period of the 3-phase traveling wave with $f = 50$ Hz. The applied voltage to the electrode corresponds to $E_0 = 2.8$ kV/mm.

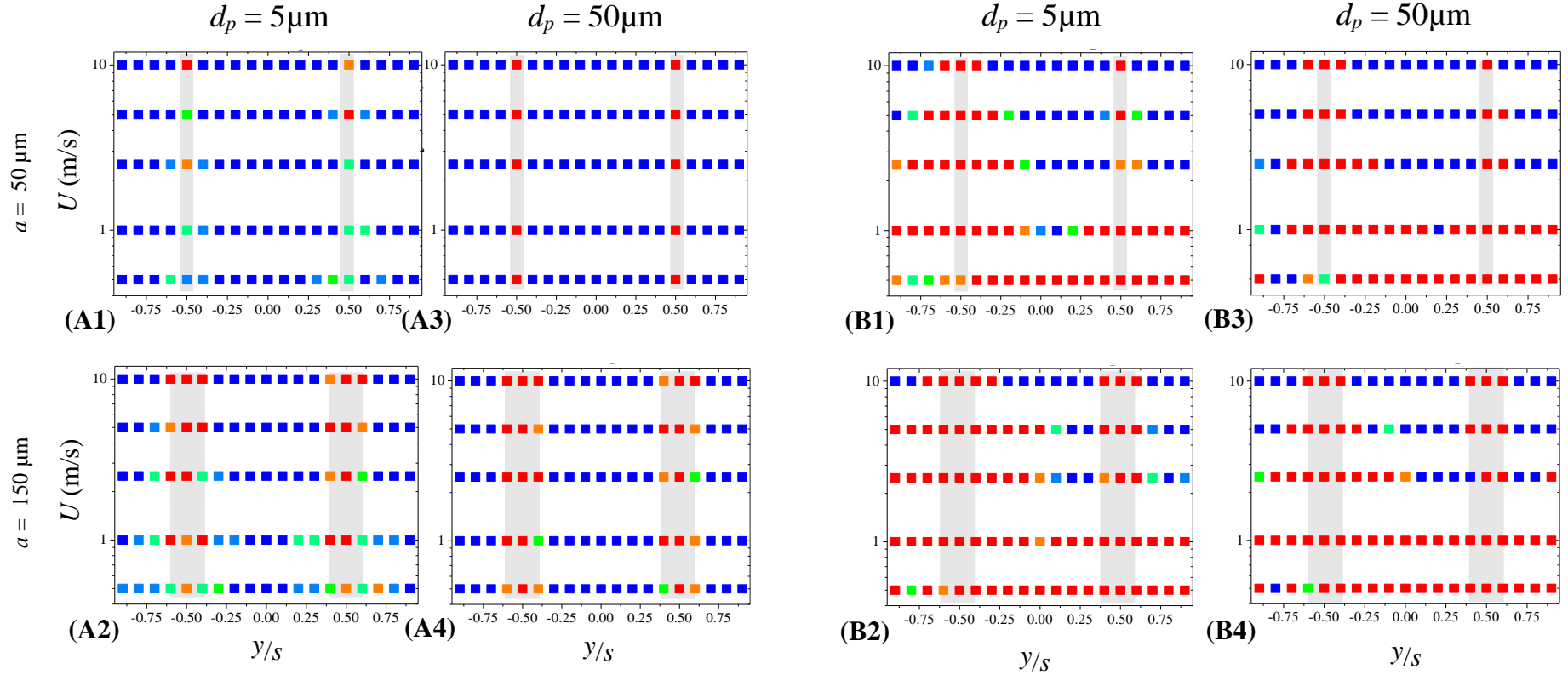


Figure A4: (A) Occurrence of capture Π mapped as functions of their transversal position of release ($-1 \leq y/s \leq +0.9$ at the inlet plane) and the inlet flow velocity U (0.5, 1, 2.5, 5 and 10 m/s), in absence of any electric field, for a constant fiber spacing $s = 1500 \mu\text{m}$. Fiber radius and particle size are varied as $a = 50 \mu\text{m}$ (A1, A3) and $150 \mu\text{m}$ (A2, A4) and $d_p = 5 \mu\text{m}$ (A1, A2) and $50 \mu\text{m}$ (A3, A4), respectively (B1 through B4). Identical parametric plots under the same conditions, except that a 3-phase AC voltage (at $f = 50 \text{ Hz}$) is imposed on the electrodes with nominal electric field strength $E_0 = 2.8 \text{ kV/mm}$. Each data-point represents the outcome of 5 simulations under identical set of parameters, yielding 6 discrete levels of Π . Colour legend: $\Pi = 5/5$ (red), $4/5$ (yellow), $3/5$ (green), $2/5$ (cyan), $1/5$ and 0 (shown together in blue). Grey-shaded regions indicate the obstruction in flow path by the fibers/electrodes.

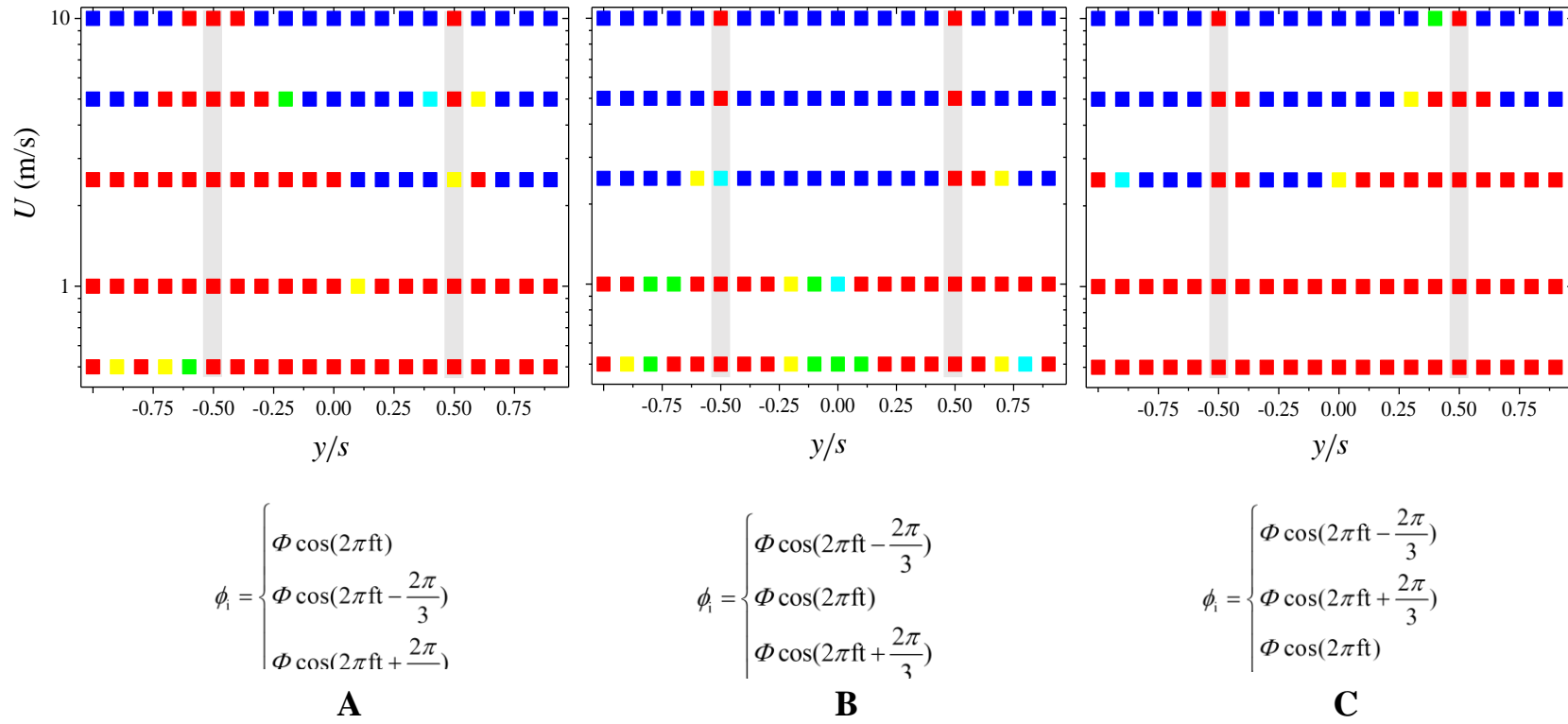


Figure A5: Spatial distribution of Π on the U - y/s plane under DEP capture, demonstrating asymmetric patterns around electrodes, influenced by electric field gradients and phase sequence in a 3-phase voltage waveform. The phase is sequentially advanced by $\frac{2\pi}{3}$ from A to C.

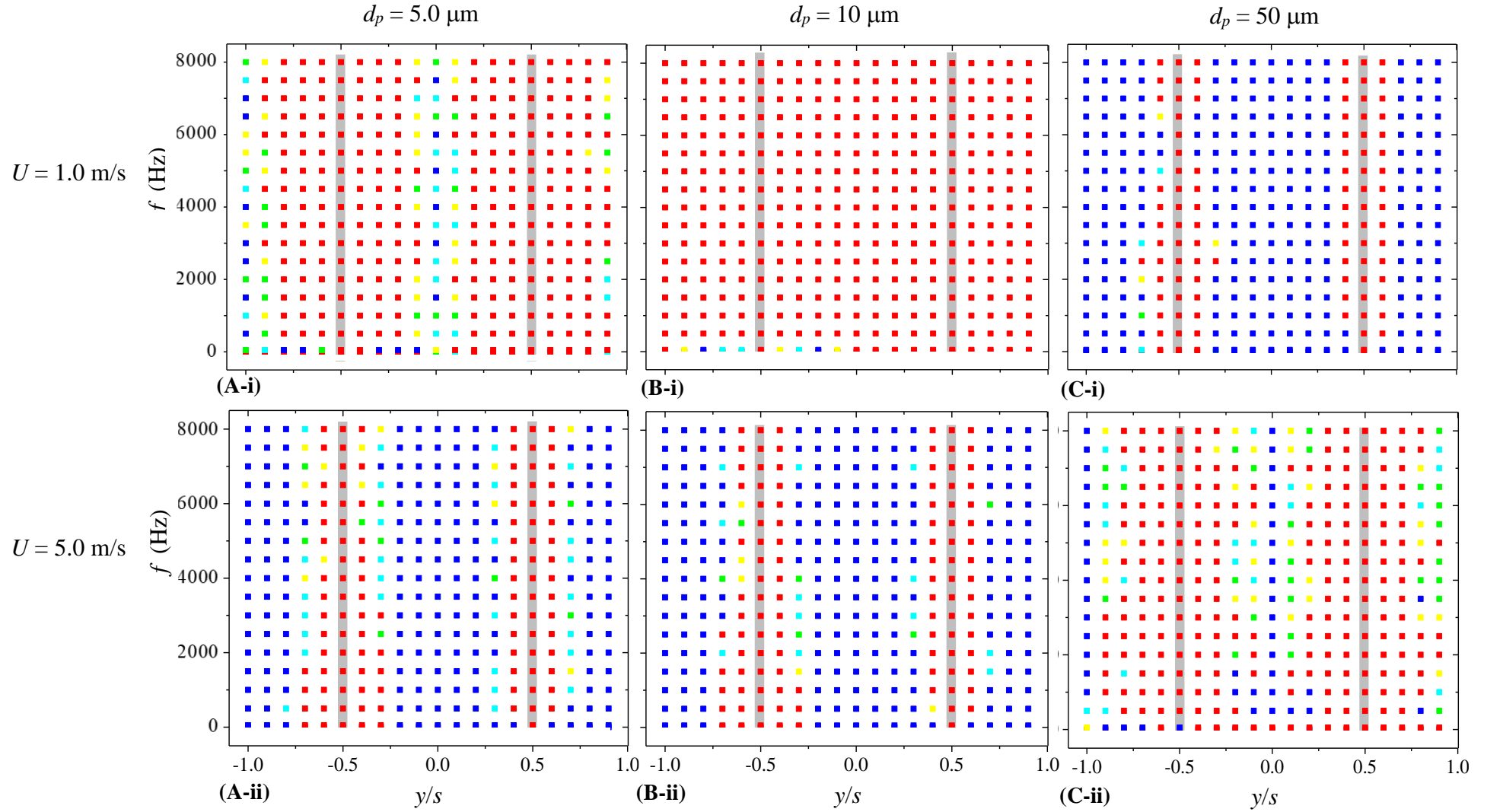


Figure A6: The impact of varying the frequency ($f \in [50, 8000]$ Hz) of the imposed electric field, corresponding to $E_0 = 2.8$ kV/mm, on Π vs y/s . The trend aligns with the non-monotonic variation in particle capture dynamics depicted in Figure 2.6, underscoring the interplay of the DEP and drag force (viz. for $U = 1$ m/s and 5 m/s). Particle sizes are varied as $d_p = 5.0$ μm (A-i - ii), $d_p = 10$ μm (B-i - ii), and $d_p = 50$ μm (C-i - ii).

Appendix B
on
**Droplet morphology-based wettability tuning and
design of fog harvesting mesh to minimize mesh-
clogging**

B1 Derivation of generalized Stokes number (St_g)

Proposition for a generalized St had been earlier put forth by Israel and Rosner [155], to account for any non-Stokesian drag on a particle in a stream. Following their derivation, the drag force on a particle moving initially with the free stream velocity can be estimated as,

$$F_D = C_{D\ fog} \frac{1}{2} \rho_{air} u^2 A_{fog} = C_{D\ fog} \frac{1}{2} \rho_{air} u^2 \cdot \left(\pi (d_{fog}/2)^2 \right) \quad (\text{A1.3})$$

Where $C_{D\ fog}$ is the coefficient of drag and A_{fog} the cross-sectional area of a fog particle, and $d_{fog} = 2R_{fog}$, is the average diameter of the fog particle. As before, the deceleration of the fog particle can be calculated similar to **Equation 3.15** (see main text) by assuming spherical fog particles, so that

$$a = \frac{F_D}{m} = \frac{C_{D\ fog} \frac{1}{2} \rho_{air} u^2 \cdot \pi R_{fog}^2}{\frac{4}{3} \pi (d_{fog}/2)^3 \rho_{fog}} = \frac{C_{D\ fog} \frac{1}{2} \rho_{air} u^2}{\frac{2}{3} d_{fog} \rho_{fog}} \quad (\text{A1.4})$$

Thereafter, assuming constant deceleration of the fog particle in the flow stream, and for a small displacement ds of the particle, it can be related to its initial droplet velocity (u) and deceleration as,

$$ds = \frac{d(u^2)}{2a} = \frac{2u(du)}{C_{D\ fog} \rho_{air} u^2} \times \frac{4}{3} R_{fog} \rho_{fog} = \frac{4}{3} \frac{\rho_{fog}}{\rho_{air}} d_{fog} \frac{du}{C_{D\ fog} u} = \frac{4}{3} \frac{\rho_{fog}}{\rho_{air}} d_{fog} \frac{dRe}{C_{D\ fog}(Re)Re} \quad (\text{A1.5})$$

Where, $C_{D\ fog}$ is a function of the fog particle Reynolds number or $C_{D\ fog} = f(Re_{fog})$. Therefore, the stopping distance (l_p) of the fog particle can be calculated by integration of the previous equation over a variation of the Reynolds number of the fog particle as it finally stops,

$$l_p = \frac{4}{3} \frac{\rho_{fog}}{\rho_{air}} d_{fog} \int_0^{Re_{fog}} \frac{dRe}{C_{D\ fog}(Re)Re} \quad (\text{A1.6})$$

Thus, a generalized Stokes number (St_g) is expressed as a ratio of the stopping distance (l_p) to the fog mesh cylinder radius ($2R_{fiber} = D_{fiber}$).

$$St_g = \frac{l_p}{R_{fiber}} = \frac{8}{3} \frac{\rho_{fog}}{\rho_{air}} \frac{d_{fog}}{D_{fiber}} \int_0^{Re_{fog}} \frac{dRe}{C_{D\ fog}(Re)Re} \quad (\text{A1.7})$$

This generalized Stokes number (St_g) can thereafter be correlated with the conventional definition of Stokes number (St),

$$St_g = \frac{8}{3} \frac{\rho_{fog}}{\rho_{air}} \frac{d_{fog}}{D_{fiber}} \int_0^{Re_{fog}} \frac{dRe}{C_{D\ fog}(Re)Re} = \frac{\rho_{fog} d_{fog}^2}{18 \mu_{air}} \cdot \frac{u}{R_{fiber}} \left[\frac{24 \mu}{\rho_{air} u d_{fog}} \int_0^{Re_{fog}} \frac{dRe}{C_{D\ fog}(Re)Re} \right] = \psi(Re_{fog}) St \quad (\text{A1.8a})$$

where

$$\psi(Re_{fog}) = \frac{24}{Re_{fog}} \int_0^{Re_{fog}} \frac{dRe}{C_{D\ fog}(Re)Re} \quad (\text{A1.8b})$$

Thus, the generalized Stokes number is found by correcting the conventional Stokes number by $\psi(Re_{fog})$ []. Herein $C_{Dfog} = f(Re_{fog})$, is a function of the fog particle Reynolds number, and can be derived for varying Re_{fog} as expressed in Equation set S1.9 [163].

$$C_{Dfog} = \frac{3}{16} + \frac{24}{Re_{fog}} \quad 0 < Re_{fog} < 0.01 \quad (\text{A1.9a})$$

$$C_{Dfog} = \frac{24}{Re_{fog}} \left[1 + 0.1315 Re_{fog}^{(0.82 - 0.05 \log_{10}(Re_{fog}))} \right] \quad 0.01 < Re_{fog} \leq 20 \quad (\text{A1.9b})$$

$$C_{Dfog} = \frac{24}{Re_{fog}} \left[1 + 0.1935 Re_{fog}^{0.6305} \right] \quad 20 \leq Re_{fog} \leq 260 \quad (\text{A1.9c})$$

Supplementary videos:

- Droplet growth and drainage in fog-harvesting scenarios in non-optimized interwoven meshes ([MP4*](#))
- Droplet growth and evolution in morphology as fog droplets coalesce and grow on a SS-304 fiber ($2r_f = 0.25$ mm, $\theta \sim 73^\circ$) until detachment; No barrel-shaped droplets were observed, as had been predicted earlier from the SE simulations in the main text; Optimizing mesh pore geometry to minimize clogging based on maximal dimensions, as calculated during such evolution of the droplet ([MP4*](#))

* <https://pubs.acs.org/doi/full/10.1021/acs.langmuir.4c00075>

References

- [1] Muhammad, S. S., Flecker, B., Leitgeb, E., & Gebhart, M. (2007). Characterization of fog attenuation in terrestrial free space optical links. *Optical engineering*, 46(6), 066001-066001.
- [2] Rothman, T., & Ledbetter, J. O. (1975). Droplet size of cooling tower fog. *Environmental Letters*, 10(3), 191-203.
- [3] Yan, C., Yan, L., Huang, Y., Wang, Q., Morawska, L., Zhaolin, G., Cao, J., Zhang, L., Li, B., and Wang, Y. (2019). Characterization of particle size distributions during winter haze episodes in urban air. *Atmospheric research*, 228, 55-67.
- [4] Gupta, S. K., & Elumalai, S. P. (2018). Adverse impacts of fog events during winter on fine particulate matter, CO and VOCs: a case study of a highway near Dhanbad, India. *Weather*, 73(12), 396-402.
- [5] Klemm, O., & Lin, N. H. (2016). What Causes Observed Fog Trends: Air Quality or Climate Change?, *Aerosol Air Qual. Res.*, 16, 1131–1142.
- [6] <https://www.downtoearth.org.in/news/walking-deep-into-fog-52687> [Accessed 18th April, 2024]
- [7] <https://english.jagran.com/india/fog-causes-30-increase-in-pollutants-over-14000-fatalities-recorded-every-year-due-to-bad-weather-10124741> [Accessed 18th April, 2024]
- [8] Tomasi, C., Fuzzi, S., & Kokhanovsky, A. (Eds.). (2017). *Atmospheric aerosols: life cycles and effects on air quality and climate*. John Wiley & Sons.
- [9] <https://www.oas.org/dsd/publications/unit/oea59e/ch12.htm> [Accessed 18th April, 2024]
- [10] Han, S., Kim, J., & Ko, S. H. (2021). Advances in air filtration technologies: Structure-based and interaction-based approaches. *Materials Today Advances*, 9, 100134.
- [11] Dubey, S., Rohra, H., & Taneja, A. (2021). Assessing effectiveness of air purifiers (HEPA) for controlling indoor particulate pollution. *Heliyon*, 7(9).
- [12] Ogbuoji, E. A., Stephens, L., Haycraft, A., Wooldridge, E., & Escobar, I. C. (2022). Non-Solvent Induced Phase Separation (NIPS) for Fabricating High Filtration Efficiency (FE) Polymeric Membranes for Face Mask and Air Filtration Applications. *Membranes*, 12(7), 637.
- [13] Babaahmadi, V., Amid, H., Naeimirad, M., & Ramakrishna, S. (2021). Biodegradable and multifunctional surgical face masks: A brief review on demands during COVID-19 pandemic, recent developments, and future perspectives. *Science of the Total Environment*, 798, 149233.
- [14] Brown, R. C. (1984). A many-fibre model of airflow through a fibrous filter. *Journal of aerosol science*, 15(5), 583-593.

- [15] Ghatak, B., Banerjee, S., Ali, S. B., Bandyopadhyay, R., Das, N., Mandal, D., & Tudu, B. (2021). Design of a self-powered triboelectric face mask. *Nano Energy*, 79, 105387.
- [16] Arya, R., Ahlawat, S., Yadav, L., Jangirh, R., Mondal, A., Sharma, S. K., ... & Mandal, T. K. (2022). Particle size distribution from municipal solid waste burning over National Capital Territory, India. *Environmental Sciences Proceedings*, 19(1), 26.
- [17] Gupta, R. K., Majumdar, D., Trivedi, J. V., & Bhanarkar, A. D. (2012). Particulate matter and elemental emissions from a cement kiln. *Fuel processing technology*, 104, 343-351.
- [18] Sosnowski, T. R. (2021). Inhaled aerosols: Their role in COVID-19 transmission, including biophysical interactions in the lungs. *Current opinion in colloid & interface science*, 54, 101451.
- [19] Khan, J. Z., Sun, L., Tian, Y., Dai, Q., Hu, T., & Feng, Y. (2021). Size Distribution of Ambient Particulate Matter and Its Constituent Chemical Species Involving Saccharides During Early Summer in a Chinese Megacity. *Frontiers in Environmental Science*, 9, 659329.
- [20] Jayakantha, D. R., Bandara, H. M. N., Gunawardana, N. M., Rajapakse, R. J., Thilakarathne, D. S., Comini, E., ... & Karunarathne, S. M. M. L. (2022). Design and construction of a low cost air purifier for killing harmful airborne microorganisms using a combination of a strong multi-directional electric-field and an ultra violet light. *HardwareX*, 11, e00279.
- [21] Ather, B., Mirza, T. M., & Edemekong, P. F. (2018). Airborne precautions.
- [22] Han, Z. Y., Weng, W. G., & Huang, Q. Y. (2013). Characterizations of particle size distribution of the droplets exhaled by sneeze. *Journal of the Royal Society Interface*, 10(88), 20130560.
- [23] Scharfman, B. E., Techet, A. H., Bush, J. W. M., & Bourouiba, L. (2016). Visualization of sneeze ejecta: steps of fluid fragmentation leading to respiratory droplets. *Experiments in Fluids*, 57(2), 1-9.
- [24] Lam, D. (2011). How the world survived the population bomb: Lessons from 50 years of extraordinary demographic history. *Demography*, 48(4), 1231-1262.
- [25] WEF Global Risks 2014 (World Economic Forum, 2014)
- [26] Gosling, S. N., & Arnell, N. W. (2016). A global assessment of the impact of climate change on water scarcity. *Climatic Change*, 134(3), 371-385.
- [27] Pachauri, R. K., & Reisinger, A. (2007). IPCC fourth assessment report. IPCC, Geneva, 2007.
- [28] <https://www.indiawaterportal.org/articles/innovation-clear-fog-water-conservation>
[Accessed on 11-05-2024]

- [29] National Research Council. (2004). Review of the desalination and water purification technology roadmap. National Academies Press.
- [30] Miller, G. W. (2006). Integrated concepts in water reuse: managing global water needs. *Desalination*, 187(1-3), 65-75.
- [31] <https://www.bbc.com/future/article/20200221-how-fog-can-solve-water-shortage-from-climate-change-in-peru> [Accessed 18th April, 2024]
- [32] Ghosh, R., Ray, T. K., & Ganguly, R. (2015). Cooling tower fog harvesting in power plants—A pilot study. *Energy*, 89, 1018-1028.
- [33] Merriam RA, Fog drip from artificial leaves in a fog wind tunnel. *Water Resource Research*, 1973; 9: 1591 – 1598.
- [34] Shuttleworth WJ. The exchange of wind-driven fog and mist between vegetation and the atmosphere. *Boundary-Layer Meteorology*, 1977; 12: 463 - 489.
- [35] Ju J, Bai H, Zheng Y, Zhao T, Fang R, Jiang L. A multi-structural and multi-functional integrated fog collection system in cactus. *Nature Communications* 2012; 3: 1247.
- [36] Hamilton, W. J., & Seely, M. K. (1976). Fog basking by the Namib Desert beetle, *Onymacris unguicularis*. *Nature*, 262(5566), 284-285.
- [37] Nørgaard T, Dacke M. Fog-basking behaviour and water collection efficiency in Namib Desert Darkling beetles. *Frontiers in Zoology* 2010.
- [38] Parker AR, Lawrence CR. Water capture by a desert beetle. *Nature* 2001; 414: 33–4.
- [39] Hamilton WJ, Seely MK. Fog basking by the Namib desert beetle, *Onymacris unguicularis*. *Nature* 1976; 5, 262-284.
- [40] Schemenauer RS, Joe PI. The collection efficiency of a massive fog collector. *Atmospheric Research* 1989; 24: 53–69.
- [41] Olivier J. Fog-water harvesting along the West Coast of South Africa: a feasibility study. *Water SA* 2004;28(4):349–60.
- [42] Abdul-Wahab, S. A., & Lea, V. (2008). Reviewing fog water collection worldwide and in Oman. *International Journal of Environmental Studies*, 65(3), 487-500.
- [43] de Dios Rivera, J., & Lopez-Garcia, D. (2015). Mechanical characteristics of Raschel mesh and their application to the design of large fog collectors. *Atmospheric research*, 151, 250-258.
- [44] Schemenauer, R. S., & Cereceda, P. (1991). Fog-water collection in arid coastal locations. *Ambio*, 303-308.
- [45] <http://www.smithsonianmag.com/innovation/this-tower-pulls-drinking-water-out-of-thin-air-180950399/> [Accessed 18th April, 2024]
- [46] Central Electricity Authority, New Delhi, Report on minimization of water requirement in coal based thermal power stations. January 2012.

- [47] <http://newatlas.com/warka-water-from-air/35721/#gallery> [Accessed 18th April, 2024]
- [48] Ghosh, R., & Ganguly, R. (2020). Fog harvesting from cooling towers using metal mesh: Effects of aerodynamic, deposition, and drainage efficiencies. *Proceedings of the Institution of Mechanical Engineers, Part A: Journal of Power and Energy*, 234(7), 994-1014.
- [49] Sanchez, A. L., Hubbard, J. A., Dellinger, J. G., & Servantes, B. L. (2013). Experimental study of electrostatic aerosol filtration at moderate filter face velocity. *Aerosol Science and Technology*, 47(6), 606-615.
- [50] Damak, M., & Varanasi, K. K. (2018). Electrostatically driven fog collection using space charge injection. *Science advances*, 4(6), eaao5323.
- [51] Uchiyama, H., & Jyumonji, M. (1995). Field experiments of an electrostatic fog-liquefier. *Journal of electrostatics*, 35(1), 133-143.
- [52] Uchiyama, H., & Jyumonji, M. (1989). Development of an electrostatic fogliquefier and its field experiments. *Japanese journal of applied physics*, 28(11R), 2319
- [53] Peng, Z., Shi, J., Xiao, X., Hong, Y., Li, X., Zhang, W., ... & Yang, Z. (2022). Self-charging electrostatic face masks leveraging triboelectrification for prolonged air filtration. *Nature communications*, 13(1), 7835.
- [54] Nguyen, V., & Yang, R. (2013). Effect of humidity and pressure on the triboelectric nanogenerator. *Nano Energy*, 2(5), 604-608.
- [55] Motyl, E., & Lowkis, B. (2006). Effect of air humidity on charge decay and lifetime of PP electret nonwovens. *Fibres Text. East. Eur*, 14(5), 39-42.
- [56] Lorenceau, É.; Clanet, C.; Quéré, D. Capturing drops with a thin fiber. *J. Colloid Interface Sci.* 2004, 279(1), 192-197.
- [57] Datta, A.; Mukhopadhyay, A.; Dutta, P. S.; Saha, A.; Datta, A.; Ganguly, R. Droplet detachment from a horizontal fiber of a fog harvesting mesh. *Fluid Mechanics and Fluid Power (Vol. 2). FMFP 2021. Lecture Notes in Mechanical Engineering*, Springer, Singapore. 2021, 485-490.
- [58] Park, K. C., Chhatre, S. S., Srinivasan, S., Cohen, R. E., & McKinley, G. H. (2013). Optimal design of permeable fiber network structures for fog harvesting. *Langmuir*, 29(43), 13269-13277.
- [59] Ghosh, R.; Patra, C.; Singh, P.; Ganguly, R.; Sahu, R. P.; Zhitomirsky, I.; Puri, I. K. Influence of metal mesh wettability on fog harvesting in industrial cooling towers. *Appl. Therm. Eng.* 2020, 181, 115963.
- [60] Gennes, P. G., Brochard-Wyart, F., & Quéré, D. (2004). Capillarity and wetting phenomena: drops, bubbles, pearls, waves (pp. 7-9). Springer New York.
- [61] Ang, B. T. W.; Zhang, J.; Lin, G. J.; Wang, H.; Lee, W. S. V.; Xue, J. Enhancing water harvesting through the cascading effect. *ACS Appl. Mater. Interfaces*. 2019, 11(30), 27464-27469.

- [62] Park, J. K.; Kim, S. Three-dimensionally structured flexible fog harvesting surfaces inspired by Namib Desert Beetles. *Micromachines*. 2019, 10(3), 201.
- [63] Raut, H. K.; Ranganath, A. S.; Baji, A.; Wood, K. L. Bio-inspired hierarchical topography for texture driven fog harvesting. *Appl. Surf. Sci.* 2019, 465, 362-368.
- [64] Zhang, L.; Wu, J.; Hedhili, M. N.; Yang, X.; Wang, P. Inkjet printing for direct micropatterning of a superhydrophobic surface: toward biomimetic fog harvesting surfaces. *J. Mater. Chem. A*. 2015, 3(6), 2844-2852.
- [65] Zhai, L.; Berg, M. C.; Cebeci, F. C.; Kim, Y.; Milwid, J. M.; Rubner, M. F.; Cohen, R. E. Patterned superhydrophobic surfaces: toward a synthetic mimic of the Namib Desert beetle. *Nano Lett.* 2006, 6(6), 1213-1217.
- [66] Ju, J.; Bai, H.; Zheng, Y.; Zhao, T.; Fang, R.; Jiang, L. A multi-structural and multi-functional integrated fog collection system in cactus. *Nat. Commun.* 2012, 3(1), 1247.
- [67] Lee, J.; So, J.; Bae, W. G.; Won, Y. The design of hydrophilic nanochannel-macrostripe fog collector: Enabling wicking-assisted vertical liquid delivery for the enhancement in fog collection efficiency. *Adv. Mater. Interfaces*. 2020, 7(11), 1902150.
- [68] de Dios Rivera, J. Aerodynamic collection efficiency of fog water collectors. *Atmos. Res.* 2011, 102(3), 335-342.
- [69] Chakrabarti, U.; Paoli, R.; Chatterjee, S.; Megaridis, C. M. Importance of body stance in fog droplet collection by the Namib desert beetle. *Biomimetics*. 2019, 4(3), 59.
- [70] Yu, Z.; Yun, F. F.; Wang, Y.; Yao, L.; Dou, S.; Liu, K.; Jiang, L.; Wang, X. Desert beetle-inspired superwetable patterned surfaces for water harvesting. *Small*. 2007, 13(36), 1701403.
- [71] Ju, J.; Xiao, K.; Yao, X.; Bai, H.; Jiang, L. Bioinspired conical copper wire with gradient wettability for continuous and efficient fog collection. *Adv. Mater.* 2013, 25(41), 5937-5942.
- [72] Breuer, C.; Cordt, C.; Hiller, B.; Geissler, A.; Biesalski, M. Using Paper as a Biomimetic Fog Harvesting Material. *Adv. Mater. Interfaces*. 2024, 2301048.
- [73] Kennedy, B. S.; Boreyko, J. B. Bio-Inspired Fog Harvesting Meshes: A Review. *Adv. Funct. Mater.* 2023, 2306162.
- [74] Fessehaye, M.; Abdul-Wahab, S. A.; Savage, M. J.; Kohler, T.; Gherezghiher, T.; Hurni, H. Fog-water collection for community use. *Renewable Sustainable Energy Rev.* 2014, 29, 52-62.
- [75] Bhushan, B. Design of water harvesting towers and projections for water collection from fog and condensation. *Philos. Trans. R. Soc., A*. 2020, 378(2167), 20190440.
- [76] Weyer, F.; Duchesne, A.; Vandewalle, N. Switching behavior of droplets crossing nodes on a fiber network. *Sci. Rep.* 2017, 7(1), 13309.

- [77] Park, J.; Lee, C.; Lee, S.; Cho, H.; Moon, M. W.; Kim, S. J. Clogged water bridges for fog harvesting. *Soft Matter*. 2021, 17(1), 136-144.
- [78] Gilet, T.; Terwagne, D.; Vandewalle, N. Droplets sliding on fibres. *Eur. Phys. J. E: Soft Matter Biol. Phys.* 2010, 31, 253-262.
- [79] Shi, W.; Anderson, M. J.; Tulkoff, J. B.; Kennedy, B. S.; Boreyko, J. B. Fog harvesting with harps. *ACS Appl. Mater. Interfaces*. 2018, 10(14), 11979-11986.
- [80] Shi, W.; van der Sloot, T. W.; Hart, B. J.; Kennedy, B. S.; Boreyko, J. B. Harps enable water harvesting under light fog conditions. *Adv. Sustainable Sys.* 2020, 4(6), 2000040.
- [81] Goswami, S.; Sidhpuria, R. M.; Khandekar, S. Effect of Droplet-Laden Fibers on Aerodynamics of Fog Collection on Vertical Fiber Arrays. *Langmuir*. 2023, 39(50), 18238-18251.
- [82] Shi, W.; De Koninck, L. H.; Hart, B. J.; Kowalski, N. G.; Fugaro, A. P.; van der Sloot, T. W.; Ott, R. S.; Kennedy, B. S.; Boreyko, J. B. Harps under heavy fog conditions: superior to meshes but prone to tangling. *ACS Appl. Mater. Interfaces*. 2020, 12(42), 48124-48132.
- [83] Hinds, W.C. and Zhu, Y., (2022). *Aerosol technology: properties, behavior, and measurement of airborne particles*. John Wiley & Sons.
- [84] Also in CDC's web site <https://blogs.cdc.gov/niosh-science-blog/2009/10/14/n95/> [Accessed on 07/09/2024]
- [85] Britten, A., 2024. Respiratory aerosol emission from oxygen face masks: Filtering and non-filtering masks measured with a manikin model show potential for reduced emissions. *Aerosol Science and Technology*, pp.1-12. doi:
- [86] Ogbuoji, E.A., Stephens, L., Haycraft, A., Wooldridge, E. and Escobar, I.C., (2022). Non-solvent induced phase separation (NIPS) for fabricating high filtration efficiency (FE) polymeric membranes for face mask and air filtration applications. *Membranes*, 12(7), p.637.
- [87] Romay, F.J., Liu, B.Y. and Chae, S.J., (1998). Experimental study of electrostatic capture mechanisms in commercial electret filters. *Aerosol Science and Technology*, 28(3), pp.224-234.
- [88] Ghatak, B., Banerjee, S., Ali, S. B., Bandyopadhyay, R., Das, N., Mandal, D., & Tudu, B. (2020). Design of a self-powered triboelectric face mask. *Nano Energy*, 105387.
- [89] Dong, M., Li, J., Shang, Y., & Li, S. (2019). Numerical investigation on deposition process of submicron particles in collision with a single cylindrical fiber. *Journal of Aerosol Science*, 129, 1-15.
- [90] Arya, R., Ahlawat, S., Yadav, L., Jangirh, R., Mondal, A., Sharma, S.K., Gurjar, B.R., Nemitz, E. and Mandal, T.K., (2022). Particle size distribution from municipal solid waste burning over National Capital Territory, India. *Environmental Sciences Proceedings*, 19(1), p.26.
- [91] Khan, J.Z., Sun, L., Tian, Y., Dai, Q., Hu, T. and Feng, Y., (2021). Size distribution of ambient particulate matter and its constituent chemical species involving saccharides

- during early summer in a Chinese megacity. *Frontiers in Environmental Science*, 9, p.659329.
- [92] Cao, Y. H., Cheung, C. S., & Yan, Z. D. (2004). Numerical Study of an Electret Filter Composed of an Array of Staggered Parallel Rectangular Split-Type Fibers. *Aerosol Science and Technology*, 38(6), 603–618.
- [93] Podgorski, A., Maißer, A., Szymanski, W. W., Jackiewicz, A., & Gradon, L. (2011). Penetration of Monodisperse, Singly Charged Nanoparticles through Polydisperse Fibrous Filters. *Aerosol Science and Technology*, 45(2), 215–233.
- [94] Vitthal, S., & Sharma, M. M. (1992). A Stokesian dynamics model for particle deposition and bridging in granular media. *Journal of Colloid and Interface Science*, 153(2), 314–336.
- [95] Rastegar, V., Ahmadi, G., & Babu, S. V. (2017). Effect of flow velocity on fiber efficiency and particle residence time during filtration of aqueous dispersions—An experimental and simulation study. *Particulate Science and Technology*, 1–10.
- [96] Jubery, T.Z., Srivastava, S.K. and Dutta, P., (2014). Dielectrophoretic separation of bioparticles in microdevices: A review. *Electrophoresis*, 35(5), pp.691-713.
- [97] Hughes, M. P. (2002). Strategies for dielectrophoretic separation in laboratory-on-a-chip systems. *Electrophoresis*, 23(16), 2569–2582.
- [98] Du, F., Hawari, A., Baune, M., & Thöming, J. (2009). Dielectrophoretically intensified cross-flow membrane filtration. *Journal of Membrane Science*, 336(1-2), 71–78.
- [99] Pesch, G.R., Du, F., Schwientek, U., Gehrmeier, C., Maurer, A., Thöming, J. and Baune, M., (2014). Recovery of submicron particles using high-throughput dielectrophoretically switchable filtration. *Separation and Purification Technology*, 132, pp.728-735.
- [100] Crowe, C., Schwarzkopf, J., Sommerfeld, M., and Tsuji, Y., (2012) *Multiphase flows with droplets and particles*. CRC press. (Vol. 906). Ž.
- [101] Stiti, M., Castanet, G., Corber, A., Alden, M. and Berrocal, E., (2022). Transition from saliva droplets to solid aerosols in the context of COVID-19 spreading. *Environmental research*, 204, p.112072.
- [102] Chrysikou, L.P. and Samara, C.A., (2009). Seasonal variation of the size distribution of urban particulate matter and associated organic pollutants in the ambient air. *Atmospheric Environment*, 43(30), pp.4557-4569
- [103] Mukherjee, A., & Agrawal, M. (2017). World air particulate matter: sources, distribution and health effects. *Environmental Chemistry Letters*, 15(2), 283–309.
- [104] O'Kelly, E., Pirog, S., Ward, J. and Clarkson, P.J., (2020). Ability of fabric face mask materials to filter ultrafine particles at coughing velocity. *BMJ open*, 10(9), p.e039424.
- [105] <https://orf.od.nih.gov/TechnicalResources/Documents/Technical%20Bulletins/22TB/H EPA% 20Air% 20Filtration% 20in% 20Cleanrooms% 20% E2% 80% 93% 20Design% 20Construction% 20and% 20Testing% 20Requirements% 20July% 202022% 20Technical% 20Bulletin 508.pdf> [Accessed on 01/01/2024]

- [106] Marshall, J. S. (2007). Particle aggregation and capture by walls in a particulate aerosol channel flow. *Journal of aerosol science*, 38(3), 333-351.
- [107] Li, S. Q., & Marshall, J. S. (2007). Discrete element simulation of micro-particle deposition on a cylindrical fiber in an array. *Journal of Aerosol Science*, 38(10), 1031-1046.
- [108] Bourouiba, L., Dehandschoewercker, E., & Bush, J. W. M. (2014). Violent expiratory events: on coughing and sneezing. *Journal of Fluid Mechanics*, 745, 537–563.
- [109] Allen, G., Sioutas, C., Koutrakis, P., Reiss, R., Lurmann, F. W., & Roberts, P. T. (1997). Evaluation of the TEOM® Method for Measurement of Ambient Particulate Mass in Urban Areas. *Journal of the Air & Waste Management Association*, 47(6), 682–689.
- [110] Bourouiba, L., (2021). The fluid dynamics of disease transmission. *Annual Review of Fluid Mechanics*, 53(1), pp.473-508.
- [111] Kazemi, B., & Darabi, J. (2018). Numerical simulation of dielectrophoretic particle separation using slanted electrodes. *Physics of Fluids*, 30(10), 102003.
- [112] Pethig, R., (2022). Protein Dielectrophoresis: A Tale of Two Clausius-Mossottis—Or Something Else?. *Micromachines*, 13(2), p.261.
- [113] Miyagi, T. (1958). Viscous Flow at Low Reynolds Numbers past an Infinite Row of Equal Circular Cylinders. *Journal of the Physical Society of Japan*, 13(5), 493–496.
- [114] Buckley, R. L., & Loyalka, S. K. (1989). Cunningham correction factor and accommodation coefficient: Interpretation of Millikan's data. *Journal of Aerosol Science*, 20(3), 347–349.
- [115] Mazo, R.M., (2008). *Brownian motion: fluctuations, dynamics, and applications* (Vol. 112). OUP Oxford.
- [116] <https://galton.uchicago.edu/~lalley/Courses/313/BrownianMotionCurrent.pdf> [Accessed on 20.08.2024]
- [117] Gregory, P. H. (1951). Deposition of air-borne Lycopodium spores on cylinders. *Annals of Applied Biology*, 38(2), 357-376.
- [118] Mirzaee, H., Rafee, R., & Ahmadi, G. (2019). Inertial impaction of particles on a circular cylinder for a wide range of Reynolds and P numbers: A comparative study. *Journal of aerosol science*, 135, 86-102.
- [119] Bulejko, P., Dohnal, M., Pospíšil, J., & Svěrák, T. (2018). Air filtration performance of symmetric polypropylene hollow-fibre membranes for nanoparticle removal. *Separation and Purification Technology*, 197, 122–128.
- [120] Podgórski, A., Bałazy, A. and Gradoń, L., (2006). Application of nanofibers to improve the filtration efficiency of the most penetrating aerosol particles in fibrous filters. *Chemical engineering science*, 61(20), pp.6804-6815.
- [121] Verbrugghe, N., & Khan, A. Z. (2023). Water harvesting through fog collectors: a review of conceptual, experimental and operational aspects. *International Journal of Low-Carbon Technologies*, 18, 392-403.

- [122] Adam, N. K. Detergent action and its relation to wetting and emulsification. *J. Soc. Dyers Colour.* 1937, 53(4), 121-129.
- [123] Eral, H. B.; de Ruiter, J.; de Ruiter, R.; Oh, J. M.; Semprebon, C.; Brinkmann, M.; Mugele, F. Drops on functional fibers: from barrels to clamshells and back. *Soft Matter.* 2011, 7(11), 5138-5143.
- [124] Carroll, B. J. The accurate measurement of contact angle, phase contact areas, drop volume, and Laplace excess pressure in drop-on-fiber systems. *J. Colloid Interface Sci.* 1976, 57(3), 488-495.
- [125] McHale, G.; Newton, M. I.; Carroll, B. J. The shape and stability of small liquid drops on fibers. *Oil Gas Sci. Technol.* 2001, 56(1), 47-54.
- [126] Saha, A.; Datta, A.; Mukhopadhyay, A.; Datta, A.; Ganguly, R. Time-Dependent Droplet Detachment Behaviour from Wettability-Engineered Fibers during Fog Harvesting. *Fluid Mechanics and Fluid Power (Vol. 5). FMFP 2022. Lecture Notes in Mechanical Engineering*, Springer, Singapore. 2024, 463-471.
- [127] Chou, T. H.; Hong, S. J.; Liang, Y. E.; Tsao, H. K.; Sheng, Y. J. Equilibrium phase diagram of drop-on-fiber: coexistent states and gravity effect. *Langmuir.* 2011, 27(7), 3685-3692.
- [128] Amrei, M. M.; Venkateshan, D. G.; D'Souza, N.; Atulasimha, J.; Tafreshi, H. V. Novel approach to measuring the droplet detachment force from fibers. *Langmuir.* 2016, 32(50), 13333-13339.
- [129] Sontag, D. S.; Saylor, J. R. An experimental study of the collection of fog droplets using a mesh fabric: Possible application to cooling towers. *J. Energy Resour. Technol.* 2016, 138(2), 024501.
- [130] Seo, D.; Lee, J.; Lee, C.; Nam, Y. The effects of surface wettability on the fog and dew moisture harvesting performance on tubular surfaces. *Sci. Rep.* 2016, 6(1), 1-11.
- [131] Mukhopadhyay, A.; Pal, A.; Sarkar, S.; Megaridis, C. M. Laser-Tuned Surface Wettability Modification and Incorporation of Aluminum Nitride (AlN) Ceramics in Thermal Management Devices. *Adv. Funct. Mater.* 2024, 2313141.
- [132] Datta, A.; Singh, V. K.; Das, C.; Halder, A.; Ghoshal, D.; Ganguly, R. Fabrication and characterization of transparent, self-cleaning glass covers for solar photovoltaic cells. *Mater. Lett.* 2020, 277, 128350.
- [133] Sarkar, S.; Roy, T.; Roy, A.; Moitra, S.; Ganguly, R.; Megaridis, C. M. Revisiting the supplementary relationship of dynamic contact angles measured by sessile-droplet and captive-bubble methods: Role of surface roughness. *J. Colloid Interface Sci.* 2021, 581, 690-697.
- [134] Das, C.; Gupta, R.; Halder, S.; Datta, A.; Ganguly, R. Filmwise condensation from humid air on a vertical superhydrophilic surface: Explicit roles of the humidity ratio difference and the degree of subcooling. *J. Heat Transfer.* 2021, 143(6), 061601.

- [135] Zhou, F.; Zhuang, D.; Lu, T.; Ding, G. Observation and modeling of droplet shape on metal fiber with gravity effect. *Int. J. Heat Mass Transfer*. 2020, 161, 120294.
- [136] Hu, H.; Lai, Z.; Hu, C. Droplet shedding characteristics on metal fibers with different wettability and inclined angles. *Int. J. Refrig.* 2023, 130, 271-277.
- [137] Shi, W., Anderson, M. J., Tulkoff, J. B., Kennedy, B. S., & Boreyko, J. B. (2018). Fog harvesting with harps. *ACS applied materials & interfaces*, 10(14), 11979-11986.
- [138] Gilet, T., Terwagne, D., & Vandewalle, N. (2009). Digital microfluidics on a wire. *Applied physics letters*, 95(1).
- [139] Aziz, H., & Tafreshi, H. V. (2019). Competing forces on a liquid bridge between parallel and orthogonal dissimilar fibers. *Soft Matter*, 15(35), 6967-6977.
- [140] Brakke, K. A. The surface evolver. *Experimental mathematics*. 1992, 1(2), 141-165.
- [141] Wenzel, R. N. Surface roughness and contact angle. *J. Phys. Chem.* 1949, 53(9), 1466-1467.
- [142] Cassie, A. B. D.; Baxter, S. Wettability of porous surfaces. *Trans. Faraday Soc.* 1944, 40, 546-551.
- [143] Gennes, P. G.; Brochard-Wyart, F.; Quéré, D. *Capillarity and wetting phenomena: drops, bubbles, pearls, waves*. Springer New York. 2004.
- [144] Sinha Mahapatra, P.; Ganguly, R.; Ghosh, A.; Chatterjee, S.; Lowrey, S.; Sommers, A. D.; Megaridis, C. M. Patterning wettability for open-surface fluidic manipulation: fundamentals and applications. *Chem. Rev.* 2022, 122(22), 16752-16801.
- [145] Carroll, B. J. Equilibrium conformations of liquid drops on thin cylinders under forces of capillarity. A theory for the roll-up process. *Langmuir*. 1986, 2(2), 248-250.
- [146] Mukhopadhyay, A., Dutta, P.S., Datta, A., Ganguly, R. "Liquid droplet morphology on the fiber of a fog harvester mesh and the droplet detachment conditions under gravity", 8th International and 47th National Conference on Fluid Mechanics and Fluid Power, Dec. 9—11, 2020, IIT Guwahati, India.
- [147] Mukhopadhyay, A., Datta, A., Dutta, P. S., Datta, A., & Ganguly, R. (2024). Droplet morphology-based wettability tuning and design of fog harvesting mesh to minimize mesh-clogging. *Langmuir*.
- [148] Sarkar, S.; Gukeh, M. J.; Roy, T.; Gaikwad, H.; Bellussi, F. M.; Moitra, S.; Megaridis, C. M. A new methodology for measuring solid/liquid interfacial energy. *J. Colloid Interface Sci.* 2023, 633, 800-807.
- [149] Berthier, J.; Brakke, K. A.; Berthier, E. *Open microfluidics*. John Wiley & Sons. 2016.
- [150] Koo, J.-K.; James, D. F. Fluid flow around and through a screen. *J. Fluid Mech.* 1973, 60(03), 513.
- [151] Steiros, K.; Hultmark, M. Drag on flat plates of arbitrary porosity. *J. Fluid Mech.* 2018, 853, R3.

- [152] Azeem, M.; Guérin, A.; Dumais, T.; Caminos, L.; Goldstein, R. E.; Pesci, A. I.; de Dios Rivera, J.; Torres, M.J.; Wiener, J.; Campos, J.L.; Dumais, J. Optimal design of multilayer fog collectors. *ACS Appl. Mater. Interfaces*. 2020, 12(6), 7736-7743.
- [153] Langmuir, I.; Blodgett, K. A mathematical investigation of water droplet trajectories (No. 5418). Army Air Forces Headquarters, Air Technical Service Command. 1946.
- [154] Shahrokhian, A.; Feng, J.; King, H. Surface morphology enhances deposition efficiency in biomimetic, wind-driven fog collection. *J. R. Soc., Interface*. 2020, 17(166), 20200038.
- [155] Israel, R.; Rosner, D. E. Use of a generalized Stokes number to determine the aerodynamic capture efficiency of non-Stokesian particles from a compressible gas flow. *Aerosol Sci. Technol.* 1982, 2(1), 45-51.
- [156] McHale, G.; Gao, N.; Wells, G. G.; Barrio-Zhang, H.; Ledesma-Aguilar, R. Friction coefficients for droplets on solids: the liquid–solid Amontons’ laws. *Langmuir*. 2022, 38(14), 4425-4433.
- [157] Showket, J.; Majumder, S.; Kumar, N.; Sett, S.; Mahapatra, P. S. Fog harvesting on micro-structured metal meshes: Effect of surface ageing. *Micro Nano Eng.* 2024, 22, 100236.
- [158] Ghosh, R.; Baut, A.; Belleri, G.; Kappl, M.; Butt, H. J.; Schutzius, T. M. Photocatalytically reactive surfaces for simultaneous water harvesting and treatment. *Nat. Sustain.* 2023, 6(12), 1663-1672.
- [159] <https://nepis.epa.gov/Exe/ZyPURL.cgi?Dockkey=P100C75V.TXT> [Accessed 18th April, 2024]
- [160] Morais, F.G., Sakano, V.K., Lima, L.N.D., Franco, M.A., Reis, D.C., Zanchetta, L.M., Jorge, F., Landulfo, E., Catalani, L.H., Barbosa, H.M. and John, V.M., (2021). Filtration efficiency of a large set of COVID-19 face masks commonly used in Brazil. *Aerosol Science and Technology*, 55(9), 1028–1041.
- [161] Morais, F. G., Sakano, V. K., Lima, L. N. D., Franco, M. A., Reis, D. C., Zanchetta, L. M., and Artaxo, P. (2021). Filtration efficiency of a large set of COVID-19 face masks commonly used in Brazil. *Aerosol science and technology*, 55(9), 1028-1041.
- [162] Konda, A., Prakash, A., Moss, G. A., Schmoldt, M., Grant, G. D., & Guha, S. (2020). Aerosol filtration efficiency of common fabrics used in respiratory cloth masks. *ACS Nano*, 14(5), 6339-6347.
- [163] Clift, R., Grace, J. R., & Weber, M. E. (2005). Bubbles, drops, and particles.


Arkadeep Datta
27/05/2024

[Home](#) > [Fluid Mechanics and Fluid Power \(Vol. 2\)](#) > Conference paper


Droplet Detachment From a Horizontal Fiber of a Fog Harvesting Mesh

| Conference paper | First Online: 09 April 2023

| pp 485–490 | [Cite this conference paper](#)



Fluid Mechanics and Fluid Power
(Vol. 2)
(FMFP 2021)

[Arkadeep Datta](#), [Arani Mukhopadhyay](#) , [Partha Sarathi Dutta](#), [Arijit Saha](#), [Amitava Datta](#) & [Ranjan Ganguly](#)

 Part of the book series: [Lecture Notes in Mechanical Engineering](#) ((LNME))

 Included in the following conference series:
[Conference on Fluid Mechanics and Fluid Power](#)

 686 Accesses  1 [Citations](#)

Abstract



Droplet detachment from a horizontal fiber of a fog harvesting mesh

Arkadeep Datta, Arani Mukhopadhyay, Partha Sarathi Dutta, Arijit Saha,
Amitava Datta and Ranjan Ganguly

Advanced Materials Research and Applications (AMRA) Laboratory,
Department of Power Engineering, Jadavpur University, Kolkata - 700106, India.

ABSTRACT

Fog capture holds promise in ameliorating the drastic freshwater crisis that is globally imminent. Metal meshes have shown promise in capturing both natural and industrial fogs, the latter primarily referring to cooling tower fog harvesting. However, there exists room for improvement of their water collection efficiency, which has been reported to be highly dependent on mesh wettability, geometry, and orientation with respect to the fog-laden wind. As fog droplets impinge and deposit on mesh fibers, they coalesce with previously deposited liquid to evolve as larger drops of different size and shape, depending on the mesh wettability and arrangement. While the primary intent of fog harvesting is to effectively drain the intercepted fog water along the mesh into a desired collector, premature drainage of the droplet is found to be detrimental to mesh performance. We investigate droplet detachment as a function of fiber diameter under real fogging scenarios. The results are compared with pre-existing droplet detachment theories and with numerical simulations using Surface Evolver. Droplet detachment volume is found to increase with the mesh-fiber diameter. It is also found that the existing theories of droplet detachment from fibers do not give reliable accuracy for detachment volume estimation under realistic fog-collection scenarios.

Keywords: Fog harvester, droplet detachment volume, drainage efficiency, fiber radius, Surface Evolver

1. INTRODUCTION

Water bodies cover a major portion of the world, but only a minuscule has freshwater suitable for consumption. In arid coastal regions that experience atmospheric fog, it can be utilized as an important source of freshwater. Strategically placed meshes in the paths of fog-laden wind can help capture and store water, which can later be used for daily utilities. However, major drawbacks of atmospheric fog collection include seasonal fluctuations in the amount of atmospheric fog as well as low collection efficiency of the meshes. Apart from the atmospheric fog, retrieving industrial fog (e.g., by capturing lost water from cooling tower plumes) can also help cut down on the freshwater dependency of thermal power plants, thereby making freshwater readily available for human consumption. Industrial fog harvesters are economically viable and do not depend on topological factors. Most cooling towers use drift eliminators to capture the egress of un-evaporated droplets larger than $\sim 40 \mu\text{m}$ [1], but huge water losses in the form of fog and mists still take place (for example, a 500 MW

power plant loses roughly $27 \text{ m}^3/\text{hour}$). Strategically placed metal meshes has been shown to greatly reduce such loss [2].

Water captured by a fog harvester depends on the interaction of fog-laden wind with the harvester mesh. A standard fog collector consists of meshes oriented perpendicular to the direction of fog flow. A fraction of the fog droplet population strikes the mesh fibers, gets deposited, coalesce to form larger droplets, which then roll down to get collected [2]. In traditional meshes, a drop will often grow large enough to clog the mesh and reduce efficiency. It is hence favorable that a drop detaches early. However, early detachment can also result in collection loss by droplet re-entrainment into the fog stream, thereby reducing harvester efficiency. Therefore, the detachment volume of a droplet from a fiber mesh is of prime importance and is one of the major factors that need to be considered for choosing the right mesh geometry.

A drop-on-fiber is ubiquitous in nature and has industrial relevance. A good example is the dew droplet on the cactus spine or spider web and the way it moves along the fiber or detaches from the fiber as it grows larger [3, 4, 5]. In recent years, nature-inspired fog harvesting mesh architectures [6] have garnered quite an interest in researchers. Traditional Raschel meshes for natural fog harvesting are developed from polyethylene and are prone to clogging and mechanical failure when subjected to high wind velocity [7]. Such traditional meshes can easily be replaced with commonly available metal meshes, which are less prone to breaking and are mass producible. Such meshes are generally produced by laying (or inter-weaving) two parallel sets of orthogonally placed fibers. A droplet forming on a vertical member (along the direction of gravity) rolls down easily and gets collected. Such a mesh design, in the form of a harp, wherein horizontal components are absent, was first proposed by Shi et al. [8]. However, in a later work they observed that such meshes would clog and perform poorly under heavy fogging scenarios due to wind-induced buckling [9]. Horizontal members are thus integral to mesh design, especially in scenarios of heavy fog and high wind velocities where mesh integrity is of prime importance for steady fog collection.

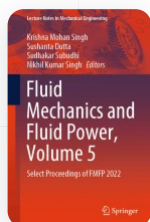
The efficiency of fog collection depends primarily on three major factors: the fraction of water content in the fog stream that may pass through the fog harvester mesh along with the undisturbed fog ($\eta_{\text{aerodynamic}}$), the fraction of water captured by the fog harvester mesh ($\eta_{\text{deposition}}$), and the fraction of water drained from the fog harvester mesh to the collector (η_{drainage});

[Home](#) > [Fluid Mechanics and Fluid Power, Volume 5](#) > Conference paper


Time-Dependent Droplet Detachment Behaviour from Wettability-Engineered Fibers during Fog Harvesting

| Conference paper | First Online: 03 March 2024

| pp 463–471 | [Cite this conference paper](#)



[Fluid Mechanics and Fluid Power,](#)
[Volume 5](#)
(FMFP 2022)

[Arijit Saha](#), [Arkadeep Datta](#) , [Arani Mukhopadhyay](#), [Amitava Datta](#) & [Ranjan Ganguly](#)

 Part of the book series: [Lecture Notes in Mechanical Engineering](#) ((LNME))

 Included in the following conference series:
[Conference on Fluid Mechanics and Fluid Power](#)

 118 Accesses  1 [Citations](#)

Abstract

Time-dependent droplet detachment behaviour from wettability-engineered fibers during fog harvesting

Arijit Saha, Arkadeep Datta, Arani Mukhopadhyay, Amitava Datta and Ranjan Ganguly¹

Advanced Materials Research and Applications (AMRA) Laboratory,
Department of Power Engineering, Jadavpur University, Kolkata – 700106, India

ABSTRACT

Water collection from natural and industrial fogs has recently been viewed as a viable freshwater source. An interesting outgrowth of the relevant research as focused on arresting of the drift losses (un-evaporated and re-condensed water droplets present in the exhaust plume from industrial cooling towers. Such exploits in fog collection have implemented metal and polyester meshes as fog water collectors (FWC). Fog droplets impinge and deposit on mesh fibers. They coalesce with previously deposited liquid to evolve as larger drops before detaching from the fibers under their own weight, an event largely dependent on the mesh fiber wettability, diameter and its arrangement relative to the fog flow. To better estimate drainage and hence collection from these fibers, the study, focuses on droplet detachment from differently wetted horizontally positioned cylindrical fibers of various diameters, placed orthogonally in the path of an oncoming fog. Droplet detachment volume is found to increase with fiber diameter and fiber surface wettability. Interestingly, in a typical fogging condition, the detachment volume is also found to exhibit a time-dependent behaviour, altering the droplet detachment criteria otherwise predicted from emulation. Our current study sheds light on this unexplored phenomenon.

Keywords: Fog harvesting; Cylindrical fiber; Surface wettability; Droplet detachment; Transient wetting

1. INTRODUCTION

Fresh water crisis is one of the most pertinent climate issues of this era, plaguing not only India but the entirety of the globe as seen in recent events. The situation is terrible in countries like India which accounts for only 4% of the world's freshwater resources despite having 16% of the world's population [1]. Nonconventional water sources need to be harnessed to bridge the gap between supply and demand. Fog harvesting is one such water conservation techniques that is looked up with much

hope. Fogging represents largely untapped source of water, especially in hilly areas and many industrial zones, the latter primarily referring to harvesting of cooling tower fog. Cooling tower (CT) happens to be one of the prominent sources of industrial fog. For a 500MW power plant, the amount of cooling water required is, 54000 to 60000 m³h⁻¹, from which nearly 3% is lost as vapour and fog from the CT exit.[2] To compensate for this loss, about 900 m³h⁻¹ of make-up water is needed. Tapping even mere 1% of this colossal volume means a saving of 9 tonnes of water in an hour.

In a typical fog harvesting configuration, fog droplets, typically in the size range of 4 – 40 μm, pass through meshes and get captured by the mesh elements. Such meshes or filters are used in large and small-scale atmospheric and industrial water harvesting systems [3, 4]. Geometrical structure of the fog collecting mesh and their surface wettability play major roles in the fog collection efficacy. Intuitively, it may appear that a denser net (i.e., having a large fraction of solid fiber per unit projected area of mesh) would imply that more fog particles would collide with the mesh fiber and gather more water. However, this is not typically the case. Smaller void fraction can also have a shielding effect [5], which would lower the mass flow of the fog stream through the mesh itself, and rather divert them around the mesh [6] [7, 8]. The fraction of the total oncoming fog stream to which the solid fibers pose as obstruction is denoted as aerodynamic efficiency η_{aero} . The percentage of the fog droplets, whose path ahead of the mesh is geometrically intercepted by the mesh fibers, which actually impinges on the fibers due to inertial impaction, interception and Brownian diffusion is accounted for by the deposition efficiency, or η_{dep} . It is interesting to note that not all the fog water that deposited on the mesh fiber can be collected. Part of it may be lost due to carryover by the oncoming fog stream, and a part will be lost due to premature dripping [9]. The percentage of water caught by the mesh that drains down the fibers and collects in the water collection manifold at the bottom of the

Designs of clog-free metal mesh for fog harvesting from cooling tower plume

Arkadeep Datta Arani Mukhopadhyay Amitava Datta Ranjan Ganguly

Advanced Materials Research and Applications (AMRA) Laboratory,
Department of Power Engineering, Jadavpur University (SL Campus), Kolkata – 700106

Corresponding author e-mail ID: arkadeepdatta@gmail.com

Abstract. With recent focus on sustainable development goals with an impetus on climate actions, there has been a sustained call from the industry to reduce their specific water consumption, especially in the power sector. One such avenue for catering to the sustainable consumption and production of power comes in the form of fog harvesting from the drift losses of cooling towers. The technology relies on placing a porous obstruction, e.g., a metal mesh, in the path of fog, at the exit of a cooling tower cell. The fog, either in the form of un-evaporated or re-condensed water droplets of 4 to 30 micron diameter are intercepted by these meshes. While such mode of fog harvesting surely shows promise of a substantial quantum of water recovery, the collection efficiency is usually poor due to several reasons, including poor aerodynamic efficiency. As the fog water is intercepted on the mesh, a typical mesh pore would get clogged, resulting in aerodynamic bypassing of the fog plume, low deposition and collection. The present study aims at improvising on the traditional stainless steel interweaved meshes by appropriately designing the critical parameters like mesh fiber diameter, pitch and porosity and defining their optimal values experimentally for a given mesh surface wettability. Based on these values and imposing the condition of 'no-clog' meshes, analytical estimates of aerodynamic and depositions efficiencies are made and an optimum design regime, as a function of mesh fiber diameter, is proposed. These modifications to the metal meshes involve solely structural design adjustments, without relying on any additional surface treatments. Consequently, they are deemed 'low-cost' and intended for convenient implementation in the industry

Keywords: Cooling tower fog harvesting; clog-free mesh; collection efficiency

1. Introduction

As the 21st century reels under the effects of global warming, there has been an orchestrated drive towards adoption of the COP 21 goals [1]. With dwindling water resources in industrial areas, especially power plants, there is a pressing urgency towards adopting new ways of reducing water consumption. Cooling tower exit plume

Bulletin of the American Physical Society

75th Annual Meeting of the Division of Fluid Dynamics

Volume 67, Number 19

Sunday–Tuesday, November 20–22, 2022; Indiana Convention Center, Indianapolis, Indiana.

Session T13: Industrial Applications: General

4:10 PM–6:33 PM, Monday, November 21, 2022

Room: 140

Chair: Kamran Alba, University of Houston

Abstract: T13.00011 : Microdroplet capture by a tunable dielectrophoretic (DEP) filter*

6:20 PM–6:33 PM

← Abstract

Presenter:

Harunori N Yoshikawa
(University of Nice Sophia-Antipolis)

Authors:

Harunori N Yoshikawa
(University of Nice Sophia-Antipolis)

Arkadeep Datta
(Department of Power Engineering, Jadavpur University, Kolkata 700106, India)

Ranjan Ganguly
(Department of Power Engineering, Jadavpur University, Kolkata 700106, India)

Dielectrophoretic (DEP) collection of water droplets, 5 to a few tens of microns in diameter, transported in an air free-stream is investigated through a numerical simulation in view of applications in air purification technology. The droplet transport-dynamics are modelled as passive individual particles using a Lagrangian scheme that takes into account the interplay of inertia, viscous, DEP and random Brownian forces on the dispersed phase. The DEP filter is assumed to consist of an array of cylindrical model fibers, which also serve as electrodes where three-phase voltage is imposed. The filtering efficiency is determined through statistical analysis of the simulation results. The effects of the applied electric voltage on the filter efficiency are examined for different droplet diameters and inter-fiber distances and for a wide range of air velocity. The optimum frequencies at which the droplet capture efficiency attains its maximum value are also determined. It is shown that these frequencies are well correlated by a single dimensionless number representing the residence time of particles in the vicinity of the filter. Findings of the study leads to the design bases of active filtration systems for critical healthcare enclosures and advanced face masks.

*The present work is supported by the international emerging action (IEA) program of the French National Centre for Scientific Research (CNRS) under the grant IEA00338. AD and RG also acknowledge the funding from DST SERB (Grant No: CRG/2019/005887).

Droplet Morphology-Based Wettability Tuning and Design of Fog Harvesting Mesh to Minimize Mesh-Clogging

Arani Mukhopadhyay,[‡] Arkadeep Datta,[‡] Partha Sarathi Dutta, Amitava Datta, and Ranjan Ganguly*



Cite This: *Langmuir* 2024, 40, 8094–8107



Read Online

ACCESS |



Metrics & More

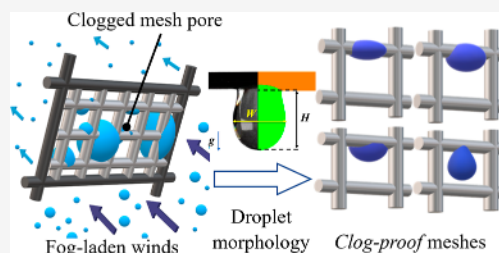


Article Recommendations



Supporting Information

ABSTRACT: Fog harvesting relies on intercepting atmospheric or industrial fog by placing a porous obstacle, for example, a mesh and collecting the deposited water. In the face of global water scarcity, such fog harvesting has emerged as a viable alternative source of potable water. Typical fog harvesting meshes suffer from poor collection efficiency due to aerodynamic bypassing of the oncoming fog stream and poor collection of the deposited water from the mesh. One pestering challenge in this context is the frequent clogging up of mesh pores by the deposited fog water, which not only yields low drainage efficiency but also generates high aerodynamic resistance to the oncoming fog stream, thereby negatively impacting the fog collection efficiency. Minimizing the clogging is possible by rendering the mesh fibers superhydrophobic, but that entails other detrimental effects like premature dripping and flow-induced re-entrainment of water droplets into the fog stream from the mesh fiber. Herein, we improvise on traditional interweaved metal mesh designs by defining critical parameters, viz., mesh pitch, shade coefficient, and fiber wettability, and deducing their optimal values from numerically and experimentally observed morphology of collected fog water droplets under various operating scenarios. We extend our investigations over a varying range of mesh-wettability, including superhydrophilic and hydrophobic fibers, and go on to find optimal shade coefficients which would theoretically render *clog-proof* fog harvesting meshes. The aerodynamic, deposition, and overall collection efficiencies are characterized. Hydrophobic meshes with square pores, having fiber diameters smaller than the capillary length scale of water, and an optimal shade coefficient are found to be the most effective design of such *clog-proof* meshes.



1. INTRODUCTION

The accentuating crisis of freshwater in the last few decades has led to a serious drive for the development of technology focused on sustainable water harvesting.¹ Harvesting fog from diverse sources such as natural environments² or industrial cooling towers³ using a mesh has emerged as an affordable and viable alternative. Polypropylene fiber-based Rachel meshes, featuring trapezoidal pores have been extensively used for atmospheric fog harvesting in different parts of the world.^{4,5} However, for heavy fogging under high stream velocities, as is typical in industrial scenarios, sturdy metal meshes having square pores are better suited for long-term use.⁶ A fog-laden stream passing through a mesh deposits the fog droplets (ranging from 4 to 30 μm in diameter^{7,8}) on the fibers by inertial impaction, physical interception, and Brownian diffusion.⁹ Progressive deposition of these fog-droplets and subsequent coalescence of the deposited liquid lead to the formation of bigger droplets [O (~ 1 mm)] of different shapes on the fibers. These growing droplets may eventually touch the neighboring mesh fibers, when they clog the mesh pore either partly or completely (see Figure 1A). A clogged mesh pore offers a greater aerodynamic resistance to the oncoming fog stream, which in turn diminishes the fog droplet deposition. The droplet shape on a fiber depends on its volume, the wettability of the mesh fiber and the fiber diameter.^{10,11}

Therefore, the morphology of the droplet and its relative size with respect to the mesh dimensions, and the fiber wettability play important roles¹² in ascertaining the fog-harvesting performance of a mesh.

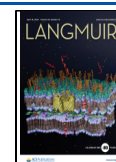
Wettability engineering has been extensively leveraged by several researchers to enhance fog harvesting on sturdy impervious flat surfaces by advocating the use of 3D features like cascading patterns,¹³ bumps¹⁴ or bioinspired surface modifications,^{15–18} and micro/nanoscale surface embellishments¹⁹ for enhancing water capture. However, these impervious plates suffer from significant aerodynamic bypassing—the fog stream gets diverted by the plate in the fog-flow path²⁰—leading to minimal fog deposition. Biomimetic surfaces, replicating the Namib desert beetle *oniscus asper*,^{21,22} cactus thorn-like geometries,²³ or variations in surface wettability,^{24,25} have shown attractive droplet drainage features for laboratory-scale setups, but they lack

Received: January 7, 2024

Revised: March 15, 2024

Accepted: March 22, 2024

Published: April 3, 2024



Arkadeep Datta
27/03/2024